Detection of fiber fracture in Unidirectional Fiber Reinforced Composites using an In-Plane Fiber Optic Sensor

by

Christopher D. Cassino

Thesis submitted to the faculty of
Virginia Polytechnic Institute and State University
in partial fulfillment of the requirements for the degree of
Master of Science in Engineering Mechanics

Approval Names:
J. C. Duke Jr.
E.G. Henneke II
M.R. Hajj

April 26, 2002
Blacksburg, Virginia

Keywords: EFPI, Acoustic Emissions, CFRP, Structural Health Monitoring

Detection of fiber fracture
in Unidirectional Fiber Reinforced Composites
using an In-Plane Fiber Optic Sensor
by
Christopher D. Cassino
J.C. Duke, Jr., Advisor
Engineering Mechanics

ABSTRACT

Fiber reinforced polymers (FRP) are an efficient and inexpensive method of repairing deteriorating infrastructure. FRP sheets can be applied to spalling bridge sections and columns to prevent further deterioration and increase stiffness. However, the effect of the environment on the long-term durability of FRP and how the various damage mechanisms initiate and develop are not known. Systems for structural health monitoring are being sought as a means of managing important components in transportation systems as assets in light of modern life cycle cost concepts. This study characterizes a fiber optic sensor for use in detecting acoustic emissions (AE) in FRP. The results of AE analysis (signal amplitude, frequency spectra, MARSE, and in-plane displacement) caused by simulated fiber fracture experiments and other types of mechanical loading in FRP test coupons are reported. The applications to the development of FRP structural health monitoring systems are also discussed.

Author's Dedication

This is dedicated to my little brother, Daniel. He was always the better writer, the more academic one and the great conversationalist. He was also a source of inspiration and support, even through his own great ordeals in college. Thank you brother.

Acknowledgments

There are so many people that helped me with this. I would say responsible for as well, but I wouldn't want them to share any blame, only credit. For instance, I would not have finished my thesis or even attempted graduate school without the love and constant support from my wife, Theresa. Furthermore, I am very grateful for the deep insight, support and careful guidance that Dr. John C. Duke provided throughout my Master's study. It was an honor walking in the footsteps of him, Dr. Henneke and other NDE gurus at VT. Finally, without the financial and technical support of Luna Innovations, I wouldn't have had any food or sensors throughout the two years this work took to finish. I would also like to thank the following people for their help and advice:

1. Michael R. Horne, for his sage-like grasp of NDE, AE and lab management. Without his technical assistance I would have left my lab in a smoking ruin. Without his camaraderie I would have had no head to bounce crazy ideas off.
2. Brooks Childers, Clark Boyd, Jason Borinski, Jason Dietz and all Luna employees that I have associated with in the past two years.
3. Dr. W. H. Prosser for his assistance in modeling and his incisive and accurate questioning of our results which lead to a deeper understanding of my work.
4. Dr. M. R. Hajj for his explanations of the complex models and methods used to understand turbulence, which directly influenced the way I approached this work.
5. Dr. Scott Hendricks who taught a civil engineer that things are not always broken if they move.
6. Mac McCord and the MRG graduate students who let me borrow microscopes, heat guns and sugar when we were out of it in Hancock 200.
7. My parents who never stop teasing me about staying in school until I receive social security benefits. Seriously though, thank you Dad, Helen, Mom and Greg.
8. Jesus Christ and St. Mary's Catholic Church for keeping my marriage strong, my life sane and my perspective realistic when things weren't going my way.

Table of Contents

List of Figures

List of Tables

Chapter 1 - Introduction

Almost one-third of the 581,862 bridges over 6 meters in length in the United States of America are structurally or functionally deficient according to the standards set by the American Society of Civil Engineers [1]. A functionally deteriorated bridge cannot support its designed service levels of traffic load and speed. A structurally deficient bridge is an imminent hazard and must be repaired. Current trends in infrastructure management have led engineers to analyze the benefits and costs related to repairing structures within a transportation network rather than building new structures[2]. Unfortunately, there is considerable disagreement as to what type of damage a structure can sustain before it needs repair. The evaluation of structural and material damage is subjective and can vary widely based on personal experience and judgment [3-6].

Visual inspection is the primary accepted method of bridge inspection nationwide. Non-destructive methods have been developed in order to remedy the problem of examining and evaluating bridges subjectively. These methods help engineers decide the "health" of a structure and make accurate assessments about when and where a bridge is most in need of repair. The goal of any health monitoring study is to provide useful data that can aid engineers and maintenance crews in repairing and maintaining structures. Global scale structural information can be related to data from local regions using non-destructive evaluation (NDE) of the structure [7, 8]. Using sensors, regions of damaged material or structural concern can be determined in a faster and more accurate manner than by human observation alone.

The advance of materials technology has led to the development of novel materials that can be used to repair bridge structures efficiently. While many materials are now available, high strength composites represent an ideal way to repair bridge structures [9]. Applying unidirectional fiber reinforced plastics (FRP) to the underside of bridge decks to stiffen aging structures and increase allowable traffic loads has been shown to be an effective method of rehabilitation [10]. Layers of FRP can also be wrapped around deteriorated columns and beams to strengthen the overall structure and provide exterior confinement [11], Figure 1.01.

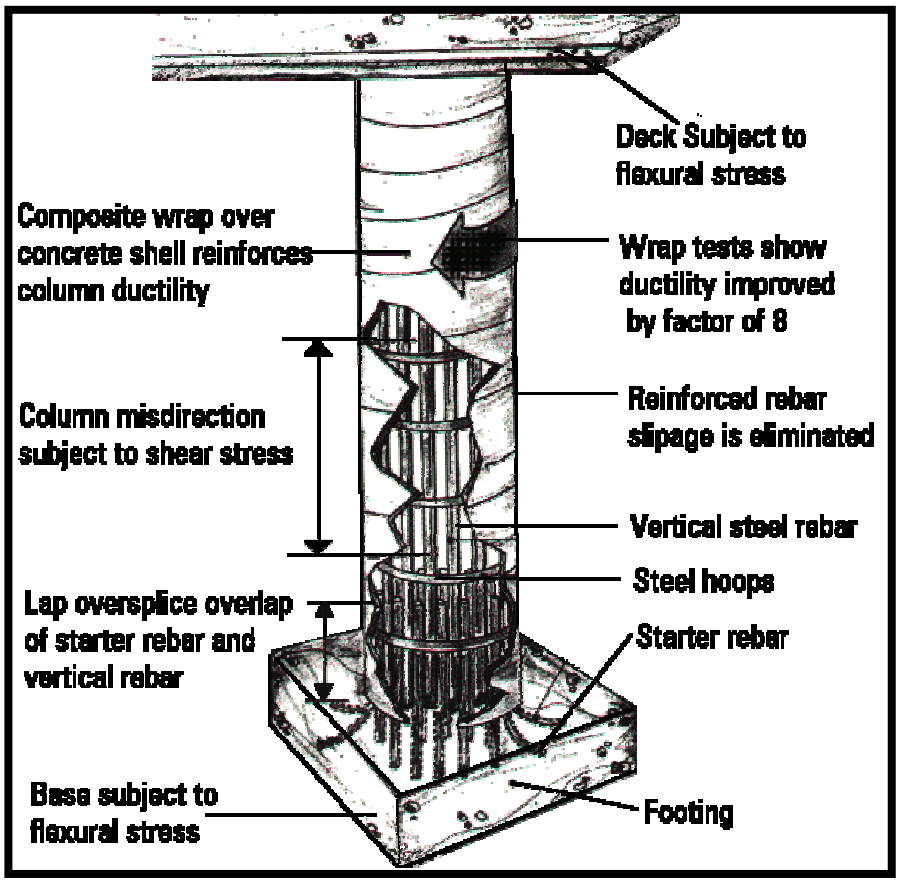

Figure 1.01: Typical FRP Infrastructure Application, adapted from www.fibrwrap.com

However, little is known about the long-term durability of composites exposed to the environment during their service life [12]. In FRP, this is especially necessary because the integrity of the material is dependent on many factors that are not immediately apparent or even detectable by the human eye. For instance, an area of resin poor fibers would transfer stress to the surrounding material much differently than a properly saturated fiber/matrix composite. While a resin poor area would be detectable if it were on the surface of a structure, FRP reinforcement is often many layers, or plys, deep and the surface is often painted for aesthetic purposes. Therefore, the standard method of large-scale structural inspection, human observation, is not adequate when inspecting FRP.

The question of what would be a better alternative to human observation is not easy to answer. Although there are many different methods of non-destructive inspection, no single method offers a panacea [13]. By using multiple methods accurate and sensitive measurements can be obtained from a structure to aid engineers in selecting an effective

method of repair. In order for an inspection method to be useful in monitoring and evaluating FRP, it must be robust and versatile given the variability of the location, material and purpose of FRP in infrastructure. A useful NDE method would be able to evaluate the current condition of the materials in a structure with access to only the outer surface in quick and easy to interpret fashion. A potential method of achieving all of these goals and successfully evaluating the long-term structural health of FRP in infrastructure applications is monitoring the acoustic emissions (AE) from the composite [11]. Figure 1.02 is a symbolic diagram of the AE monitoring method.

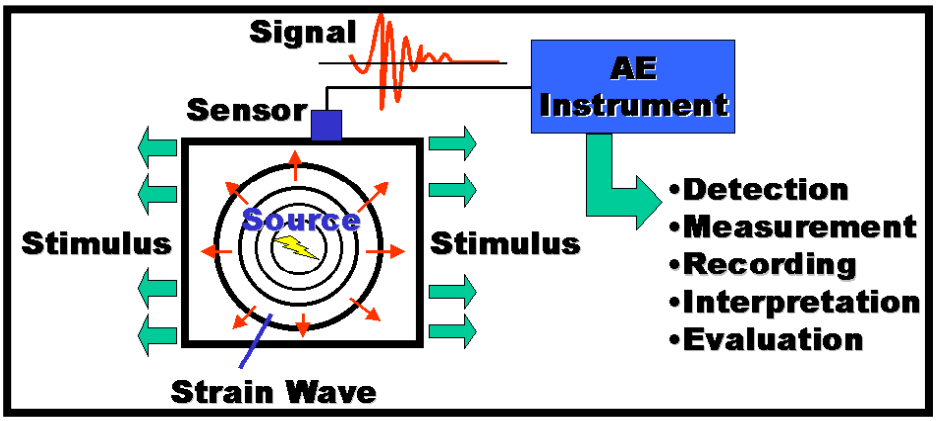

Figure 1.02: Acoustic Emissions Monitoring Process

The method, study and detection of AE in materials has been well developed (see references [14-25]). In composite materials, AE has been used to monitor the progression of damage and the critical failures in structures (see references [12, 20, 24, 26-31]). However, there are several problems concerning the use of AE monitoring in FRP. For instance, pre-failure damage might occur in the direction parallel to the reinforcing fibers instead of perpendicular to the surface of the fibers. Current AE transducers are not optimally sensitive to this kind of in-plane displacement unless the damage mechanism also produces a component of out-of-plane displacement. It has been demonstrated that optical interferometric systems can be used to monitor in-plane displacements and AE in materials [32].

The health monitoring concerns in FRP can be addressed by using a novel sensor developed by Luna Innovations: the extrinsic Fabry-Perot interferometer (EFPI). It is the goal of this study to verify that the EFPI can detect AE from fiber fracture. A secondary goal is to compare the use of in-plane sensors to out-of-plane sensors in structural health

monitoring of fiber reinforced composites so that the EFPI can be compared and understood in the context of previous AE research. The major contribution of this work is the description of a method that relates the mechanical nature of a fiber fracture to the results from AE detected using sensors to monitor on fiber reinforced composites.

The second chapter of the thesis discusses the pertinent literature and current research in acoustic emission monitoring, infrastructure rehabilitation, the mechanics of FRP composites and using NDE to monitor the structural health of FRP. The basic concepts of wave propagation in anisotropic materials are also discussed in the chapter. The methods used in analysis of AE signals and modeling FRP materials as well as the mathematical conventions in this work are also defined.

In chapters 3 through 14, the experimental methods, results and discussion of the results for four related test series are covered in detail. The four test series are: EFPI system calibration and characterization, optical fiber breaks on an aluminum plate, optical fiber breaks in MBrace^{tm} CFRP and mechanical loading of MBrace^{tm} coupons. Each test was designed with three goals in mind. First, to define the system and calibrate the sensor response with respect to a well characterized source. Second, to create ideal scenarios where the only form of damage occurring in a FRP sample is fiber fracture and record and analyze AE from those conditions. Third, to compare other, more realistic failures to the previous results and use the knowledge of the system response and the character of an ideal fiber fracture to identify fiber fracture in FRP coupons. For purposes of clarity and continuity, each experiment is divided into three separate chapters dealing with the experimental materials and methods, results and a discussion of the results. Chapter 15 discusses the significance of the results in light of the research goals and what possible conclusions can be drawn from the experiments. This chapter also discusses ideas for future work and related ideas for using the EFPI in structural health monitoring. The importance of this work lies in the characterization of a novel sensor for use in NDE and a method of using it to detect fiber fracture in FRP composites. Appendices are also included to aid others that may pursue NDE research using the EFPI and FRP composites.

Chapter 2 - Literature Review

Definition of Coordinate System and Conventions

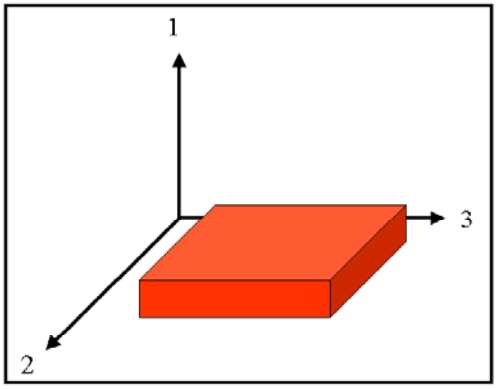

Figure 2.01: Definition of Coordinate System

A consistent sign convention and coordinate system is used throughout this work, Figure 2.01. The coordinates shall be written in terms of the position on the 1, 2, 3 axes. Alternatively, the coordinates can be denoted using X1, X2, X3 or X, Y, Z for the coordinate axes. When considering plates or samples, the origin is located in the middle of the horizontal plane. The reduced tensor notation (11—1, 22—2, 33—3 23—4, 13—5, 12—6), is used to describe the general 3-D linear elastic stress-strain relations. References [20, 33] give a full description of the mathematical conventions used in this work.

Overview of Acoustic Emissions

Acoustic emission, according to the American Society for Testing and Materials (ASTM) [34], refers to the generation of transient elastic waves during the spontaneous release of energy from localized sources within a material. Most materials used in construction and engineering produce acoustic emissions when deformed. Acoustic emissions can be monitored and recorded using many different techniques, although most of the techniques focus on using highly sensitive listening devices to detect the vibration or pressure changes caused by the wave. ASTM references [34-39] give a detailed description of AE terminology and standard practice. Table 2.1 lists the ASTM standards relevant to this work.

Table 2.1: Relevant ASTM Standards for AE and FRP Testing

Test Specification	ASTM Standard
Mounting Piezoelectric AE Sensors	E 650-97
Characterizing AE Instrumentation	E 750-88
Determining Reproducibility of AE Sensor Response	E 976-94
Primary Calibration of AE Sensors	E 1106-86
Secondary Calibration of AE Sensors	E 1781-96
Tensile Properties of Polymer Matrix Composites	D 3039M-95a
Mode I Interlaminar Fracture Toughness of Unidirectional Fiber Reinforced Polymer Matrix Composites	D 5528-94a
Classifying Failure Modes in FRP Joints	D 5573-94
Lap Shear Adhesion for FRP Bonding	D 5868-95
Acousto-Ultrasonic Assessment of Composites, Laminates and Bonded Joints	E 1495-97
Terminology of Nondestructive Examinations	E 1316-97b

Many of the current sensors used for the detection of acoustic emissions use piezoelectric crystals that transform the surface displacement due to the mechanical energy of the wave into an electric signal. Monitoring acoustic emissions from a structure can reveal the presence of on going damage or deformation processes, especially in large structures such as bridges or dams.

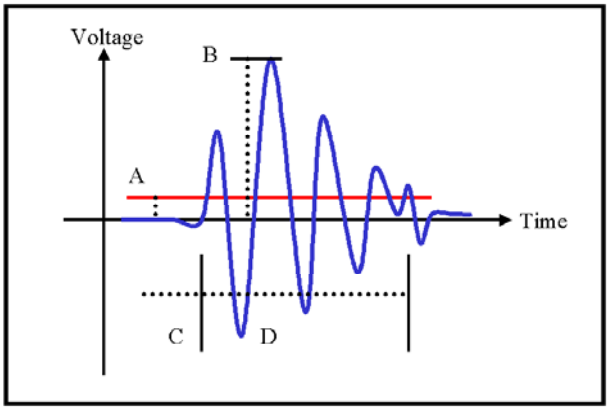

Figure 2.02: Typical AE Signal

Figure 2.02 is a representation of a typical AE signal as viewed on an oscilloscope or data acquisition system capable of receiving input from a transducer [16]. The ordinate is typically time, usually measured in microseconds. The abscissa is the voltage output of the transducer response to the displacement of the material surface. The line at point A is the threshold value or the minimum value of displacement or voltage that causes the monitoring system to “trigger” and begin recording data.

Some systems use a pre-trigger, which makes it possible to capture data for a pre-determined period of time before the sensor output initially surpasses the threshold value. The distance from the ordinate to the line at point B is the maximum positive amplitude of the event. Generally, the monitoring equipment or software is set-up to trigger off of a positive displacement value but software exists that can monitor the degree that the slope of the signal changes, and in which direction it changes, for triggering purposes.

Each time that the amplitude of the signal is equal to or greater than the threshold value is called a "hit." The period of time from the start of the signal to the line at point C is called the rise time and the period of time from point C to point D that the signal amplitude remains above the threshold is called the decay time. Another signal related measurement is the energy envelope, which is often used to correlate different types of damage. This quantity is the measured area under the rectified, or positive, signal envelope, also known as MARSE [16], Figure 2.03.

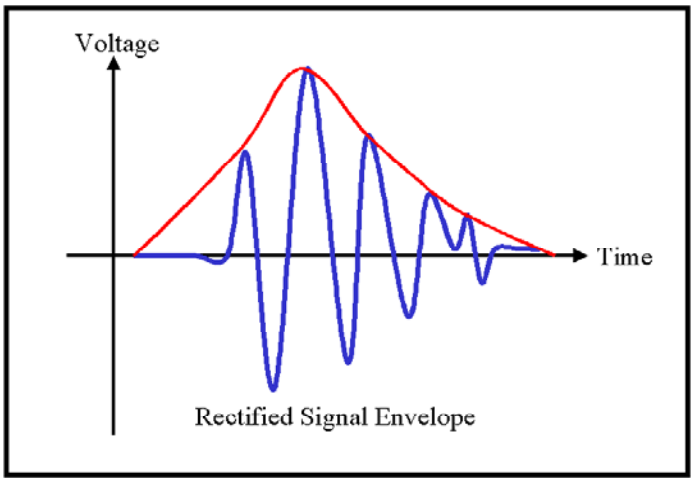

Figure 2.03: Typical rectified signal envelope.

MARSE is an easy quantity to calculate using numerical methods. The area under the signal peaks can be calculated by taking a trapezoidal area defined by positive voltage values and the time step under any peak and adding the area from each trapezoid. Equation 2.01 expresses this idea mathematically where n is the total number of points in the signal, V_n is the voltage at point n and V_{n+1} is the voltage at point $n+1$ and t_n is the time in the signal record that V_n occurs and t_{n+1} is the point of time when V_{n+1} occurs. For this study, n was typically 8800 points and $t_{n+1} - t_n$ was 0.04, in microseconds.

$$MARSE = \sum_{0}^{n} \frac{V_n + V_{n+1}}{2}[t_{n+1} - t_n] \qquad (2.00)$$

When choosing transducers to monitor AE it is important to consider the frequency range of the signals of interest and to choose a sensor with an ideal response in that range. If the sensor response is not considered the sensor may contaminate the signal with irrelevant data or not function efficiently in the selected application [33]. For instance, if it is important to detect a certain direction of displacement, then a sensor should be selected that is optimally sensitive to that form of displacement. Most sensors currently manufactured are multi-modal, that is, sensitive to different wave modes and directions of displacement. The information from multi-modal transducers cannot be used to determine the direction of the displacement. For example, a disturbance of a point on the surface of a plate has three components of displacement, in the 1, 2 and 3 directions, but only the combination of the displacements is capable of being recorded by the sensor (see equation 2.01).

$$D(t) = \sqrt{u(t)^2 + v(t)^2 + w(t)^2} \qquad (2.01)$$

The equation available to determine the individual components of displacement has one known quantity at a particular point in time, D(t), and three unknowns, the components of displacement in the 1, 2, 3 directions over time. The directional uncertainty occurs because some or all of the points on the surface of the transducer are in contact with the surface of the material deforming. However, all of the displaced points on the surface of the transducer may not displace at the same time or in the same direction, Figure 2.04.

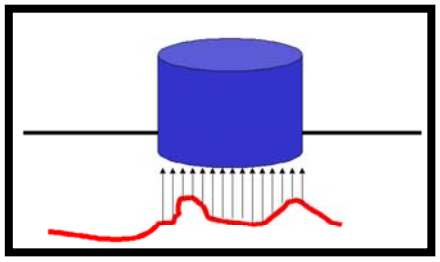

Figure 2.04: Sketch of Sensor Displacement varying with Time and Position along a line

The voltage output of a piezoelectric transducer is achieved by summing the displacement of all the points on its surface. As the source of a displacement changes (either by decaying or increasing) the resulting stress waves that impinge on the surface

of the sensor will displace separate points differently. The larger the surface area of the transducer the more pronounced might be the difference in displacement between different points in time. A well-calibrated sensor that is often used as a standard, the National Institute of Standards and Technology (NIST) conical transducer has a smaller surface area in order to increase the probability that all of the points on the surface of the transducer will be displaced at the same time. It should be noted that the NIST transducer is not suited for work on composites because the sensor requires a conductive path between the tip of the transducer and the main signal amplifier. Other sensors are currently available which have a minimal surface area. These sensors are called "point" or "pin" transducers.

The monitoring of acoustic emissions is considered a "passive" inspection method because processes occurring in the structure itself, rather than someone or something affecting the structure, generate the emissions. While active acoustic methods exist, such as acousto-ultrasound, ultrasonic testing and impact echo, they cannot reveal the type of information available in AE signals and are better suited to the inspection of suspected structural defects rather than long term monitoring [40]. AE sensors require access only to the exterior surface of the structure and the emissions that can be detected are dependent on the material and the geometry of the structure. Because of the inherent dependence of the emissions on the intrinsic material properties of the structure it may be possible to characterize the type of event causing an emission with a specific character to a type of event [16]. Although it is generally easier to estimate the location of the event relative to the sensor than to characterize the event that caused the deformation.

Wave Propagation in an Anisotropic Medium

It is helpful to understand the physics and physical concepts behind acoustic emission monitoring when studying a material. The physical reasons behind the AE and the mathematics behind the physics of waves in solids materials are inseparable in most detailed AE studies. Mathematically, the various ways that disturbances can propagate through anisotropic materials govern the detection of AE in FRP. Physically, the vibration of broken fibers and various other mechanisms that deform FRP initiate the disturbance which then propagates at rates that can be investigated mathematically. As

such, a brief review of the mechanical behavior of anisotropic materials and how it can affect wave propagation is useful. Equally useful, is the development of a conceptual model to represent fiber fracture in FRP. Most of the following material has been synthesized from Dr. Edmund G. Henneke's [41] and Dr. Ronald D. Kriz's course on wave propagation in elastic solids and the on-line course lecture notes [42], as well as ideas discussed in Dr. Scott Hendrick's class on structural vibrations.

Mathematical Model of Wave Propagation

In order to understand the effect of a disturbance traveling through an anisotropic continuum, the dynamic mechanical behavior of the anisotropic solid must be considered in the equations of motion for a continuum. Imagine a spherical disturbance such as a dilatational pulse expanding equally in all directions. By invoking Huygen's principal it is possible to envision a very small plane wave, which can exist on the surface of a very small sphere in the center of an anisotropic solid, such as a crystal. From Huygen's principal each of these planes travels in a unique and specific direction with direction cosines, ν_i, at a speed that corresponds to elastic properties in the corresponding direction.

Therefore, plane waves traveling in different directions will travel at different speeds if the elastic properties are different. The continuous collection of all plane waves, although initially a sphere, soon distorts into a non-spherical shape simply because plane waves propagate faster in stiffer directions. The wave surface topology created by this distortion uniquely describes a complete set of components of the fourth order stiffness tensor. In order to prove this, begin with the equations of motion for a continuum and Hooke's Law for linear elastic solids.

$$\sigma_{ji,j} = \rho \frac{\partial^2 u_i}{\partial t^2} \tag{2.02}$$

$$\sigma_{ij} = C_{ijkl}\, l_{kl} \tag{2.03}$$

and substitute the strain-displacement relationship,

$$l_{ij} = \frac{1}{2}\left(u_{i,j} + u_{j,i}\right) \tag{2.04}$$

into equation (2.03) to yield

$$\sigma_{ij} = \frac{1}{2} C_{ijkl} \left(\frac{\partial u_k}{\partial x_l} + \frac{\partial u_l}{\partial x_k} \right) \tag{2.05}$$

Recall that the strain tensor is symmetric which further reduces the equation,

$$\sigma_{ij} = C_{ijkl}\, u_{k,l} \tag{2.06}$$

Substituting equation (2.02) into equation (2.06) yields the equation of motion in terms of displacements.

$$\frac{\partial \left(C_{ijkl}\, u_{k,l} \right)}{\partial x_j} = \rho \frac{\partial^2 u_i}{\partial t^2} \tag{2.07}$$

This equation can be further reduced if it is possible to assume that the material is homogeneous.

$$\frac{\partial C_{ijkl}}{\partial x_j} = 0 \tag{2.08}$$

With this simplification equation (2.09) reduces to a form where we can now assume a solution for the displacement and substitute it into this equation.

$$\frac{C_{ijkl}}{\rho} \frac{\partial^2 u_k}{\partial x_l \partial x_j} = \frac{\partial^2 u_i}{\partial t^2} \tag{2.09}$$

Now, imagine what a small periodic displacement in a continuum in the form of a plane wave would look like. Figure 2.6 is a sketch of a small plane wave oscillating periodically.

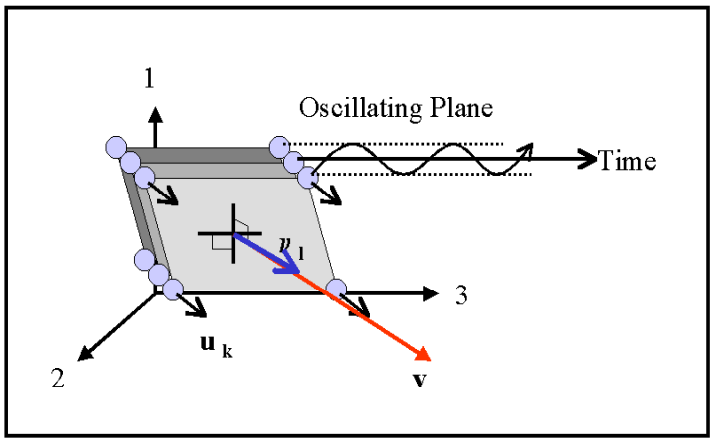

Figure 2.05: Graphical model for a plane wave disturbance.

The periodic plane displacement in Figure 2.05 is best represented using an exponential functional form instead of sines and cosines because it is easier to differentiate. Equation 2.10 defines the particle displacement, $\mathbf{u_k}$, in terms of wave velocity, $\mathbf{v}$, the direction cosines of the propagation direction, ν_i. In equation 2.10, A_k is the amplitude of the particle vibration, which can be decomposed into $\mathbf{A}\alpha_\mathbf{k}$, where $\mathbf{A}$ is the scalar magnitude of the vibration and $\alpha_\mathbf{k}$ is the particle vibration direction.

$$u_k = A_k e^{i\left(k_l x_l - \omega t\right)} \tag{2.10}$$

The terms in the exponent are derived from the plane wave equation, assuming that the oscillation is periodic with a circular frequency, ω. Replacing $\mathbf{A_k}$, $\mathbf{k_l}$ and ω with the decomposed notation mentioned above allows a more relevant interpretation of the substitution and the eigen-system.

$$u_k = A\,\alpha_k e^{ik\left(\nu_l x_l - v t\right)} \tag{2.11}$$

Substituting equation (2.11) into equation (2.09), equation (2.09) reduces to an eigen-value problem which is written below in both tensor (2.12a) and matrix notation (2.12b).

$$\left(C_{ijk\ell}\,\nu_j\nu_\ell - \rho v^2\,\delta_{ik}\right)\alpha_k = 0 \tag{2.12a}$$

$$\begin{bmatrix} \left(c_{11}\nu_1^2 + c_{66}\nu_2^2 + c_{55}\nu_3^2\right) - \rho v^2 & \left(c_{12} + c_{66}\right)\nu_1\nu_2 & \left(c_{13} + c_{55}\right)\nu_2\nu_3 \\ \left(c_{12} + c_{66}\right)\nu_1\nu_2 & \left(c_{66}\nu_1^2 + c_{22}\nu_2^2 + c_{44}\nu_3^2\right) - \rho v^2 & \left(c_{23} + c_{44}\right)\nu_2\nu_3 \\ \left(c_{13} + c_{55}\right)\nu_2\nu_3 & \left(c_{23} + c_{44}\right)\nu_2\nu_3 & \left(c_{55}\nu_1^2 + c_{44}\nu_2^2 + c_{33}\nu_3^2\right) - \rho v^2 \end{bmatrix} \begin{Bmatrix} \alpha_1 \\ \alpha_2 \\ \alpha_3 \end{Bmatrix} = 0 \tag{2.12b}$$

If the matrix form of equation (2.12b) is used it is easier to see that the velocity terms along the diagonal, $\rho\mathbf{v^2}$, are the eigen-values and the displacement direction cosines, α_i are the eigen-vectors. Closer examination of the solution to this particular eigen-value problem reveals that both the eigen-values and eigen-vectors can only be functions of all stiffness tensor components for an assigned propagation direction, ν_i.

Hence it is possible to conclude that by solving for eigen-values (wave speeds) in all possible propagation directions, ν_i and connecting points to form a continuous surface, a 3-D shape would be generated representing each wave speed. Since there are three eigen-values, equation (2.12) predicts three wave sheets: a quasi-longitudinal one, which is usually the fastest and observed as the largest shapes; two different shear, or quasi-transverse, waves which are usually slower and consequently observed as smaller shapes. Using computers to visualize the wave surfaces, the direction cosines (0 to 90 degrees) can be mapped onto the eigen-value surfaces as different colors. Although the problem becomes more complex when the condition of homogeneity cannot be assumed, the basic solution and the results of the solution are similar. Literature sources [43, 44] give more detail on wave propagation in elastic, inhomogeneous solids.

Conceptual Model of Mechanisms that Generate AE in FRP

The study of wave propagation in plates, rods and isolated fibers has been well developed [14, 17-19, 24, 25, 30, 45, 46]. In FRP systems, which consist of fibers surrounded by a matrix and cured into a plate-like structure, there are many possible sources of acoustic emissions. References [20, 26, 28, 30, 40, 47] report research relating specific AE sources to sensor response in composite materials. For example, matrix cracking due to the strain caused by load transfer or stress concentrations caused by voids in the composite can result in AE in a fiber reinforced material. Delamination of the FRP layers or from the surface of another material can also be the cause of AE. An important source of AE in FRP materials is due to the fracture of the load bearing fibers. In order to understand how fiber fracture could cause AE in FRP consider a uniform elastic rod loaded in the elastic range, with a constant mass per unit length, ρ, a constant cross-sectional area A, and a constant value for the tensile modulus E [48]. Imagine also that the ultimate strength of the rod is at the end of the elastic range before it begins to experience permanent, in-elastic deformation. The reaction of the rod to mechanical loading is similar to the behavior of a reinforcing fiber, Figure 2.06.

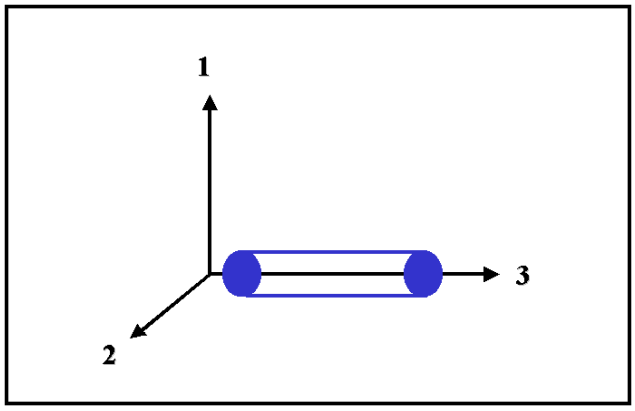

Figure 2.06: Elastic Rod/Fiber Model

If the rod were free on either end it would have the ability to translate or displace anywhere along its length in any direction. However, if the rod were fixed on either end, it could only vibrate in an axial, flexural, torsional or combined mode. Now imagine what would happen if the rod were then stretched until it just passed its ultimate strength and fractured along an even plane. See figure 2.07. If the fracture were a completely even cut along a plane parallel to the 1-2 plane then the two rods created by the fracture would convert the potential elastic strain energy to kinetic energy by vibrating axially, Figure 2.08.

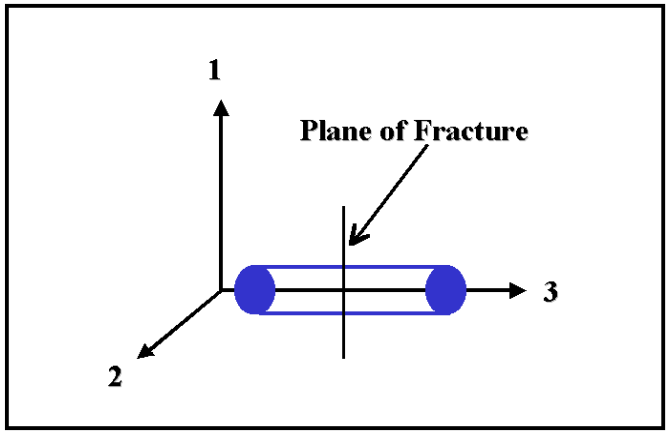

Figure 2.07: Ideal Plane of Fracture

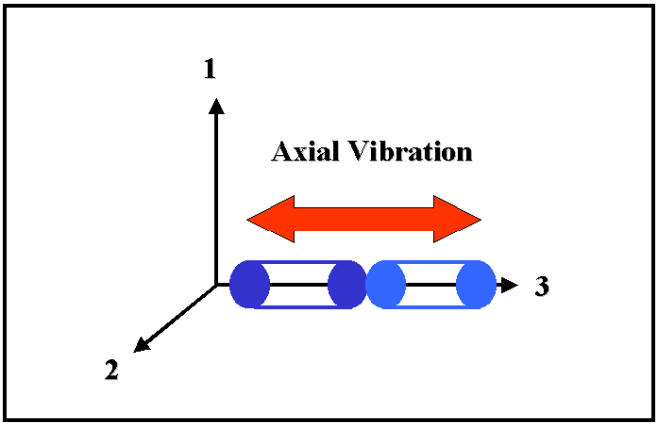

Figure 2.08: Fractured Rod in Axial Vibration

If the plane of fracture was not parallel to the 1-2 plane, say it was skewed some angle α in the 2-3 plane, and then the two rods would vibrate in mixed modes, or flexurally, like cantilever beams. See Figures 2.09 and 2.10.

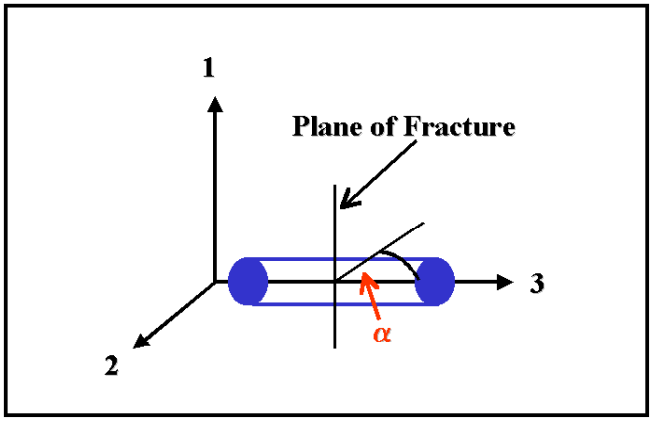

Figure 2.09: Fracture Skewed in the 2-3 Plane

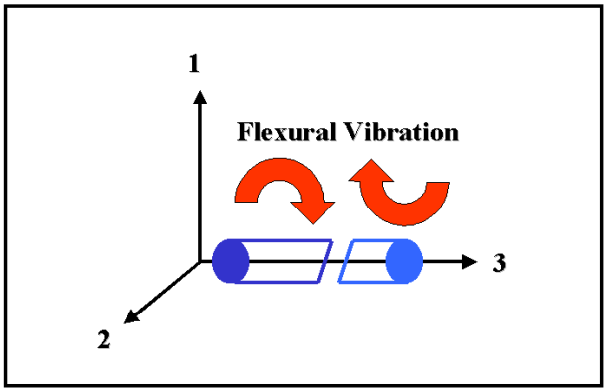

Figure 2.10: Fractured Rod in Flexural Vibration

If the plane of fracture was skewed some angle α in the 2-3 plane and some angle β in the 1-3 plane then the two rods would vibrate in a combined flexural and torsional mode (figures 2.11 and 2.12).

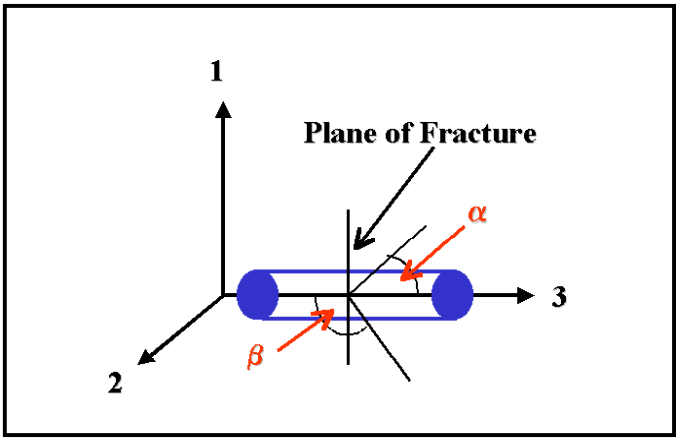

Figure 2.11: Fractured Skewed in the 1-3 and 2-3 Planes

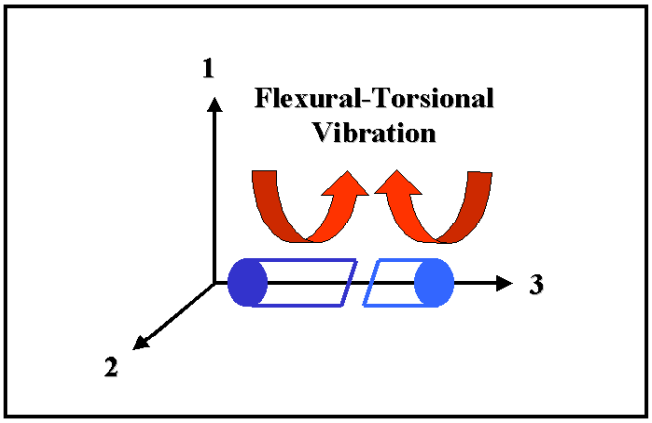

Figure 2.12: Fractured Rods in Flexural-Torsional Vibration

Now imagine that the rod is surrounded by an infinite elastic medium while still fixed on either end. When the rod fractures it is free to vibrate axially or torsionally but due to its contact with the medium it is restricted in how much it can vibrate flexurally. However, if the plane of fracture imparts a torsional or combined vibration mode to the two rods the energy stored in the rods will be released to the surrounding medium as the rods attempt to vibrate. Eventually, interaction between the rods and medium would dampen the amplitude of the vibrations. As the volume of the medium that was affected by the vibrations grows larger, the amount of mass involved will eventually dampen the energy of the vibrations.

In FRP, the load released from fiber fracture is redistributed to surrounding fibers through shear loading of the matrix. Each fiber fracture may cause further ruptures until either equilibrium is reached between the current load and the remaining fibers or total failure of the structure occurs [29]. Each fiber fracture imparts energy to the local matrix and fibers in the form of strain and the elastic stiffness of the constituent materials affect the transfer of the strain energy to its global surroundings. Using this idea it is possible to envision an "ideal" fiber break. Imagine a fiber of comparable density, elastic modulus and diameter. If this fiber was placed in a FRP coupon and loaded so that it was the only fiber to fracture, then the resulting displacement and therefore AE should be comparable to a random fiber break in the coupon. However, if the fiber were placed carefully, then the location of the fiber break would be known. By varying the location of the fiber, the effect that changing the location of the fiber break source has on the ability of a sensor to detect fiber break AE could be studied.

AE Signal Loss and Attenuation

In order for acoustic energy to be transmitted as efficiently as possible from one material to another the stiffness and density of each material should be close to the same values. If the FRP material has very stiff or very compliant materials on its boundaries then the amount of strain energy that can be transmitted to the surroundings from a single fracture event is decreased. In FRP materials, scattering and attenuation make it difficult for AE to be detected over long distances from its source [15], Figure 2.13.

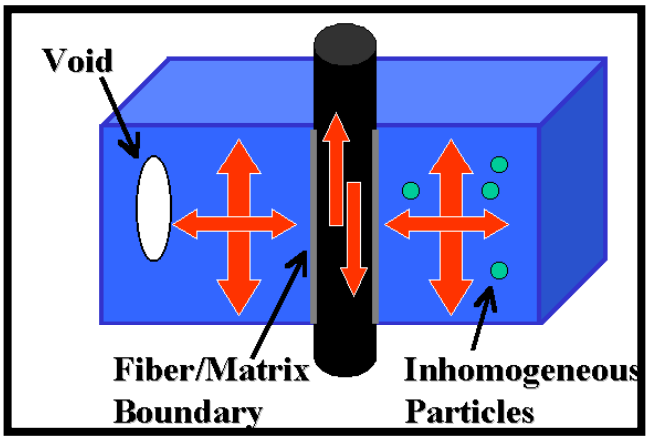

Figure 2.13: Possible Reasons for Scattering in FRP

Despite many of the difficulties associated with AE it is still a useful monitoring technique for FRP. Acoustic energy is efficiently channeled along the reinforcing fibers, which act as a wave-guide for the strain energy [49]. Fiber fractures are energetic events and the displacements associated with a fiber fracture can be detected using transducers. However, fiber fractures cannot be easily distinguished from AE caused by matrix cracking or delamination of FRP sheets using traditional sensors. When monitoring AE in FRP it is reasonable to set the threshold value for monitoring above the maximum amplitude of small amplitude events but below the amplitude of AE from a catastrophic matrix failure [16]. Likewise, many FRP AE experiments use signal amplifiers to magnify the amplitude of events with equivalent thresholds to prevent triggering the system because of insignificant events [8, 15, 16, 50-52]. Results have shown that it is possible to use a network of conventional piezoelectric sensors to monitor a large area and detect significant forms of damage in a structure [22].

Description of the Extrinsic Fabry-Perot Interferometer

The sensor chosen for use in this study was the Extrinsic Fabry-Perot Interferometer (EFPI) manufactured by Luna Innovations. Figure 2.14 is a detailed schematic of the EFPI. The description given here is a summary from a recent article by Duke et al [53].

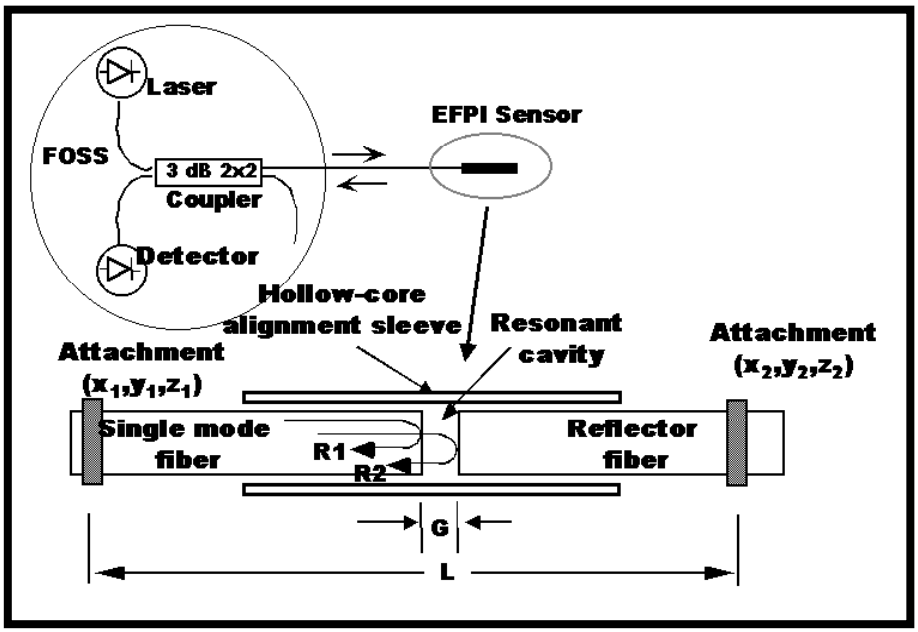

Figure 2.14: EFPI Sensor Diagram

The EFPI sensor is composed of two optical fibers maintained in coaxial alignment by a capillary tube sleeve, and separated by an initial distance G, the gap length. Light from a coherent light source is transmitted through one fiber. At the end of the transmitting fiber, a portion of the light is reflected while a portion of the light exits the fiber and reflects off the face of the reflector fiber. If the fibers are aligned, this reflected light re-enters the original transmitting fiber and interference is developed between these two reflected light beams.

Using the EFPI to Measure Displacement

The best model used to interpret the response of the EFPI is a double-beam, amplitude-splitting interferometer with dielectric reflectors [53]. This model neglects the intensity differences in the two beams due to gap spacing and any phase errors that might result from imperfections in sensor construction. This model is given by

$$V = V_{pp} \cos\left(2\pi \frac{2G}{\lambda}\right) \tag{2.13}$$

where V_{pp} is the peak-to-peak response of the interferometer (including pre-amplifier gain, See Appendix A), G is the gap length, and λ is the wavelength of the laser source. In order to determine the conversion factor between the voltage and gap length we calculate $\frac{\partial V}{\partial G}$, which yields equation 2.14.

$$\frac{\Delta V}{\Delta G} \cong \frac{\partial V}{\partial G} = V_{pp} \frac{4\pi}{\lambda} \sin\left(2\pi \frac{2G}{\lambda}\right) \tag{2.14}$$

The sensor gap is initially set to a value of $G = \frac{n\lambda}{8}$ where $n = 1,3,...$ in order to maximize the sensitivity. To convert measured voltage ΔV to a change in gap distance, ΔG, use the relationship in equation 2.15,

$$\Delta G = \left(\frac{\lambda}{4\pi\ V_{pp}}\right)\Delta V \tag{2.15}$$

For this study λ was 1325 nm, and *Vpp* was measured to be 14 V for the EFPI sensors, which corresponds to 7.53 nm/V for converting detected voltage to change in

gap length. Since the sensor is attached to the surface the change in gap length is directly related to the surface displacement of the two fiber attachment points.

The EFPI sensor is attached by means of epoxy adhesive at a point of attachment on the signal fiber and a point of attachment on the reflector fiber. The sensor is attached, and the middle hollow core alignment sleeve is also anchored with a point of epoxy. After the sensor has been mounted to the substrate, the sensor is heated with a heat gun to a temperature of 300 ºC to melt the plugs of crystalline phenyl salicylate on either end of the alignment sleeve used to hold the fibers in place prior to attachment. References [54-56] and Appendix A provide further notes and recommendations on mounting the EFPI.

As indicated above the output of the EFPI sensor is a function of the change in gap length. Assuming the displacements are small such that the fibers move freely, but remain aligned, the change in gap length, Δd(t) varies with time, ***t***, and is a function of the relative displacement of the attachment points; the fibers do not deform between the attachment points.

$$\Delta d(t) = L(t) - Lo = \sqrt{\left(x_2 + u_2(t) - x_1 - u_1(t)\right)^2 + \left(y_2 + v_2(t) - y_1 - v_1(t)\right)^2 + \left(z_2 + w_2(t) - z_1 - w_1(t)\right)^2} - L_D \quad (2.16)$$

In equation 2.16, L(t) is the distance between attachment points at any time ***t***, Lo is the distance between the attachment points, 25 mm when the plate is not disturbed by the acoustic waves. Since the plate is allowed to deform the initial location of a point is described by its coordinates (1, 2, 3) and its location at some later time is determined by adding to each coordinate the components of displacement at that time (1+u(t),2+v(t),3+w(t)). In the equation above the indices correspond to the attachment points, 1 and 2, or the near end and far end of the sensor cavity.

Benefits to using the EFPI to monitor AE in FRP

There are many potential benefits to using a sensor such as the EFPI when monitoring AE from FRP materials. EFPI sensors can be embedded in composites or can be mounted between layers of FRP laminates. The small size of the EFPI and the epoxy used in mounting it allow the sensor to be placed in small, confined, areas or on vertical surfaces. Since the EFPI sensors are sensitive to surface waves access to the interior of a

structure is not necessary. The EFPI sensor is most sensitive to events that create displacements with components that are parallel to the axis of the sensor [8, 40, 57]. The EFPI is sensitive to off axis displacements, but not to a significant degree as most of the detected off-axis signals are on the order of the noise in the system [40]. A major benefit to using the sensor when dealing with FRP is that the axis of the sensor can be aligned with the major axis of reinforcement. In unidirectionally reinforced FRP composites this feature is very useful. As reported by Chen [49] unidirectional fibers act as wave guides and the longitudinal mode of a propagating stress wave can be detected more efficiently and will undergo less signal attenuation in the composite material. This makes the EFPI an ideal sensor for monitoring the major damage mechanism of interest: fiber fractures. Also, because the EFPI relies on the transmission of light through fiber optic cable the sensor is immune to electromagnetic radiation and interference, such as the kind caused by automobiles and other highway traffic that use bridges.

Perhaps the greatest benefit is that the components of displacement related to relevant damage in the material occur primarily parallel to the surface of the FRP sheet with very little out of plane (normal to the surface) displacement. For example, a fiber fracture can produce displacements in the 1, 2 and 3 directions meaning that out-of-plane and in-plane displacements are generated. However, the displacements that are in plane travel faster, and experience less signal attenuation in FRP and indicate that significant damage is occurring in the material. Large amplitude out-of-plane displacements are generally associated with such events as delamination and cracking between the layers of FRP or from the surface of the reinforced structure. While conventional AE sensors can detect all types surface displacements, they are not designed to be optimally sensitive to in-plane displacements, nor can distinguish in-plane from out-of-plane displacements. Furthermore, many out-of-plane sensors are affected by the velocity of the displacement, which makes it difficult to distinguish between similar damage mechanisms if the strain propagates at different rates. If a sensor is to be a useful part of a health monitoring system it must be able to detect the in-plane displacements that occur prior to catastrophic failure of the material. The EFPI is uniquely suited for this purpose.

Approximations of AE Wave Velocity in FRP materials

A rigorous method of determining the phase and group velocity of specific kinds of waves requires solving the Christoffel's equation for eigen-values and vectors as mentioned previously. References [15, 17, 23, 24, 41, 42, 45, 58] give a detailed explanation and numerical methods for the solution of wave speeds in anisotropic materials. However, it is useful to be able to approximate the velocity of a longitudinal or transverse wave when designing experiments. This can be accomplished using the relationships between the density and directional stiffness for a material. Such relationships generally involve density, ρ, Young's Modulus, **E**, and Poisson's Ratio, μ, in FRP. Equation 2.17 gives an estimate of the longitudinal wave velocity.

$$V_l = \{\frac{E(1-\mu)}{\rho(1+\mu)(1-2\mu)}\}^{1/2} \tag{2.17}$$

It is important to note that although Equation 2.17 can give a fairly accurate estimate it also gives a double root with both a positive and a negative value. The actual wave speed in FRP for any specific mode must be verified experimentally. Equation 2.18 gives an estimate of the transverse mode velocity.

$$V_s = \{\frac{E}{2\rho(1-\mu)}\}^{1/2} \tag{2.18}$$

Equation 2.19 calculates the velocity of a Rayleigh wave based on the transverse mode estimate.

$$V_r = V_t\{\frac{0.87\mu + 1.12\mu}{1+\mu}\} \tag{2.19}$$

It was assumed that there would be many sources of signal loss in the material due to the nature of fiber reinforced composites. Although, observing the signal loss as a function of distance is a good approximation of the signal attenuation in a composite material [16]. Using these estimates, the required size of coupon samples and other experimental variables can be determined without detailed analysis prior to beginning experiments. It has also been reported that the origin of the AE source can be determined by measuring the velocity of the wave mode and using the elastic properties of the composite constituents to verify which material originated the displacement occurred [50]. Although it is theoretically possible to make statements regarding the origin of

displacements relative to wave speeds in large scale and simple composites, for instance with large diameter fibers and low fiber fractions, it is doubtful that this method could be applied in many practical or realistic scenarios.

Deformation and Damage leading to AE in FRP Samples

There are many possible reasons why AE would occur in FRP samples. For instance, fiber pull-out from the matrix, crack propagation through the matrix or through a fiber, delamination between the layers. All types of damage that can cause a spontaneous release of energy from the material in the form of a stress wave will generate AE [44]. However, some damage mechanisms and deformations may not be possible in a specific type of material because of fiber direction or the number of plys. For example, damage typically seen in cross-ply samples might not be observed in unidirectionally reinforced composites. See figure 2.15 for a representation of the MBrace FRP test sample cross-section. In figure 2.15, the "A" layer represents the carbon fiber/epoxy resin matrix and the "B" layer represents the polymer primer layer. AE signals resulting from damage that occurred in different parts of the sample would not only look different but also have different ranges of frequency and amplitude.

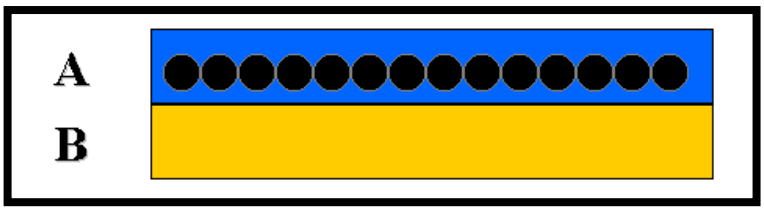

Figure 2.15: Mbrace FRP Cross Section

However, determining what a fiber fracture signal "is" and what characteristic appearance it might have is not a simple matter. It is possible to report the results of a number of experiments in order to classify the type of signals observed and the response of the EFPI in comparison to other types of sensors. But it is difficult to design any experiments to verify the occurrence of a single fiber break. In a piece of carbon fiber reinforced polymer (CFRP) laminate, there may be as many as 2.5 million fibers in a 60 cm wide section [59]. See figure 2.16 for a micrograph of a CFRP laminate. The existence of one or two fiber ruptures in such a large amount of bundle fibers is the proverbial "needle in a haystack."

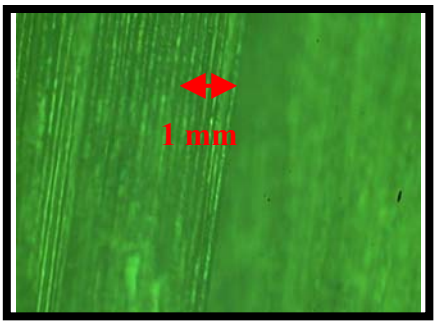

Figure 2.16: CFRP Laminate Micrograph

There are several possible approaches to this problem. A potentially useful approach is to design a series of experiments that will produce fiber fracture in the material under varying conditions and record and compare the AE signals form those events [12]. By process of elimination and comparison of the data set the amplitude, frequency and characteristic shape of a fiber fracture AE signal can be determined. Although modeling options exist, due to the extreme complexity of the boundary conditions the problem is often reduced to its ultimate extent and then scaled up [27]. In the first approach, it is not possible to verify the existence or occurrence of single fiber fractures, but only of fiber bundles rupturing simultaneously. In the second approach, the applicability of the small ideal samples to larger, more realistic structures is questionable. However, by using concepts from both experimental designs, the data from an ideal experiment can be compared to the data from a large sample in order to determine the character of fiber fracture signals and verify the smaller scale results on a larger structure. This can be accomplished by establishing a set of criteria or data ranges for a particular form of damage or displacement in ideal conditions and then comparing the ideal data to other scenarios with similar boundary conditions and materials.

Observing and Modeling Fiber Fracture in FRP

The problem of detecting fiber fracture in polymeric materials has been closely followed by the search for an accurate method of modeling fiber fracture in FRP. With the advent of powerful computers with increased processing capacity and speed, more complex wave surfaces and boundary conditions can be modeled. The computational details of designing and validating relevant models are discussed in the literature [24, 25, 27, 30, 41, 42, 60-63]. Overall, two different approaches have been taken in order to

develop a realistic and useful model of fiber fracture in FRP. Most research has focused on either micro-processes involved with AE in composite materials (i.e. micro-cracking, dispersion, strain release rates, etc.), or the research has used larger test samples and characterized the micro-processes and failure mechanisms in order to generally apply the model to large scale structures.

Bohse [50] used AE to characterize micro-failure processes in simple multiple fiber test coupons and compared the experimental results with a finite element model (FEM). Different damage mechanisms were studied using various coupon configurations and correlating the intrinsic frequencies of stochastic processes in the coupons using the different elastic properties of the materials in the coupons. Chimenti and Auld [64] studied the effect of micro and macro-structural dispersion of guided waves in solids based on crystalline models and applied the results to fibrous composites with plate geometries. Dietzhausen et al [60] used an FEM model to represent a single brittle fiber with different material constitutive laws applied to the model. The different material models used were linear-elastic, non-linear elastic and elastic plastic. Each case was compared to AE data from the tensile loading of single fiber/epoxy coupons monitored by four piezoelectric sensors. While there was reasonable agreement between the models and the data, the small scale and two-dimensional nature of the FEM model limits the applicability of the results to large-scale structures.

However, qualitative and quantitative evaluation of the damage due to loading in FRP can be approached at a larger scale. For instance, Mitzutani et al [61] compared the results of laser generated Lamb waves with known source characteristics to the AE detected from loading a 60 mm by 85 mm cross ply CFRP sample. The results were also corroborated with an ultrasonic C-Scan of the test samples. This method allowed the classification of signals representing different damage phenomena in the composites. Other attempts to classify fiber fracture in composites have used theory to deconstruct experimental data in order to determine trends and then associate those trends with different damage mechanisms. Valentin et al [12], reported a method to detect the presence of matrix micro-cracks and fiber fracture using amplitude analysis of collected AE signals. Their approach used a differential histogram to compare the relative slopes of high-count signal amplitude values to determine which peaks in the histogram were

representative of which type of damage. Although the composite they used had some processing concerns which led to a higher than anticipated number of low amplitude events, they obtained good fit using this method to correlate damage with AE signals in predicting the life of the composite samples.

Aberg and Gudmundson [52] developed a laminate model with infinite length and free edges to characterize different AE from damage mechanisms in composites using stiffness and volume forces to derive the associated displacements. Aberg [51] later used this model to numerically model the acoustic emissions in laminated tensile test specimens. By applying the model to the given loading and boundary conditions, he was able to generate a series of ideal scaled displacement curves as a function of time in the direction of independent unit normal vectors for a Cartesian coordinate system.

The results from these and other papers reveal two important facts. Qualitative characteristics are important and agreement in signal character between the model and the experiment should be verified before any further work is done. Second, quantitative AE results vary widely depending on the scale and composition of the composite sample as well as the method of loading the sample. However, several papers were in agreement regarding a few key points on qualitative and quantitative analysis of AE signals from FRP. First, the amplitude of signals corresponding to matrix micro-cracks can vary from 25 dB to 45 dB, but will typically occur at a lower amplitude value than fiber fracture. Second, the amplitude values for important types of damage mechanisms were similar. Both Bohse and Dietzhausen reported signal amplitudes in the neighborhood of 60 dB for unidirectional single ply carbon fiber fracture. Although Valentin reported a value of 40 dB for CFRP fiber fracture, he used cross ply samples and commented that he expected higher values for unidirectional samples. Third, the method of curing the samples is crucial since rapid curing or incomplete curing of the samples will introduce micro-cracking and significant differences between numerical results and experimental data. Lastly, interfacial debonding and bulk damage mechanisms (such as crack growth through fibers and matrix) tend to occur at higher amplitude values relative to fiber fracture [12].

The most useful quantitative methods of assessing the results of AE tests are viable for either unidirectional or cross ply materials and were commonly applied in each

paper, although different results were reported in each case. The cumulative signal energy and number of events can be used to calculate the stress in the sample at failure, which is useful in proof testing and life prediction [12, 26]. Furthermore, the increase in the cumulative signal energy over time can be used as an indication of the rate of damage accumulation in a specimen [50].

It is useful to consider the literature results within the context of this work. The amplitude values for fiber fracture as detected by traditional piezoelectric sensors can be used to verify the existence of fiber fracture in a sample. Also, if a piezoelectric sensor and an EFPI were attached to a piece of FRP and the piezoelectric sensor detected AE and the results were consistent with the literature, logically the EFPI also detected AE from fiber fracture. While the results from the EFPI and the piezoelectric sensor cannot be directly compared, the traditional sensor can validate the performance of the EFPI. However, it should be noted that a direct comparison of amplitudes is not possible since the amplitude of any given signal is dependent on many different factors, such as amplifiers, thermal expansion and contraction of test samples and the exact type of sensor used to detect the signal.

Chapter 3 – EFPI System Characterization

Experimental Purpose

While the EFPI should be suited to the task of monitoring AE in FRP materials, it is necessary to prove that the sensor is in fact an accurate and precise way of detecting displacements. The following experiments were designed with two goals in mind. The first goal was to prove that the EFPI was a reliable sensor and compare it to a known standard so that the analysis of acoustic emissions detected by it could be compared to established criteria and previous work. The second goal was to determine the character and types of signals that correspond to displacements generated by fiber fractures while confirming that the EFPI signal was indeed caused by them.

Materials and Methods

AE Sensor and System Characterization

The signals from the EFPI sensors are evaluated and processed by a Fiber Optic Strain Sensor (FOSS) detection system manufactured by Luna Innovations. A series of tests were performed in order to differentiate FOSS output signals containing noise from output signals composed of experimental data. Similar tests were performed for the NIST sensor and a Physical Acoustics (PAC) R15 sensor. These electrical signals were captured using analog to digital (A/D) sampling with a PC computer based A/D board, manufactured by Gage, with 12 bit voltage resolution using a 25 MHz sampling rate. The FOSS output was evaluated using three different conditions: no sensor attached, a half sensor or cleaved fiber attached, and an EFPI sensor applied to an FRP substrate.

EFPI and Dynamic Finite Element Model Comparison

A 330.2 x 330.2 x 3.175 mm 6061 aluminum plate was used as a test material. Pieces of 0.3 mm (0.0118 in.) diameter (nominal value) 2H pencil lead were broken at three locations, which are listed in Table 3.1, and shown in Figure. 3.01. Two of the pencil lead breaks (PLB) were on the midplane of the edge face and one was on the top surface of the plate. In plates of this thickness, a PLB located on the top surface of the plate will result in a disturbance composed predominantly of fundamental antisymmetric (Ao) Lamb, or flexural plate modes. For a PLB exactly at the mid-plane of the edge face,

the resulting acoustic disturbance consists of the fundamental symmetric (So) Lamb, or extensional plate mode. If the PLB on the edge face is not at the mid-plane, a component of the antisymmetric mode is also expected to be present. To assure that the PLB breaks on the edge face were broken at the mid-plane a 0.012 in.(0.3 mm) wide alignment slot, 0.004 in. (0.1 mm) deep was cut into the edge face at the mid-plane. A shoe for the tip of the mechanical pencil was machined from high density polypropylene (HDPE) to keep the length of the lead and the angle of the break as consistent as possible in accordance with ASTM standards [35].

Two separate EFPI sensors were attached with approximately 2 mm hemispherical drops of epoxy, to the top surface of the plate. The EFPI sensor aligned with the x-axis of the plate is referred to as EFPI-X, and the one aligned with the y-axis, EFPI-Y. These sensors were positioned to postpone the arrival of acoustic wave reflections from the lateral edges of the plate.

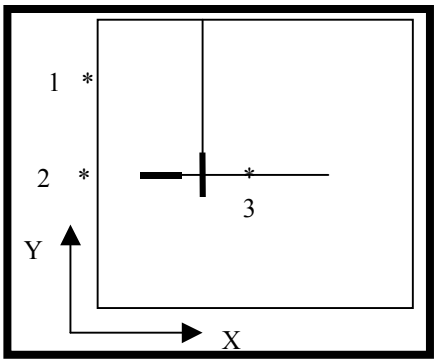

Figure 3.01: Schematic location of EFPI sensors and the three different PLB locations. Note: The Z axis perpendicular to the plane of the page.* PLB locations, EFPI sensor

Table 3.1: Physical Locations of PLB points

x, mm	y, mm	z, mm		description
0	247.65	1.5875		PLB location 1
0	165.1	1.5875		PLB location 2
165.1	165.1	3.175		PLB location 3
88.8	165	3.175		EFPI X- attachment point 1
63.8	165	3.175		EFPI X- attachment point 2
100	171.35	3.175		EFPI Y- attachment point 1
100	146.35	3.175		EFPI Y- attachment point 2

Dynamic Finite Element Model

The dynamic finite element model (DFEM) used in this research has been extensively described [19], and only the details relevant to the current work are repeated here. In the earlier studies, only the out-of-plane surface displacement component was reported. This was because the sensor used for experimental verification, the NIST conical displacement sensor, was only sensitive to displacements normal to the surface plane. It is presumed that the EFPI sensor will respond to only in-plane displacements, which can be predicted by the DFEM.

Stress free boundary conditions were assumed along the top and bottom surfaces as well as along the outer edges of the plate. A source function with temporal variation to approximate that of a pencil lead break as determined by Proctor et al [65] was used. A force of amplitude 1 N was used, which is in good agreement with that produced by the fracture of a 0.3 mm diameter piece of Pentel® 2H lead. For aluminum the density of 2700 kg/m^3, and longitudinal, 6320 m/s^2, and shear, 3100 m/s^2 elastic wave speeds, were used as inputs to the model [65].

For all cases, a plate thickness of 3.175 mm was modeled, where the mesh consisted of equiaxial cells approximately 0.2646 mm on a side, and the region of contact over which the step force was applied was roughly circular with a diameter of four cells. It should be noted that the footprint of the modeled step force, 1.05833 mm, is much larger than the nominal diameter of the pencil lead, 0.3 mm. The results of the analysis were provided as three orthogonal displacements (u, v, and w) that correspond to the three coordinate axes (x, y, and z) calculated at time increments of 0.377 seconds.

As noted by Gary and Hamstad [66] the DFEM models the application of a force with appropriate time history at the location of interest. However, the force condition that corresponds to the experimental PLB is actually a release of a force with such a time history. Therefore the measured displacements are 180^o out-of-phase with that theoretically predicted by the DFEM. For sake of comparison one set of results can be inverted to account for this phase difference.

The test results of each experiment were filtered using either the MATLab Signal Processing toolbox or a LABView Bessel Infinite Impulse Response filter application. See Appendix B for further details about the filter application. All other experimental

constraints and conditions were based on the applicable ASTM standards. See references [34-39].

Definition of Ordinate Percent Occurrence and AE Signal Count

A method similar to counting the total number of AE events is used to evaluate the amplitude distributions from the experimental results in this work. Since many of the tests use different methods of loading FRP coupon samples, the total number of signals from each test can vary by as much as several orders of magnitude. This makes it difficult to compare the results of one experiment to another, even though the same materials were used in the experiment and the damage mechanisms should be similar. In the literature [3, 12, 26, 49, 50], the number of recorded signals and the number of AE counts per signal were within the same range. In situations where this was not the case, such as in Valentin's study of amplitude histograms [12], the AE counts were normalized by the 25th percentile of the average total of events in the record. To compare the amplitudes from each signal equally in this work, an average amplitude distribution for a was calculated by taking the number of times that an amplitude value occurred and dividing it by the total number of amplitude occurrences and summing over the range of amplitudes, see equation 3.1.

$$A_D = \sum_{a=1,n=1}^{a=145,n=i} \frac{A_{an}}{A_a} = \frac{\sum_{n=1}^{i} A_{1n}}{\sum A_1} + \frac{\sum_{n=1}^{i} A_{2n}}{\sum A_2} + \frac{\sum_{n=1}^{i} A_{3n}}{\sum A_3} + \ldots = 1 \tag{3.01}$$

Where $\mathbf{A_D}$ is the normalized amplitude distribution, $\mathbf{A_a}$ is the sum of all amplitude occurrences and $\mathbf{A_{an}}$ is the sum of the amplitude occurrences for a particular amplitude. See figure 3.02 for a sample spreadsheet calculation. In the figure, column *A* corresponds to the subscript value "a" in equation 3.01, and columns *B*-*D* correspond to $\mathbf{A_{an}}$. The total sum below column *E* is the value $\mathbf{A_a}$.

A	B	C	D	E	F
dB	**Signal 1**	**Signal 2**	**Signal 3**	**Sum**	**%**
40	37	56	78	171	0.30
41	12	34	52	98	0.17
42	34	53	53	140	0.24
43	36	52	75	163	0.28

Total Sum 572

Figure 3.02: Sample Percent Occurrence Calculation

This calculation results in a distribution that relates an amplitude value for a specific sensor to the expected percent chance it will occur in an AE signal recorded by the sensor. This is considered the percent occurrence of an amplitude, and multiplying each value in the distribution by 100, yields an ordinate percentage value, with a maximum value of 100 and a minimum value of 0. A signal is considered one voltage versus time record that exceeded the threshold value. The number of AE signals that exceeds the threshold value for a given record of an experiment is the signal count. All other definitions and AE terminology used in this work can be found in the literature [34]. The percent occurrence distribution is used in this work to evaluate voltage output, decibel output and signal frequency. When decibel values are used, the log ratio of the amplitudes is calculated using the equation 3.02.

$$A_{dB} = 20 * Log(A_i / A_{ref}) \tag{3.02}$$

Where $\mathbf{A_i}$ is the positive amplitude of a data point (usually voltage) and $\mathbf{A_{ref}}$ is a predetermined amplitude reference value. A typical reference voltage is 1 microvolt ($1x10^6$ volts).

Results of EFPI System Characterization

AE Sensor and System Characterization

Figure 3.03 is a sketch of the three different sensor configurations. In each case, no external stimulus was used to generate a signal, so the recorded events are purely the result of the sensor/system noise. Figure 3.04 shows the results for the signal amplitudes captured by the FOSS when no sensor was attached. The amplitudes of each signal were rounded to the nearest 10 mV and ordered in 10 mV groups. The resulting histogram clearly shows that 70% of all occurrences have an amplitude between –5 mV and +5 mV,

while a small but significant percentage of signals have fallen within a wider band of ±5 mV to ±15 mV. A small percentage (< 1%) of signals have amplitudes outside of ±15 mv to maximum values of –25 mV and +25 mV.

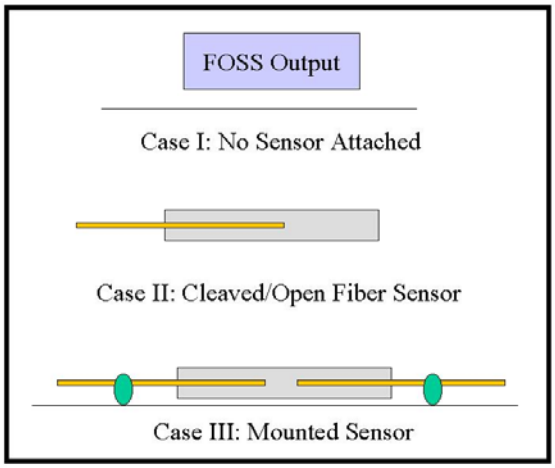

Figure 3.03: Schematic of System Configurations for Cases I, II, III.

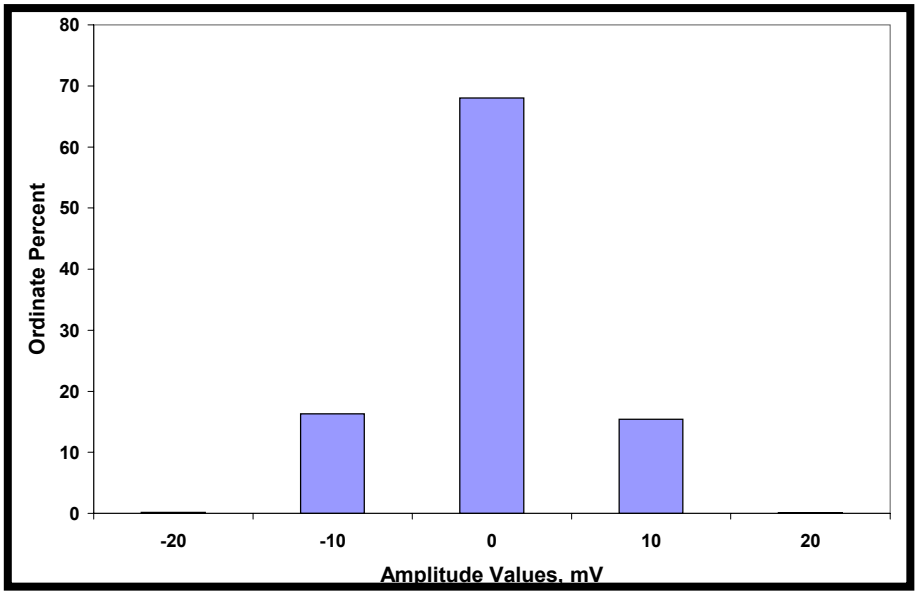

Figure 3.04: Case I Results.

Figure 3.05 shows the amplitude distribution when a cleaved fiber was attached to the FOSS. The amplitudes of each signal were rounded to the nearest 10 mV and ordered in 10 mV groups. The cleaved fiber histogram shows that 86% of all occurrences have an amplitude between –5 mV and +5 mV, while a small but significant percentage of signals have fallen within a wider band of ±5 mV to ±15 mV. A very small percentage (< 0.5%)

of signals have an amplitude range outside of ±15 mV, with maximums at –45 mV and +55 mV.

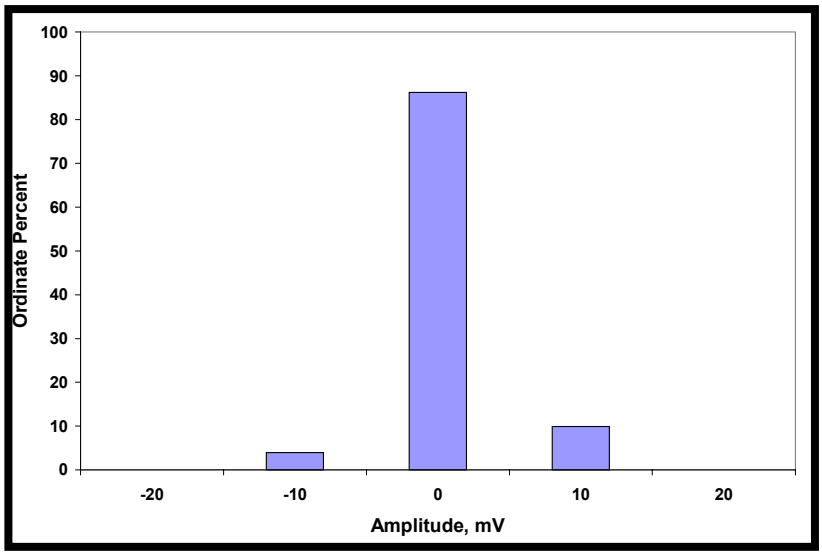

Figure 3.05: Case II Results.

Figure 3.06 shows the results from a FOSS with a mounted sensor attached. Again, the amplitudes of each signal were rounded to the nearest 10 mV and ordered in 10 mV groups. The resulting histogram shows that approximately 95% of all occurrences have an amplitude between –5 mV and +5 mV, while small percentage of signals fall within a wider band of –15 mV to +15 mV. Outside of those groups, no other signal amplitudes occur.

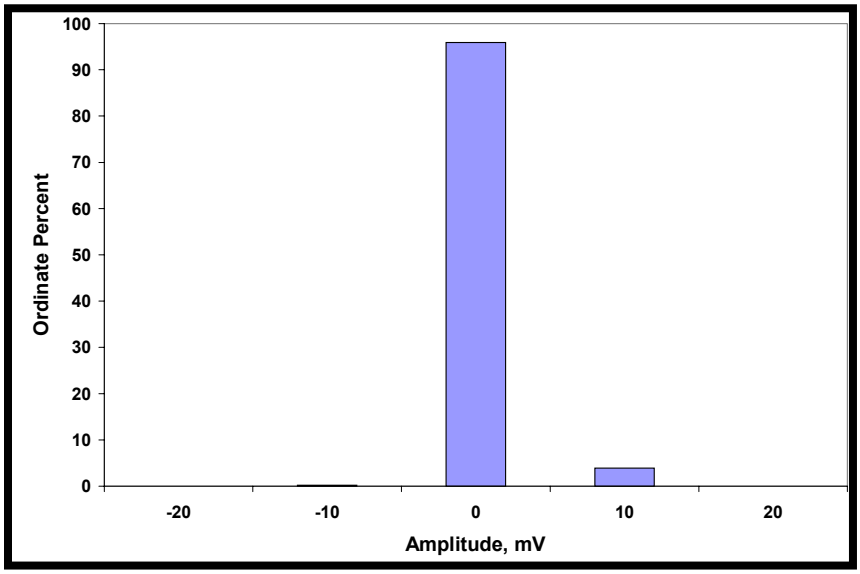

Figure 3.06: Case III Results

The frequency response of the cleaved fiber signals was also examined to determine if the system had a fundamental frequency that might corrupt a data signal. The cleaved fiber was ideal for this because it represented the ideal response of the EFPI before mounting with no refractive interference since it corresponds to half of a sensor. Figure 3.07 is a normalized histogram of the frequencies that were present in the signals from the cleaved fiber experiment. The frequency distribution shows that the signal output of the FOSS and cleaved fiber, without any interference, is approximately uniform.

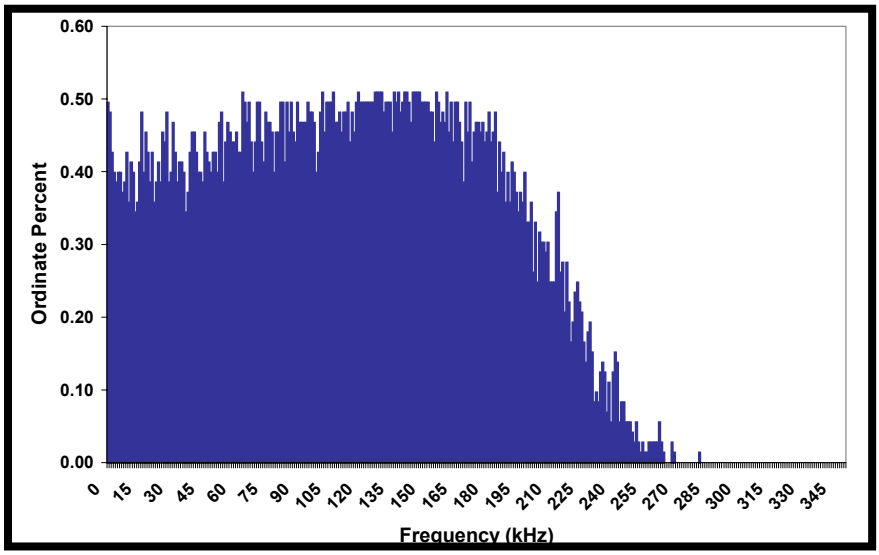

Figure 3.07: Cleaved Fiber Frequency Distribution

Figure 3.08 shows the average noise amplitude distribution for the EFPI mounted on an unloaded FRP sample using a decibel scale. Figures 3.09 and 3.10 show the average noise amplitude distributions for the PAC R15 and NIST sensors respectively. In each graph, the reference voltage for the decibel scale is 1 microvolt (1 x 10^{-6} Volts).

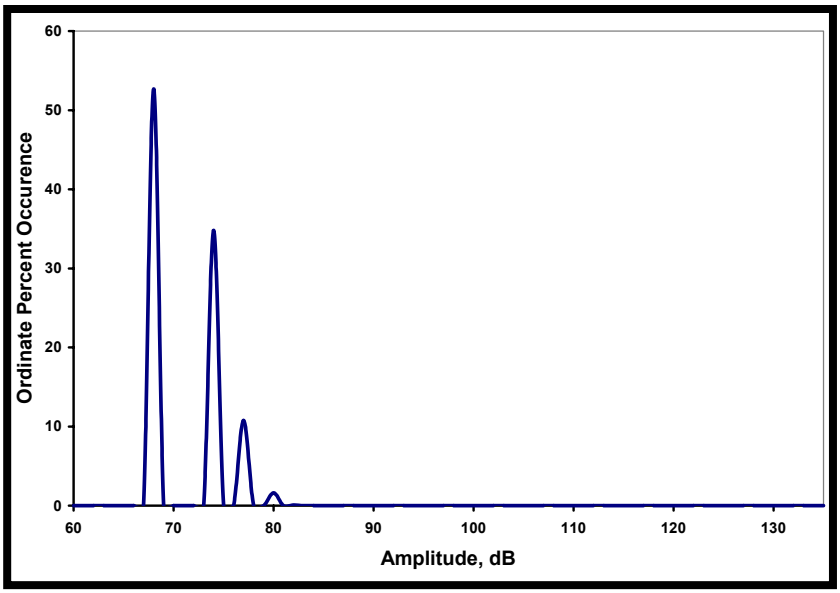

Figure 3.08: EFPI Noise Amplitude Distribution, reference $1x10^6$ volts.

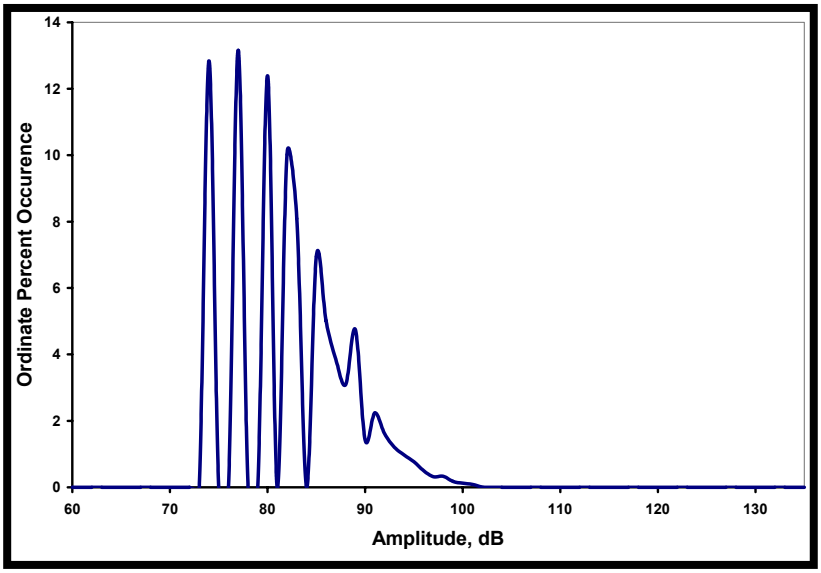

Figure 3.09: PAC R15 Noise Amplitude Distribution, reference $1x10^6$ volts.

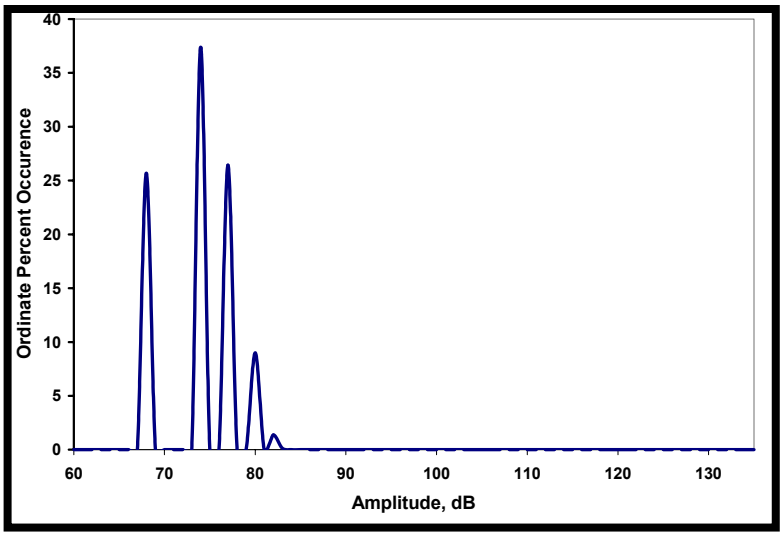

Figure 3.10: NIST Noise Amplitude Distribution, reference $1x10^6$ volts.

EFPI and Dynamic Finite Element Model Comparison

The DFEM predicted displacement components at the three points of attachment for the EFPI-X sensor for a PLB are plotted in Figure 3.11. The data are directly from the DFEM and have not been filtered. It should be noted that there is a significant difference in magnitude for the different displacement components. The u component of displacement is much larger than the other two, and can dominate the predicted, shown in Fig. 3.12, and the observed response of the EFPI sensor.

A.)

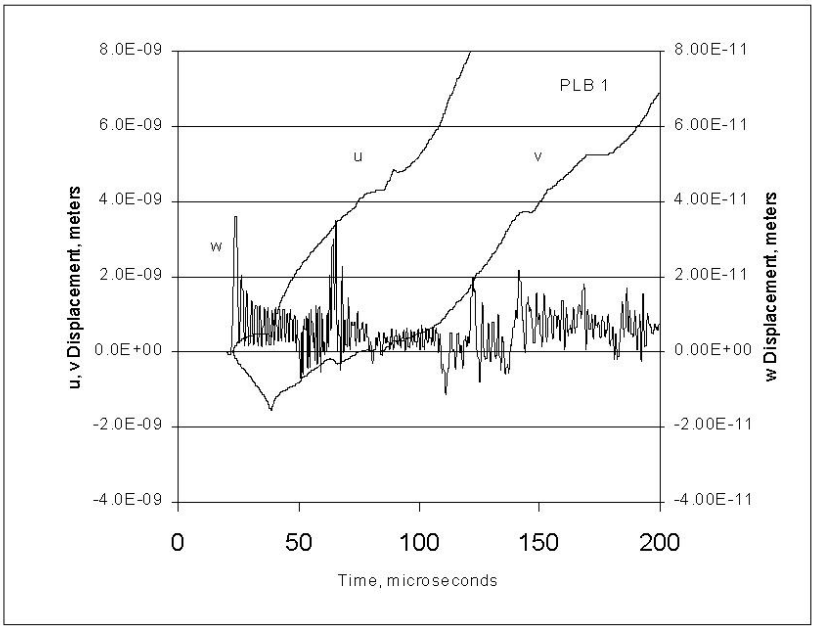

B.)

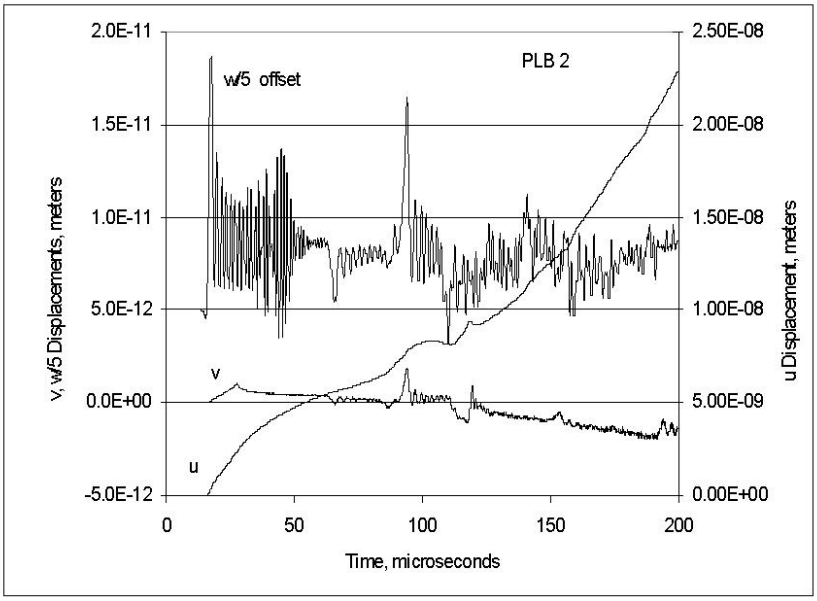

C.)

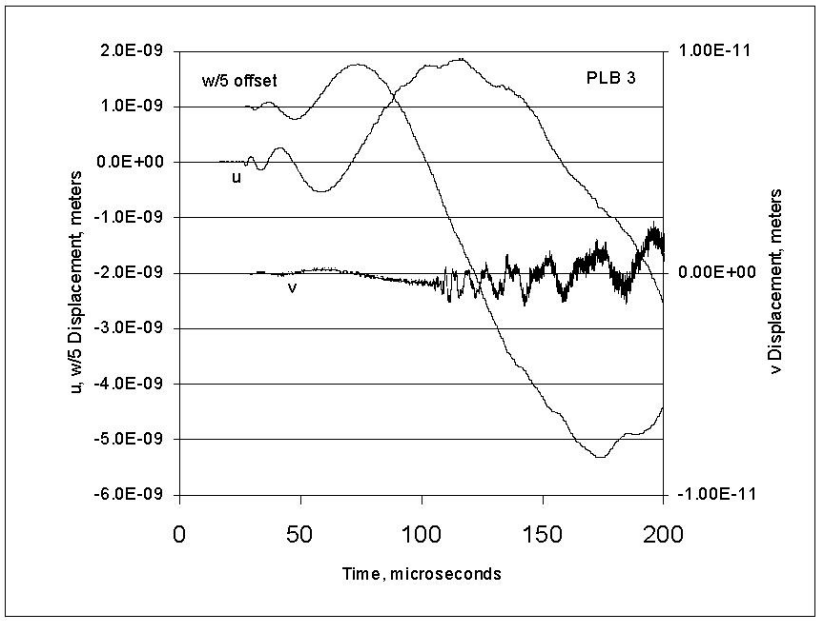

Figure 3.11: Predicted u, v, and w displacement components at the mid point of the EFPI sensor for a PLB at A.) position 1, B.) position 2 and C.) position 3, with w diminished by a factor of 5 and offset.

For the situations considered one of the displacement components tends to be dominant. Figure 3.12 shows that for the PLB 2 and PLB 3 locations the difference in w component mimics the predicted gap change, u2-u1 and the estimated gap change G(t)-Go. This is due in part to the magnitude of the u and w components in these cases and also to the fact that the other components are quite similar at both attachment points at the same instances of time. For situations where the source-sensor location and orientation

relative to the wave propagation are less “symmetric” some differences are to be expected.

A.)

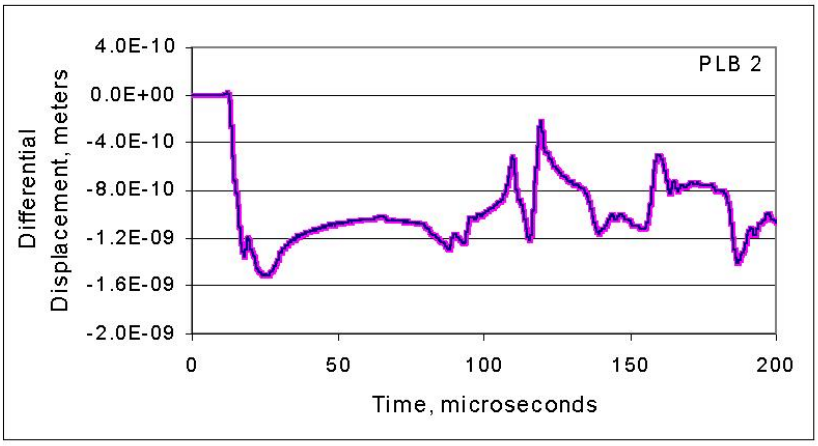

B.)

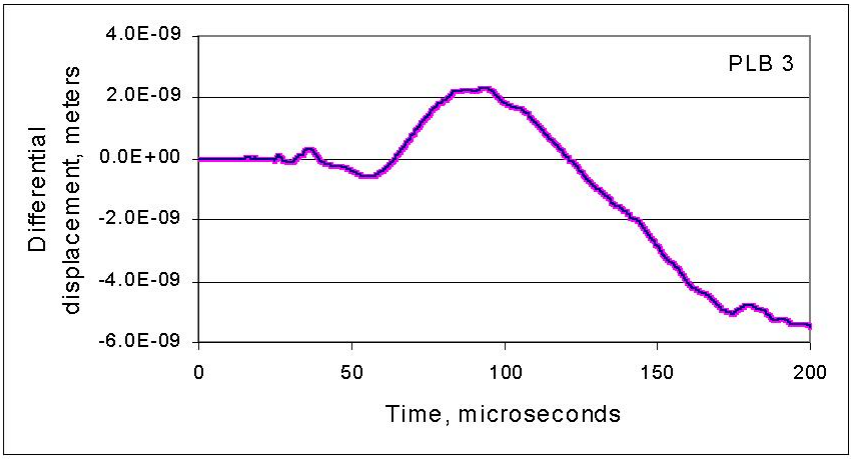

Figure 3.12: G(t)-Go and $u_2(t)$-$u_1(t)$ computed for the two EFPI sensor attachment points caused by a PLB at a) location 2, and b) location 3 illustrating the similarity; the data have not been filtered. In both cases the plots are essentially superimposed.

Although PLB 1 may not be the most asymmetric possible for this plate it is not particularly symmetric. Consequently the EFPI sensor is predicted to respond to disturbances dominated by either in-plane components of displacement or out-of-plane components of displacement, because the response is related to the relative displacement of the epoxy fixed attachment points.

In addition, significant low frequency content is present in the data shown in Figure 3.12. Similar to the NIST sensor the EFPI sensor system is insensitive to the low frequencies on the order of 20 kHz, with wavelengths of approximately 30mm. In order to examine the correspondence between the DFEM predictions and the experimental measurements it is convenient to filter out the low frequencies. Consequently the

experimental and predicted data have both been bandpass filtered using a 4th order Bessel Infinite Impulse Response (IIR) filter from 150-1000kHz, implemented using LabView® software.

Figure 3.13 displays the predicted G(t)-Go and an example of the detected EFPI-X response for each of the three PLB locations. Figure 3.14 displays examples of the response for these PLB locations for the EFPI-Y sensor. The amplitude of the signals is believed to be important when noting the correlation between them. However, for situations where the signal to noise ratio is better, Figure 3.13b and c, the correlation seems to be good.

A.)

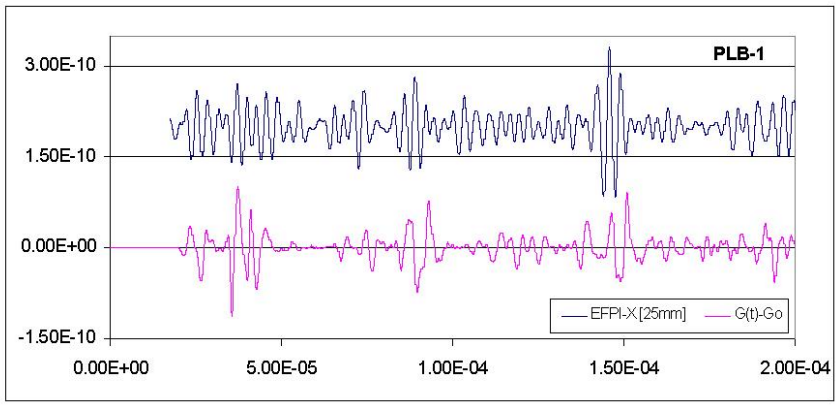

B.)

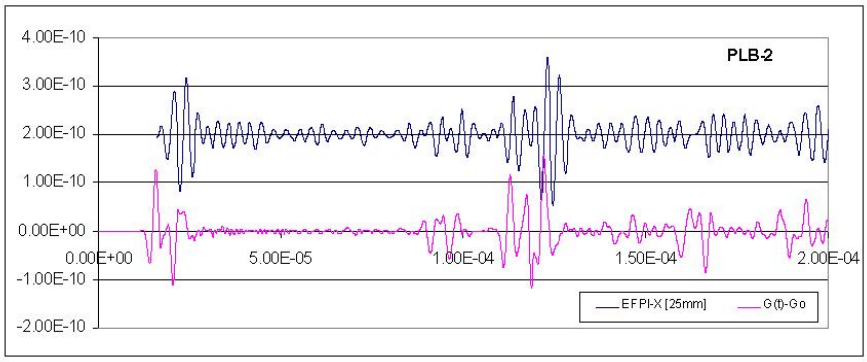

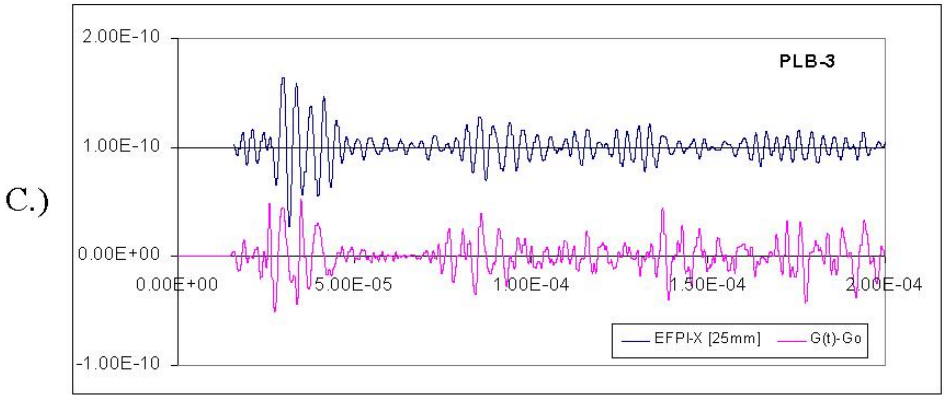

Fig. 3.13: Predicted change in gap and the response of the EFPI sensor with attachment points 25 mm apart, oriented parallel to the x-axis, for PLBs at a) location 1, b) location 2, and c) location 3.

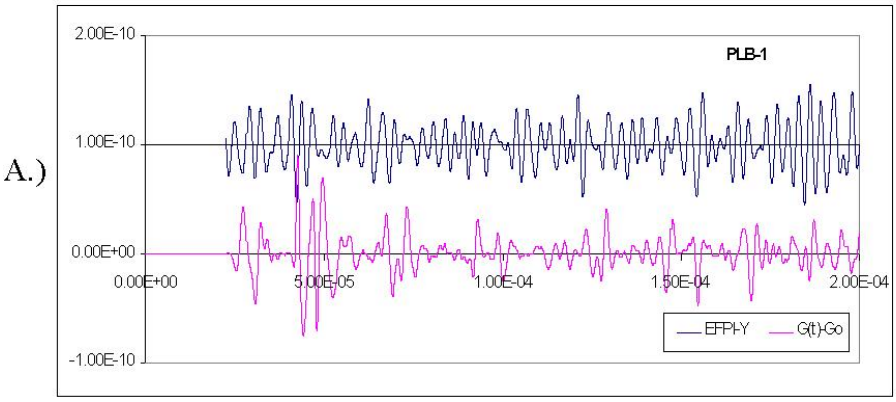

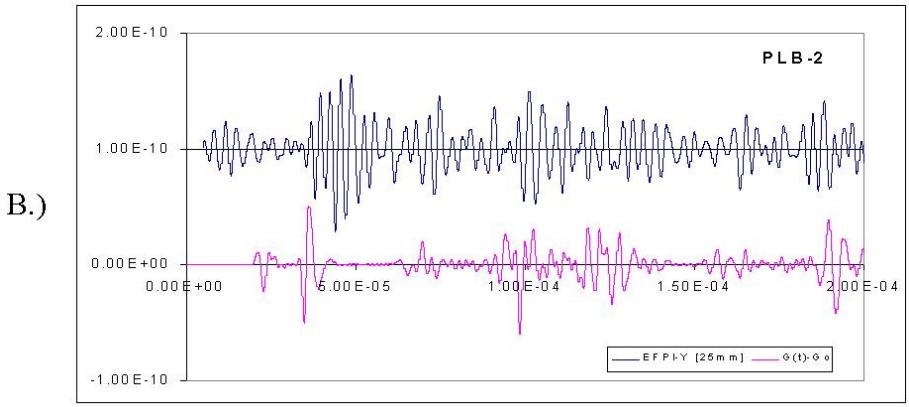

C.)

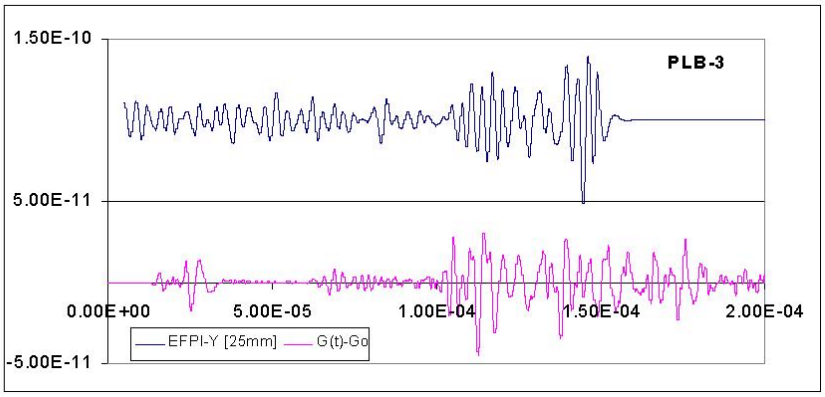

Figure 3.14: Predicted change in gap and the response of the EFPI sensor with attachment points 25 mm apart, oriented parallel to the y-axis, for PLBs at a) location 1, b) location 2, and c) location 3. The flat line response after about 160 microseconds is due to no data being collecting for this PLB after that point in time.

A.)

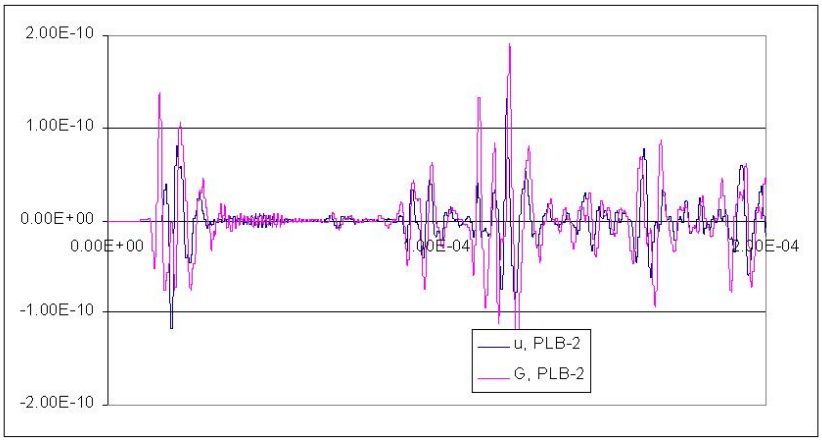

B.)

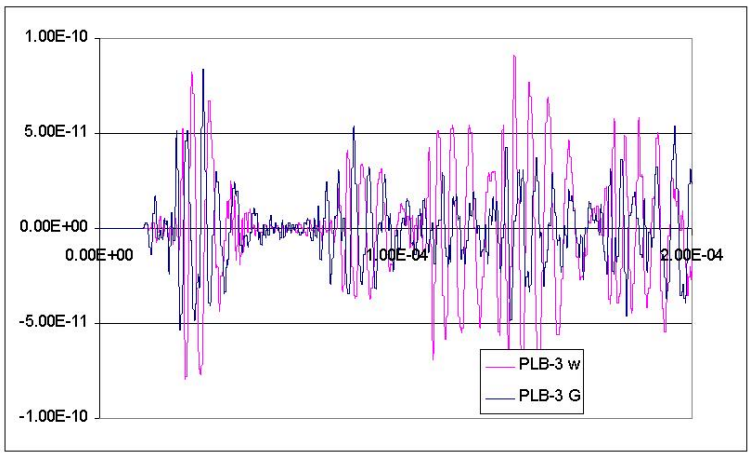

Figure 3.15: Dominant displacement components predicted for a PLB-2 (u) and PLB-3 (w) and predicted change in gap for an EFPI sensor oriented parallel to the x-axis versus time.

Figure 3.16 displays the amplitude distributions from the predicted displacement components at the PLB 1, 2 and 3 positions for the U, W, G(t)-Go. The G(t)-Go and W

distributions closely mimic the expected response of the EFPI and NIST sensors at those locations and give insight to how the signal amplitudes of the sensors compare to each other. The amplitude distribution of the U displacement is useful to look at because it is the displacement direction of interest with respect to the EFPI.

A.)

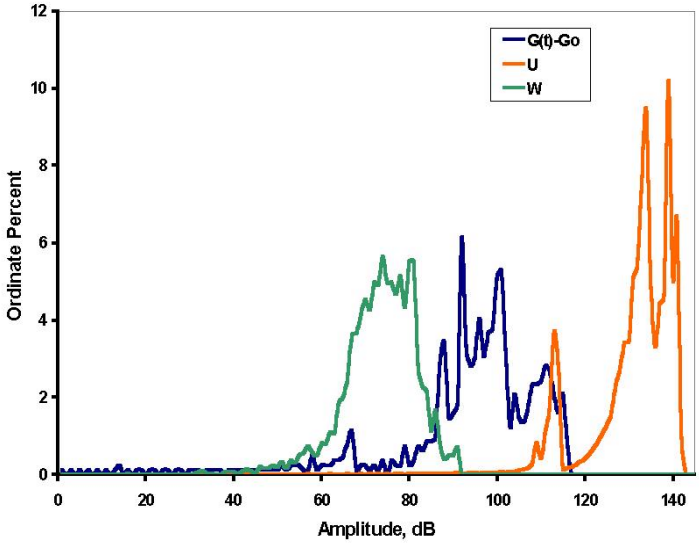

B.)

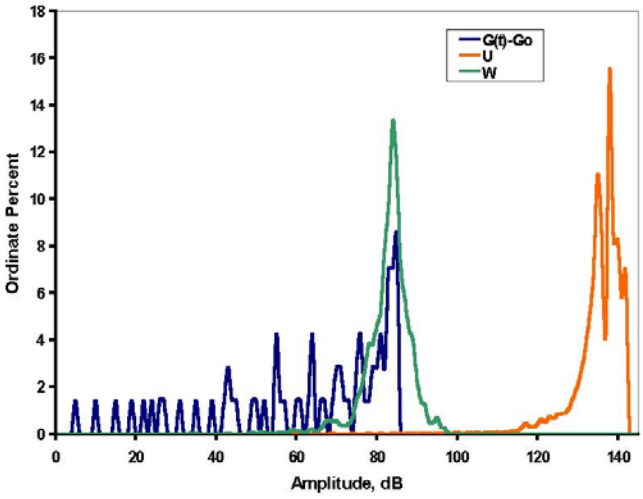

C.)

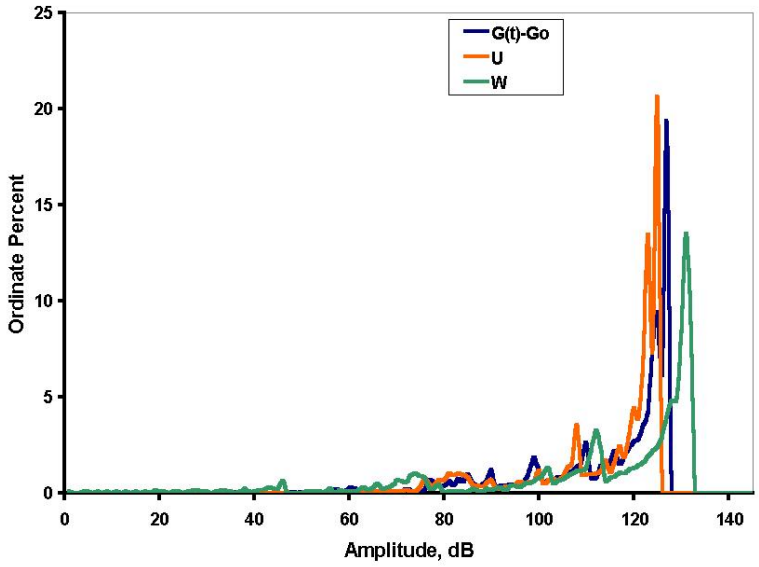

Figure 3.16: Distributions for predicted U, W, G(t)-Go displacement at PLB positions 1,2,3, reference $1x10^6$ volts.

Discussion of EFPI System Characterization Results

Discussion of Sensor and System Characterization

The results of the experiments indicate that neither the raw output of the FOSS or the EFPI have any significant frequency or amplitude characteristics that might corrupt the detected AE signals. However, the background noise from the EFPI is very uniform and can be easily removed from a detected signal by simply subtracting the percent occurrence of the decibel amplitude values. The results also indicate that the system has a strong tendency towards zero, and the most likely value for a mounted sensor is zero volts. Given the large number of samples it is not unreasonable to assume a normal distribution for the amplitude values and fit a curve to the histograms. Figure 3.17 compares the amplitude distributions from each case, using curves instead of bins to represent the data, disregarding the amplitudes that occurred less than 0.1% of the time.

Comparing the different discrete distributions it is clear that the 0 mV peak occurs less frequently in a mounted active sensor than an open circuit condition. The amplitude distributions for both the cleaved fiber and the FOSS without a sensor attached fall outside the mounted active sensor distribution. The increased occurrence of the FOSS without a sensor to have a greater chance of a wider distribution can be attributed to unfocused light reflecting at the connection point for the sensor which may account for

higher amplitude peaks in the output signal. However, with a wave-guide (i.e. optical fiber) to channel the FOSS signal, the output signal becomes more narrowly centered at 0 mV with a much smaller chance of a wide distribution. It is important to note that the signal amplitudes from the attached sensor signals have a greater chance of occurring at zero volts than either the cleaved fiber or no sensor case. This means that the sensor itself does not add any significant character to a signal and that the system noise actually decreases when the sensor is applied.

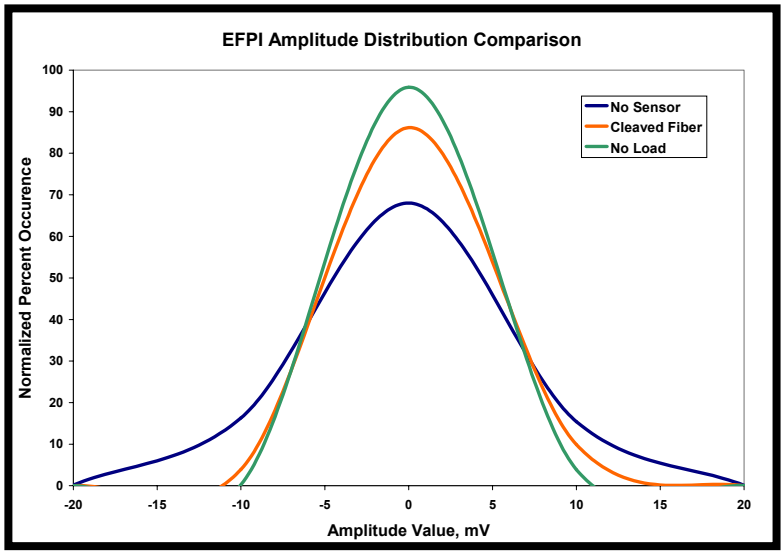

Figure 3.17: Normal Curve Comparison of Cases I, II, III

Discussion of EFPI and Dynamic Finite Element Model Comparison

The dominant displacement component for the PLB-2 and PLB-3 breaks can be correlated with the corresponding change in gap length, which is directly related to the EFPI-X sensor response. Figure 3.15 a) suggests that for essentially the entire record close correspondence is predicted, while b) suggests that for a PLB-3 the predicted correspondence is good until reflections from distant boundaries arrive at the sensor. For these situations the initial qualitatively response of the EFPI sensor is predicted to correlate with the dominant component of surface displacement in the vicinity of the sensor. The qualitative response with time exhibited in Figure 3.13 b and c are consistent with this suggesting that the EFPI response has greater fidelity when the displacements induced by the acoustic disturbance are dominated by a single component.

The EFPI sensor is sensitive to displacements associated with PLBs that have been used to simulate AE sources. The EFPI response is dependent on the change in gap

length between the points of attachment, which in some instances is dominated by the parallel in-plane component for PLBs exciting symmetric plate modes and in other instances is dominated by the out-of-plane component for PLBs exciting flexural plate modes.

The amplitude distributions suggest that for the PLB 1 position, the NIST and EFPI have different ranges of signal response with a range of significant amplitude values in common from 60-90 dB, Figure 3.16a. However, the distributions from the PLB 2 and 3 locations suggest that both sensors should respond similarly, even though they are optimally sensitive to different displacement components, Figure 3.16b, c. In cases where the distance from the source to the sensor are similar to the PLB 2 position and the source is primarily in-plane and on-axis with the sensors the amplitude distributions of both the NIST and EFPI should be very similar. For the PLB-2 position, the most frequently occurring amplitude value for the G(t)-Go distribution is 85 dB whereas for the W distribution it is 84 dB, Figure 3.16b. This is interesting because it is counter-intuitive to expect the NIST and EFPI sensors to behave the most similarly for an in-plane on-axis displacement where the EFPI should be the most sensitive. However, these results may be different in materials where signal attenuation is a significant factor.

Chapter 4 – Optical Fiber Break Aluminum Plate Experiment

A 330.2 x 330.2 x 3.175 mm 6061 aluminum plate, with four 125 mm (5 in) lengths of 80 micron optical fiber attached to the plate with epoxy was used as a test material. The fibers were attached on the top surface of the plate and in a 0.3 mm (0.012 in) wide alignment slot, 0.1 mm (0.004 in) deep in the edge face at the mid-plane, Figures 4.01 and 4.02. The optical fibers were oriented parallel to the sensor axis of the EFPI-X. The optical fibers were cleaved to generate AE from a fiber unloading from a fracture. The goal was to gain insight to the behavior of fiber structures unloading which is suspected of being similar to fiber fracture in CFRP composites. Each of the optical fibers were pulled taut and then cleaved with an optical fiber blade in 12.7 mm increments. The AE from the cleaved optical fiber was compared to the displacements generated by the DFEM. See chapter three for a detailed explanation of the DFEM and the model generated components of displacement.

The NIST and EFPI sensors were used to monitor the AE from the optical fiber breaks. The EFPI was attached with approximately 2 mm hemispherical drops of epoxy, to the top surface of the plate. These sensors were positioned to postpone the arrival of acoustic wave reflections from the lateral edges of the plate, Figure 4.01.

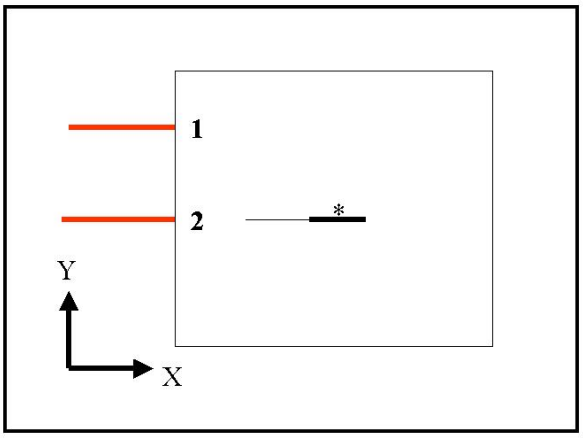

Figure 4.01: Schematic location of EFPI sensors and the three different PLB locations. Note: The Z axis perpendicular to the plane of the page. * NIST Sensor location, EFPI sensor ▬▬

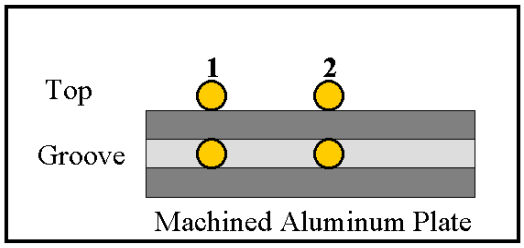

Figure 4.02: Side view schematic of optical fiber locations

Results of Optical Fiber Break Aluminum Plate Experiment

The EFPI and the NIST sensors detected displacements that were generated by optical fiber breaks (OFB), or the cleaving of telecommunications grade optical fibers attached to an aluminum plate. Figures 4.03 and 4.04 are graphs of typical sensor output over time from the broken fibers that were attached to the groove at position 1. Figures 4.05 and 4.06 are graphs of typical sensor output over time from the broken fibers that were attached to the top surface of the plate at position 1. Figures 4.07 and 4.08 are graphs of typical sensor output over time from the broken fibers that were attached to the groove at position 2. Figures 4.09 and 4.10 are graphs of typical sensor output over time from the broken fibers that were attached to the top surface of the plate at position 2.

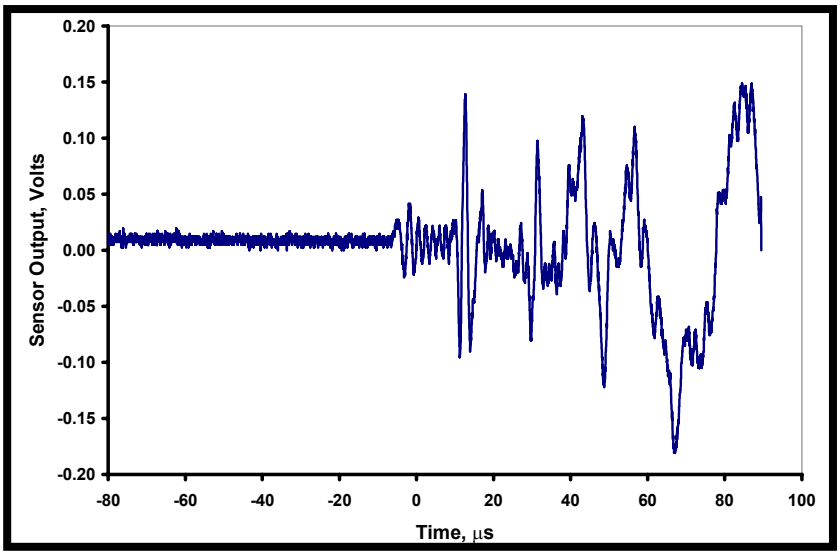

Figure 4.03: NIST, Position 1, Groove Break

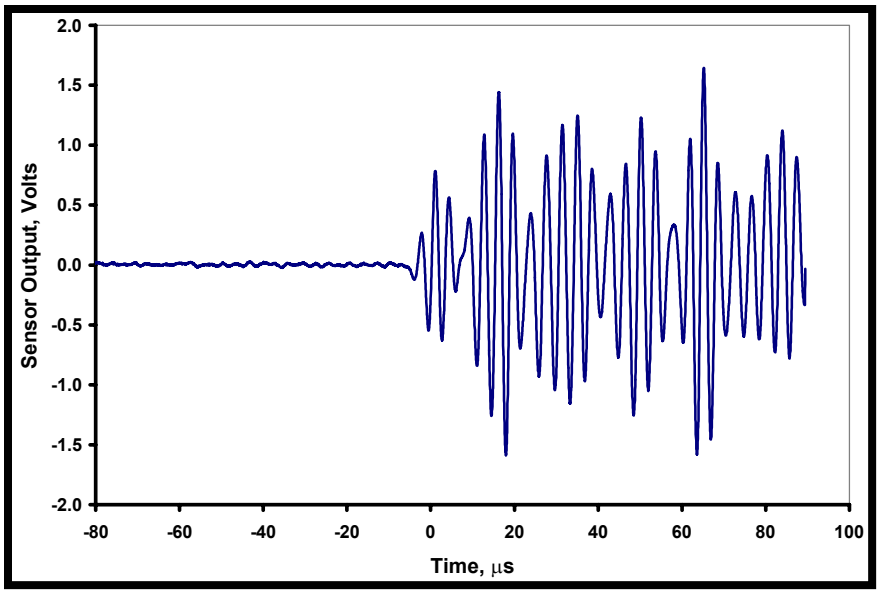

Figure 4.04: EFPI, Position 1, Groove Break

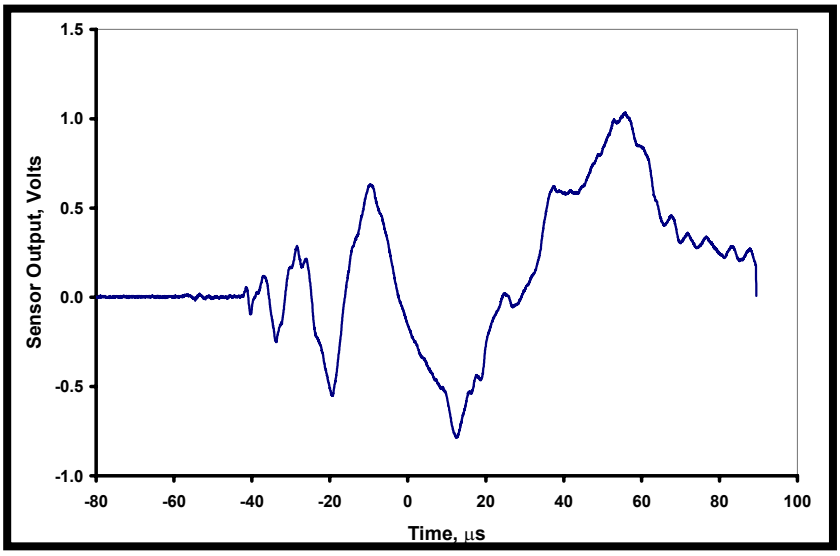

Figure 4.05: NIST, Position 1, Top Break

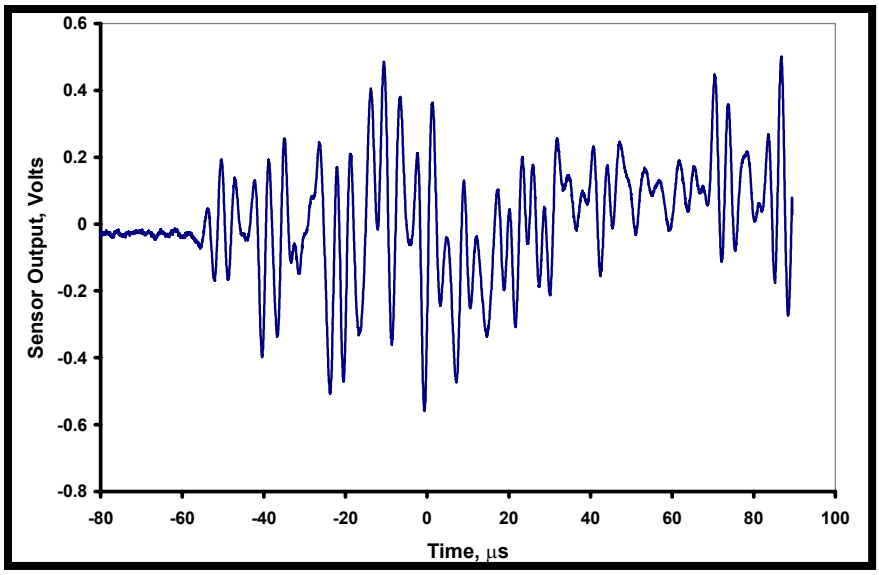

Figure 4.06: EFPI, Position 1, Top Break

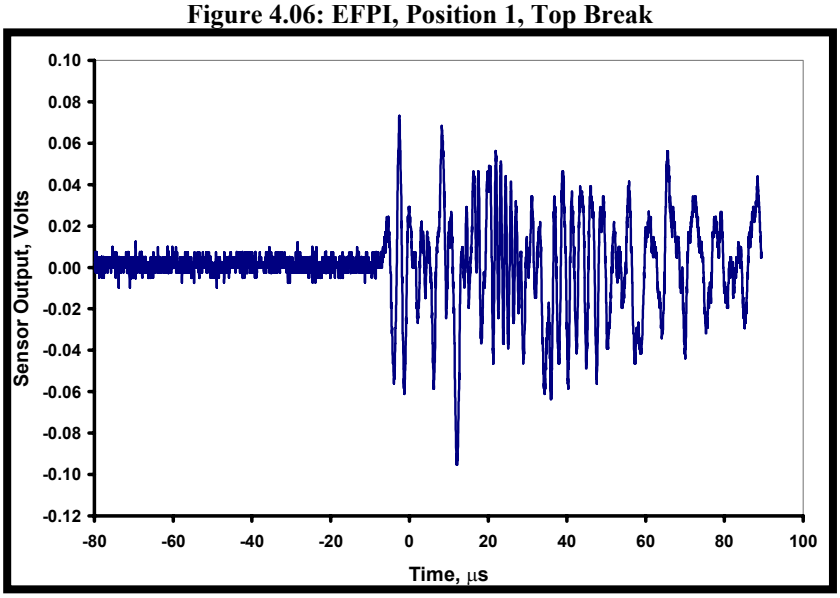

Figure 4.07: NIST, Position 2, Groove Break

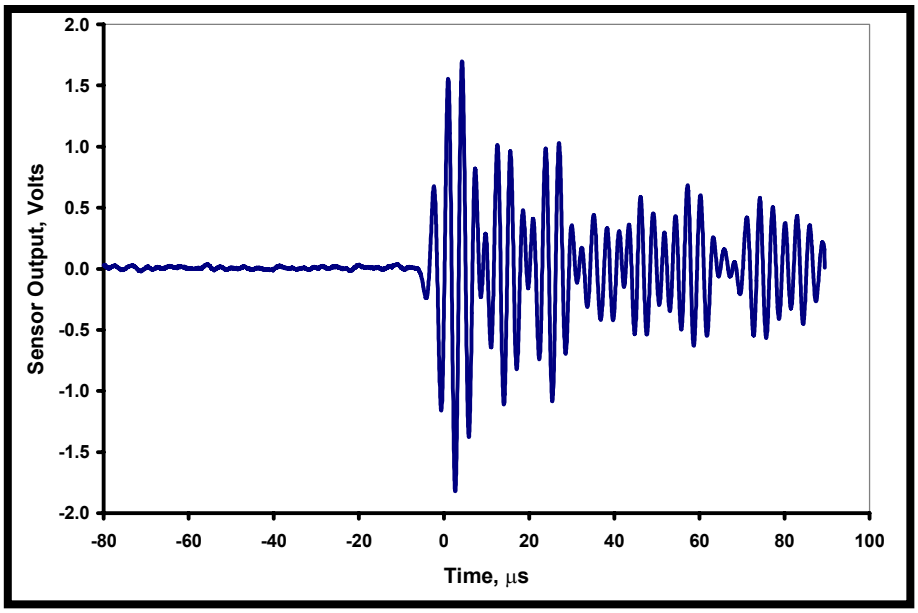

Figure 4.08: EFPI, Position 2, Groove Break

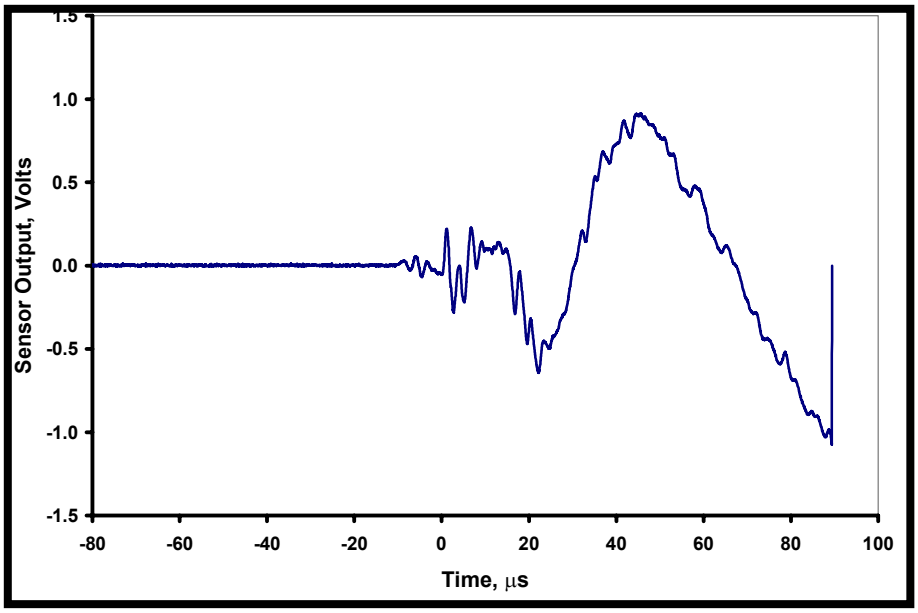

Figure 4.09: NIST, Position 2, Top Break

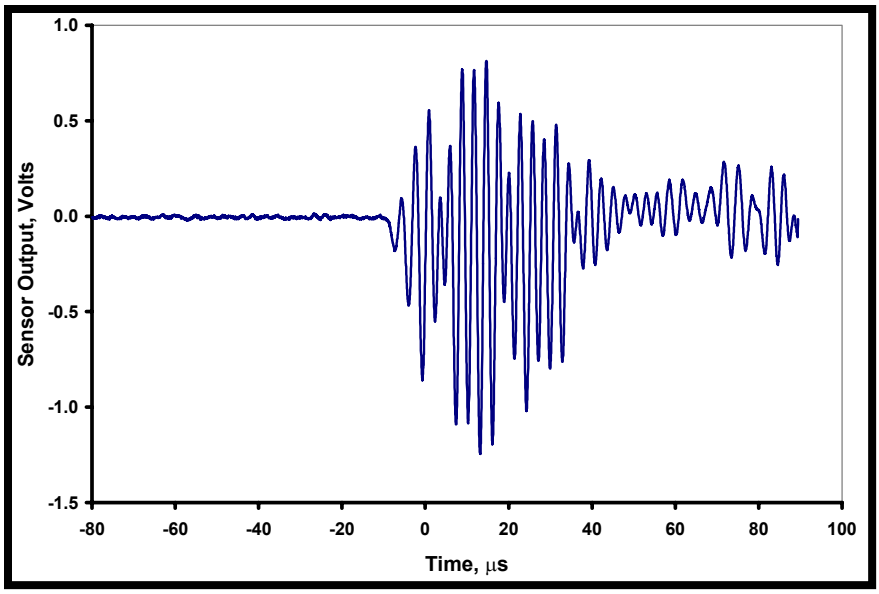

Figure 4.10: EFPI, Position 2, Top Break

Overall, the EFPI output was greatest for in-plane events that occurred at the mid-plane of the plate. The NIST output was smaller than the EFPI for all in-plane sources but it had a larger response to displacements caused by fibers attached to the top surface of the plate. The amplitude distributions of the sensors for the various OFB locations had a small margin of error, with the most frequently occurring amplitudes below 90 dB. Error bars for each distribution are shown in red. Figures 4.11 and 4.12 are the NIST amplitude distributions for position 1. Figures 4.13 and 4.14 are the EFPI amplitude distributions for position 1. Figures 4.15 and 4.16 are the NIST amplitude distributions for position 2. Figures 4.17 and 4.18 are the EFPI amplitude distributions for position 2.

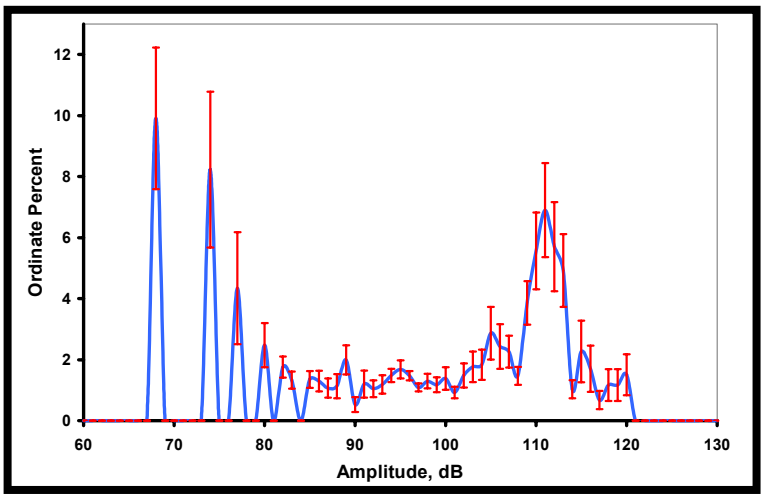

Figure 4.11: NIST Amplitude Distribution, Top break position 1, reference $1x10^{-6}$ volts

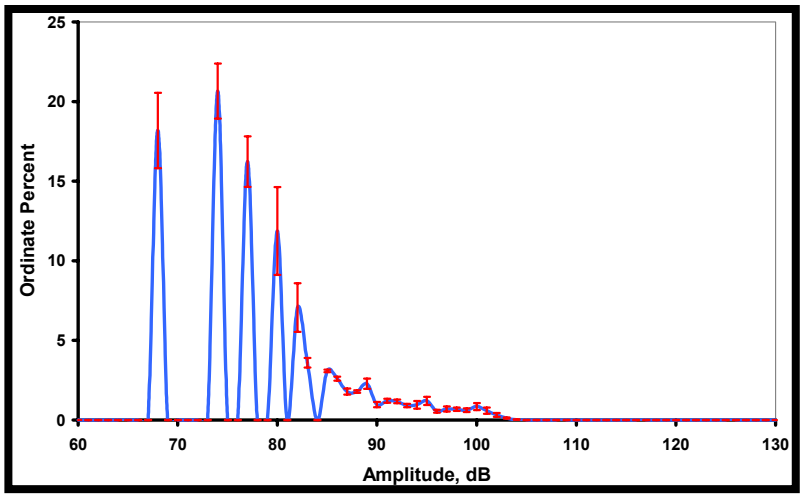

Figure 4.12: NIST Amplitude Distribution, Groove break position 1, reference $1x10^{-6}$ volts

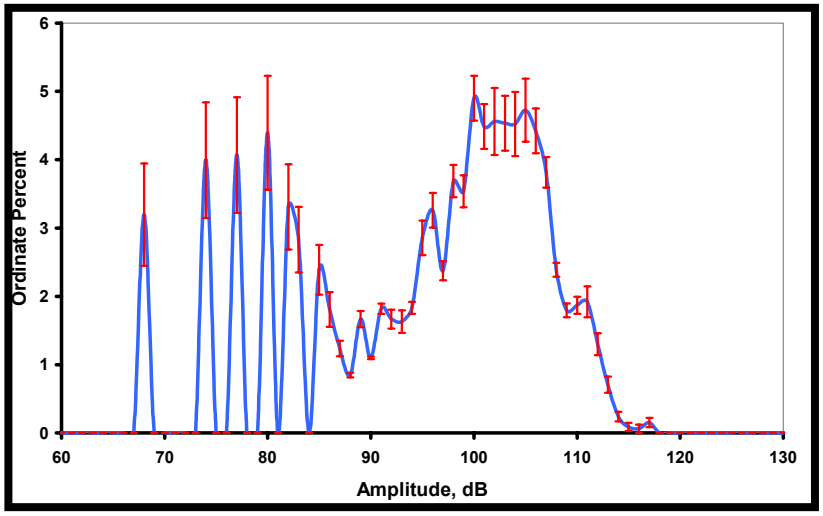

Figure 4.13: EFPI Amplitude Distribution, Top break position 1, reference $1x10^{-6}$ volts

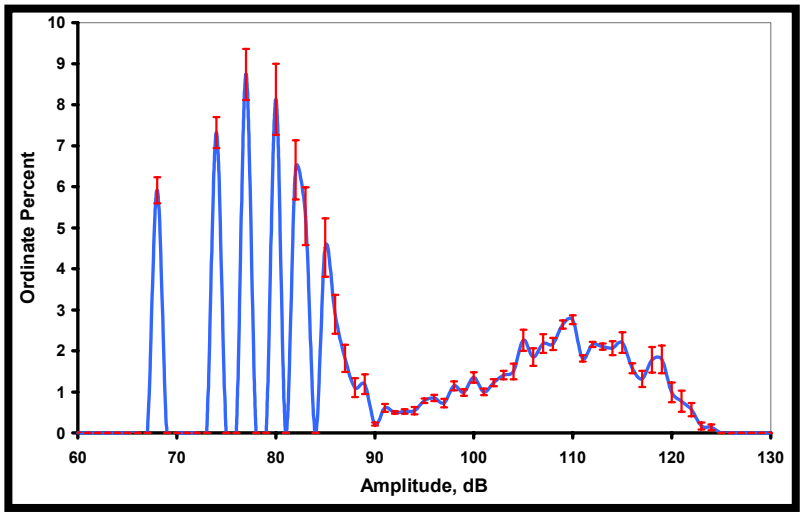

Figure 4.14: EFPI Amplitude Distribution, Groove break position 1, reference $1x10^{-6}$ volts

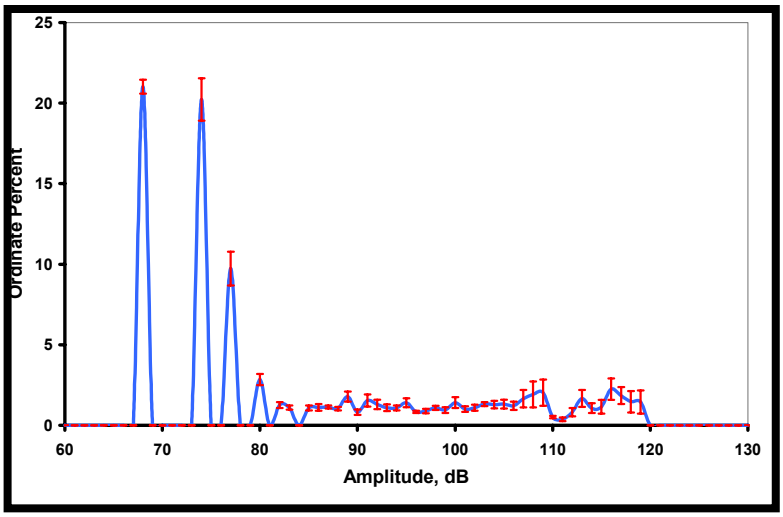

Figure 4.15: NIST Amplitude Distribution, Top break position 2, reference $1x10^{-6}$ volts

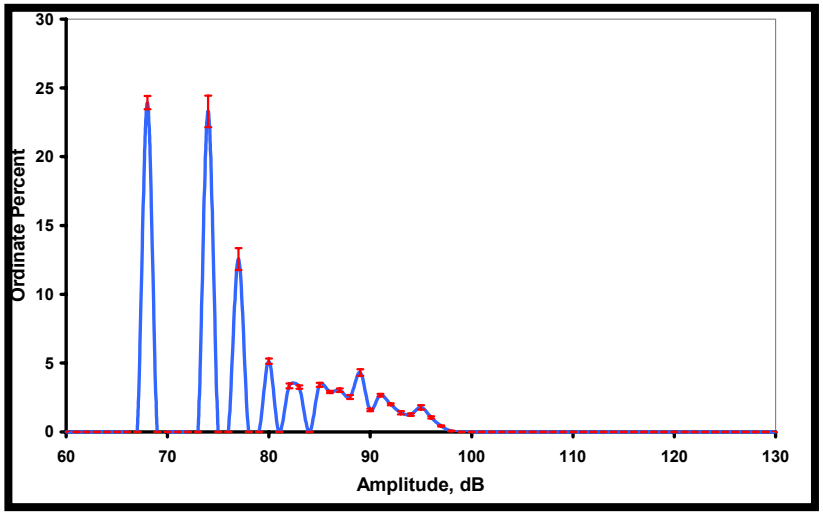

Figure 4.16: NIST Amplitude Distribution, Groove break position 2, reference $1x10^{-6}$ volts

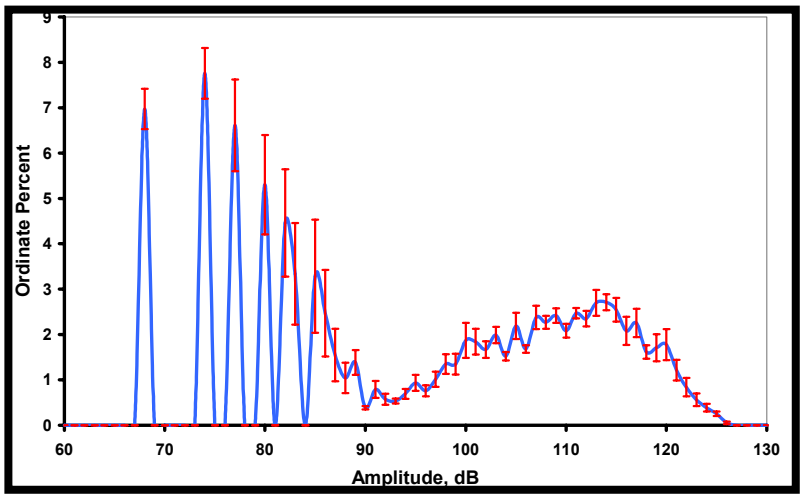

Figure 4.17: EFPI Amplitude Distribution, Top break position 2, reference $1x10^{-6}$ volts

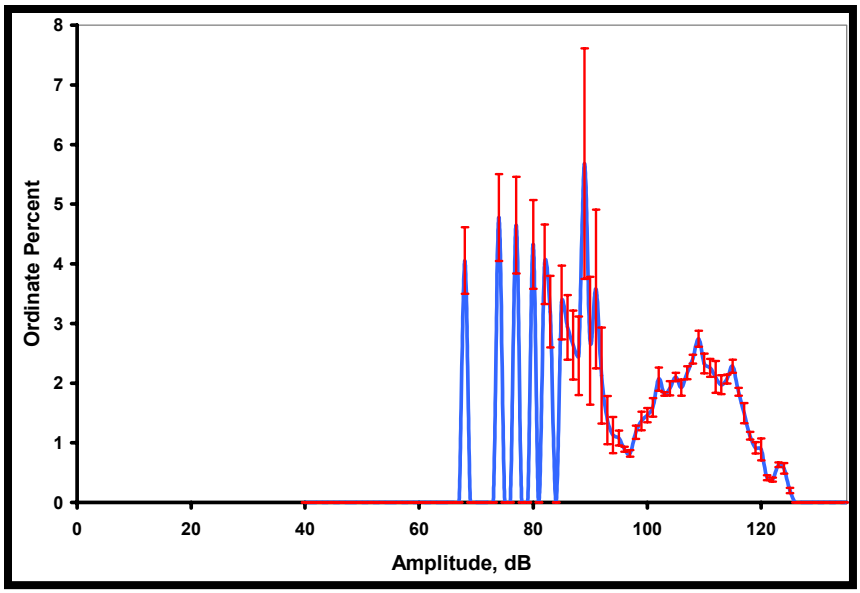

Figure 4.18: EFPI Amplitude Distribution, Groove break position 2, reference $1x10^{-6}$ volts

As expected from the previous results, the EFPI had a greater signal response to in-plane sources than the NIST. Also, for the in-plane on-axis case (position PLB-2) the NIST had large amplitude peaks below 80 dB and compared well with the EFPI amplitude distribution above 80 dB. Figures 4.19 and 4.20 show how the EFPI OFB compares to both the U and G(t)-Go amplitude distributions. Figures 4.21 and 4.22 compare the NIST and EFPI OFB amplitude distributions to the predicted and model generated displacements at position 2, mid-plane.

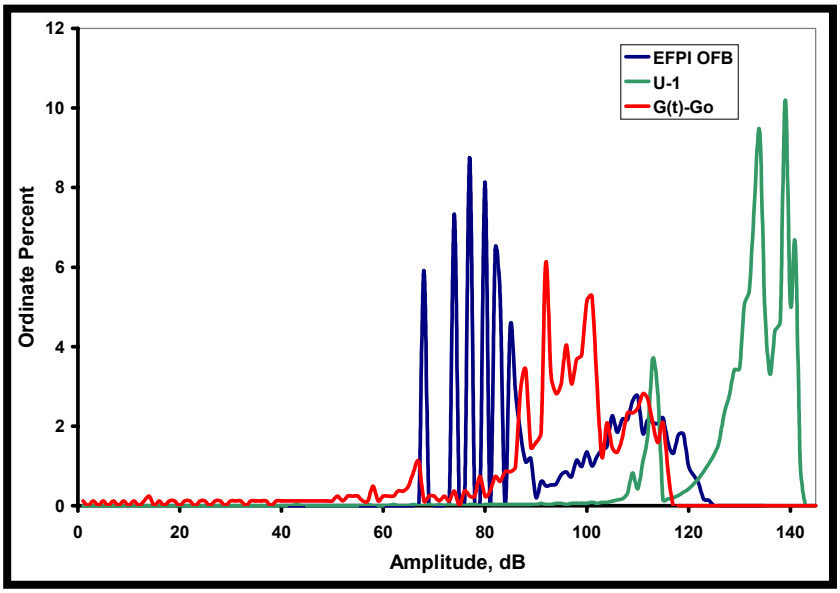

Figure 4.19: Comparison of Amplitude distributions from mid-plane sources (i.e. groove) at position 1, reference $1x10^{-6}$ volts.

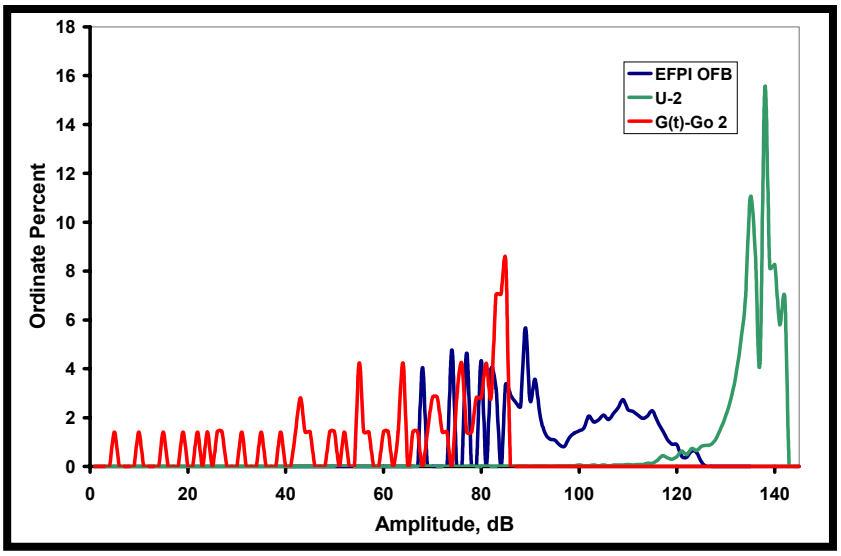

Figure 4.20: Comparison of Amplitude distributions from mid-plane sources (i.e. groove) at position 2, reference $1x10^{-6}$ volts.

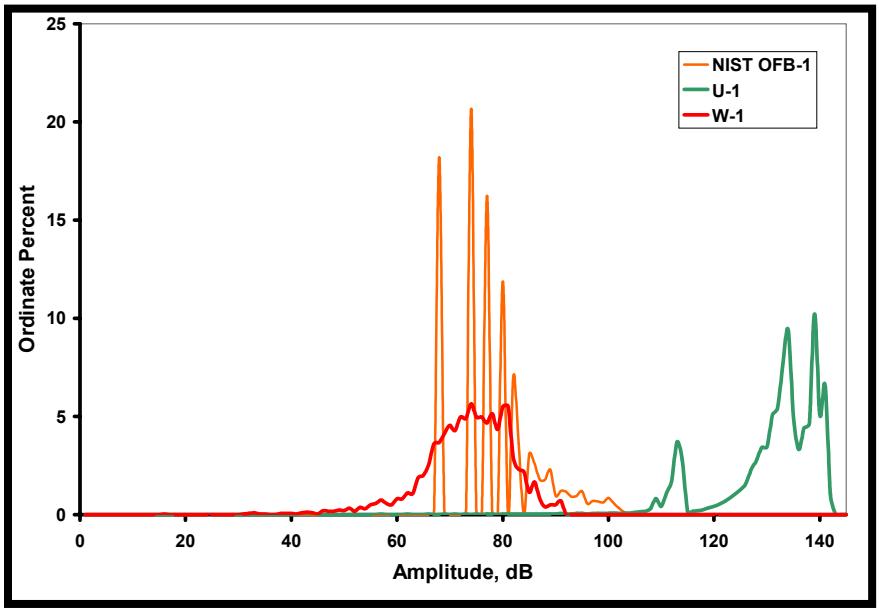

Figure 4.21: Comparison of Amplitude distributions from mid-plane sources (i.e. groove) at position 1, reference $1x10^{-6}$ volts.

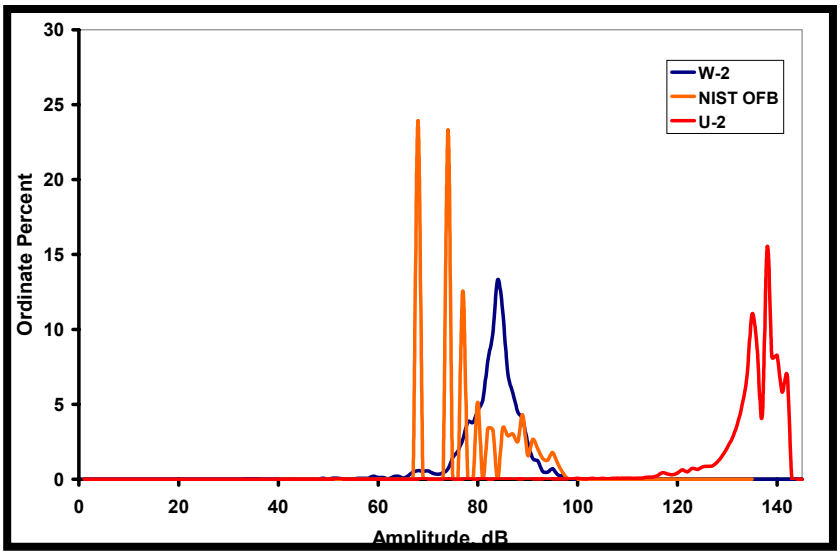

Figure 4.24: Comparison of Amplitude distributions from mid-plane sources (i.e. groove) at position 2, reference $1x10^{-6}$ volts.

Discussion of Optical Fiber Break Aluminum Plate Results

The optical fiber breaks provide a good in-plane signal source. However, they do not compare well with the majority of the predicted displacement components from the DFEM. Within certain amplitude ranges, the EFPI agrees with the G(t)-Go distribution. In general, the EFPI also has a higher decibel signal response more frequently than the NIST at amplitude values greater than 90 dB. The signal response of the EFPI is more accurate with respect to the off-axis or on-axis sources than the NIST. Furthermore, the amplitude distribution of the NIST becomes closer to the distribution of the W-displacement when the source is off-axis than when it is on-axis.

The NIST and the EFPI have amplitude peaks at similar locations below 80 dB. This coincidence may be from similar sources of noise, which both sensors can detect, see figures 3.08 and 3.10. However, these results suggest that the NIST and EFPI should respond in a similar manner to an OFB source. It can also be assumed that the NIST and EFPI should respond similarly to the fracture of fibers with similar properties. The largest percentage of error in the EFPI amplitude distributions was approximately 2%, with the average error in most of the amplitudes less than 0.25%. Using the NIST sensor, the error ranges were much greater, the largest error was 6.00% and the average error was 0.14%. It is reasonable to assume a 2% margin of error in the EFPI amplitude distributions in the rest of this work.

Chapter 5 – Optical Fiber MBrace^{tm} Experiment

The EFPI was mounted on coupons cut from Master Builder MBrace^{tm} CFRP sheets. The coupons were loaded in two different ways to generate different kinds of acoustic emission from different material deformations. The coupons were mounted on a plate and loaded using a constant rate of deflection on an Instron testing machine, with a load cell rated to a maximum of 20 kips or 9000 kg.

Ideal Fiber Fracture Comparison

In order to obtain an ideal test comparison for fiber fracture in large scale FRP composite samples, FRP coupons were fabricated with three plys of MBrace and telecommunication grade optical fibers (80 microns nominal diameter) embedded in the saturant layer between each ply and on the top surface. The wires were placed directly on the EFPI sensor axis and on parallel lines at 12.7 and 25.4 mm (0.5 and 1 in) distances from the EFPI fiber axis on either side. The coupons that were tested on the Instron had glass wires only in the 2nd layer off the fiber axis due to the machine grips and the difficulty of reproducibly breaking the glass wires in the grips, Figure 5.01. The coupon was placed in tension using the Instron and held with a constant 100 kg (220 lbs.) load. One half of each of the glass wires was covered in a silicone mold release to prevent the cured composite from gripping the entire glass wire. The load level was chosen to produce a low state of strain in the coupon material and not cause any significant damage due to the loading. While the load was applied to the test materials, the glass wires were pulled taut and cleaved to create a displacement similar to that of a fiber fracture. The wires were oriented in the same direction as the reinforcing fibers, parallel to the EFPI fiber axis with the silicone covered end protruding out of the coupon and the clean end of each glass wire was inside the coupon.

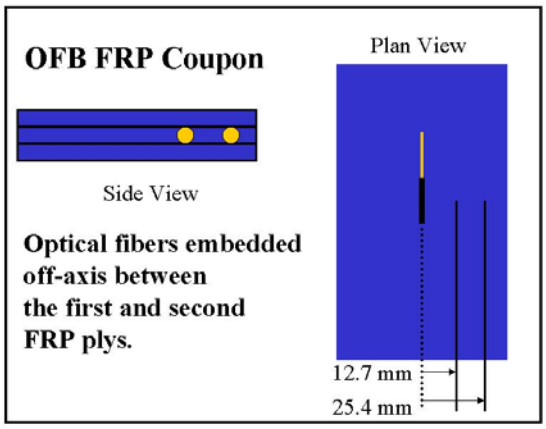

Figure 5.01: Illustration of embedded glass wires in FRP sample.

One coupon was attached to a stainless steel plate (grade 3404), Figure 5.02. In order to overcome the required conductive path between the NIST and the main signal amplifier, a thin sheet of tinfoil was laid over the surface of the test sample and held in place with 50 gram weights, Figure 5.03. Both the EFPI and the NIST sensors were used to record the data from the experiment with the steel/FRP plate experiment, while the EFPI and the PAC R15 sensors were used to record the signals from the Instron experiment, Figure 5.04.

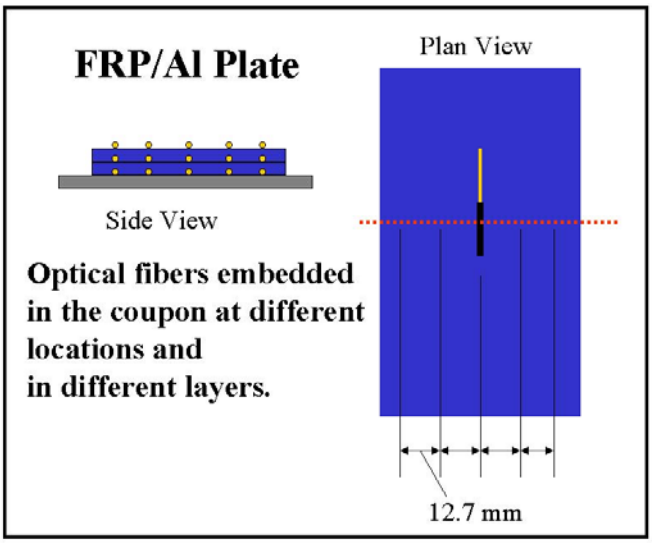

Figure 5.02: Schematic of FRP/Al test sample.

Figure 5.03: Schematic of coupon/ steel plate sample.

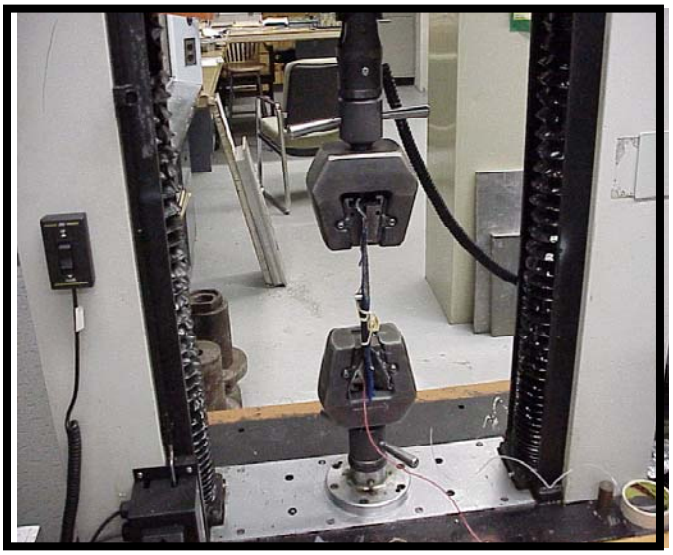

Figure 5.04: Picture of coupon in Instron Grips.

Fabrication of FRP coupons

The FRP material chosen for this study was MBrace[tm] carbon fiber unidirectional reinforcement system manufactured by Master Builder. All of the MBrace material used was cured and set-up according to the guidelines set by Master Builders and MBrace using official MBrace two part epoxy materials. All of the epoxy was used in small quantities (approx. 2-3 liters) using a 3:1 ratio, by volume, and mixed with a 50.8 mm wide paint stirrer at 300 to 600 rotations per minute.

The coupons were cut from sheets of the cured MBrace material. The MBrace sheets were applied to flat plywood boards covered with a thin (2 mil) layer of plastic sheeting on a level surface. A primer layer was applied directly to the plastic covered

wood. After a day of curing, the saturant layer and the MBrace carbon fiber fabric was applied to the board. If multiple layers of fabric were needed, multiple layers of saturant and fiber were applied successively. After curing, the FRP material was peeled from the plywood board and the thin plastic layer was removed from the back of the MBrace sheet.

Since a small volume of epoxy was used to make the FRP sheets, and there was no high capacity heat sink during the curing process (e.g., concrete), the epoxy required a longer cooling time than would be necessary in a typical field application. All of the coupons were given a 7-day cooling and curing period. As a side benefit, the slow cooling process reduced the probability of significant residual stresses forming in the material.

Several kinds of coupons were created for testing purposes. Test coupons were created with one or two plys of MBrace CF 530, Carbon Fiber Reinforcement System, which is specified as a high modulus carbon fiber material. Several coupons were also cut from the larger MBrace sheets so that the reinforcing fibers were oriented transverse to the direction of loading. Typical widths for the coupons were 63.5 mm (2.5 in) for a double ply sample and 88.9 mm (3.5 in) for a single ply sample and 88.9 mm (3.5 in) for a single ply transverse sample. The coupons were all within ±5 mm of 228.6 mm (9 in) in length. A single EFPI sensor was applied to each coupon, with a sensor gage length of 25 mm, as close to the exact center of the top surface as possible. See figure 5.05 for an example of a finished test coupon.

Figure 5.05: Typical Test Coupon, resting on a plywood board

The data from the sensors was received and recorded in the same manner in each FRP coupon experiment. The signals from the EFPI sensors were taken individually from

the Fiber Optic Strain Sensor (FOSS) detection system. These electrical signals were captured using analog to digital (A/D) sampling with a PC computer based A/D board, manufactured by Gage, with 12 bit voltage resolution using a 25 MHz sampling rate. See figure 5.06 for a symbolic diagram of the data recording and evaluating process.

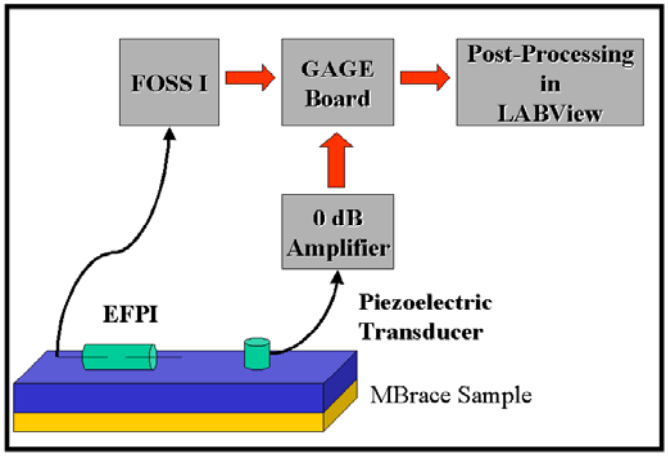

Figure 5.06: Data Flow Block Diagram

Results of Optical Fiber MBrace^{tm} Experiment

AE signals were recorded from two MBrace coupon samples with glass wires embedded in the matrix at various locations parallel to the direction of fiber reinforcement. Signals were also recorded from an aluminum/FRP plate that was selectively damaged and placed in 3 point bending. Each coupon was loaded in a different fashion, one was mounted to the surface of an unloaded steel plate, one mounted to the surface of a plate in three point bending and another in tension by an Instron testing machine held at a constant extension.

During loading, the glass wires were cleaved one at a time at 150 second intervals to prevent signal contamination from reflections or "ringing" in the samples. Two sensors were used to monitor the AE signals from each experiment. In both of the plate experiments the EFPI and NIST sensors were used to measure and record AE. In the constant strain experiment, a PAC R15 and the EFPI were used to monitor and record AE activity. Twenty distinct signals were recorded from the constant strain experiment that exceeded the threshold value of 1 mV. Ten distinct signals were recorded from the unloaded plate experiment that exceeded the threshold value of 1 mV. Figure 5.07 shows the amplitude distribution for the unloaded plate from the EFPI. Figure 5.08 is the

amplitude distribution from the NIST sensor for the unloaded plate experiment. Figure 5.09 is the amplitude distribution for the constant strain Instron experiment using the EFPI. Figure 5.10 is the amplitude distribution for the constant strain Instron experiment using the PAC R15. In each case, the reference voltage is $1x10^{-6}$ volts. Also, the distribution are labeled according to both the layer the OFB occurred on (surface, 2nd layer, 3rd layer) and the distance from the EFPI axis (0, 12.7 and 25.4 mm).

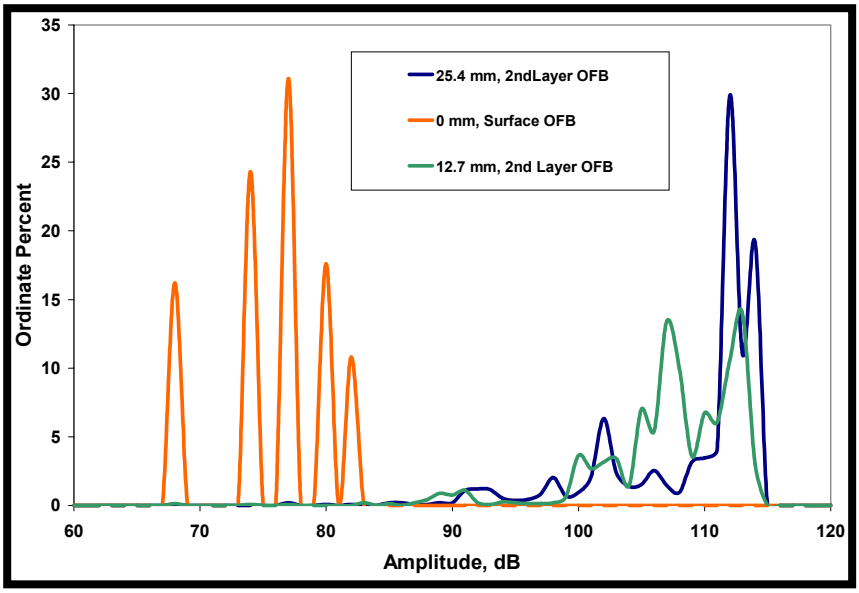

Figure 5.07: EFPI Amplitude Distributions, Unloaded Plate Glass Wire Break

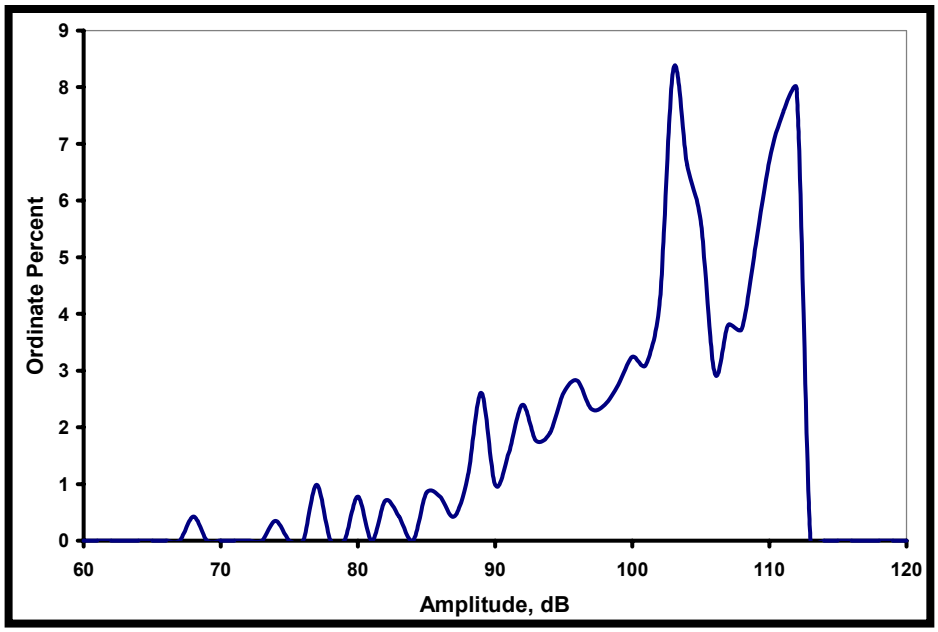

Figure 5.08: NIST Amplitude Distribution, Unloaded Plate Surface OFB, 0 mm.

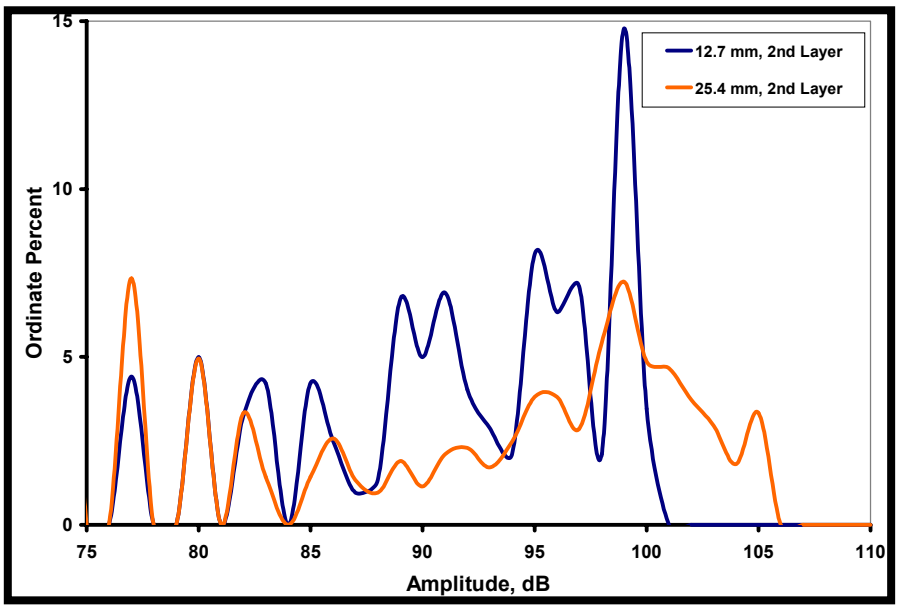

Figure 5.09: EFPI Amplitude Distribution for Instron OFB

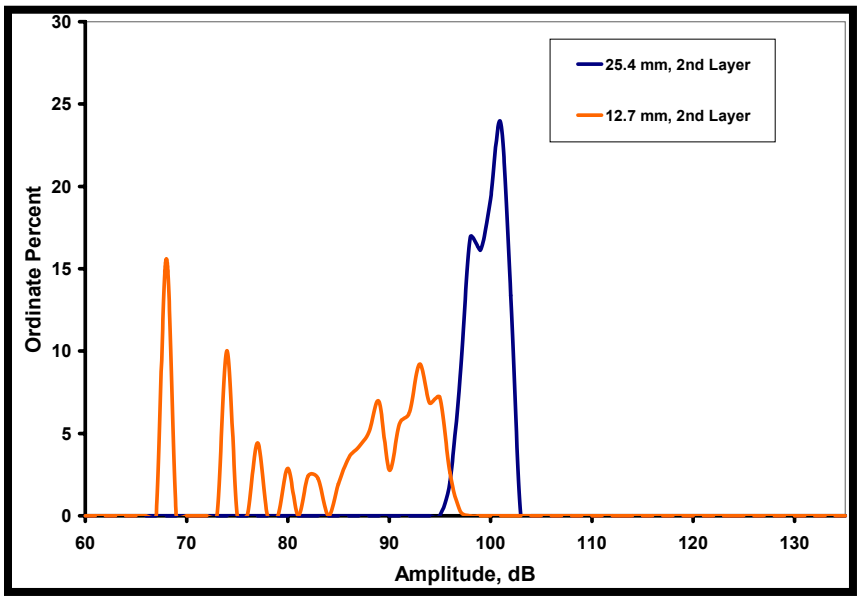

Figure 5.10: PAC R15 Amplitude Distribution for Instron OFB

Discussion of Optical Fiber MBrace^{tm} Results

The purpose of these three experiments was to create an artificial situation where the only damage experienced by the MBrace materials was due to the cleaving of the glass wires or the fracture of a few select carbon reinforcing fibers. Aside from matrix micro-cracks due to the tensile loading, the only source of displacement is the in-plane disturbance caused by the sudden unloading of the glass wires. The glass wires had an 80

micron nominal diameter which is on the order of 8-10 carbon fibers. Therefore the sudden cleaving of a glass wire is approximately equivalent to a small bundle of fibers fracturing simultaneously.

Although it was not possible to record signals from the glass wires in the 3rd layer of either the Instron coupon or the FRP/Steel plate, the tests provided a valuable comparison between the different sensors and the sensor response to an ideally fiber fracture like displacement. The most likely cause for the difficulty of obtaining signals from the 3rd layer glass wires is the weak attachment of the wires to the matrix/plate interface due to the mold release. However, in the case of the unloaded FRP/Steel plate experiment, the NIST sensor was only capable of detecting displacements from a surface break whereas the EFPI was capable of detecting displacements in a lower layer and off the optimally sensitive axis of the sensor.

In the unloaded plate experiment, the surface breaks detected by the EFPI resulted in three peaks at 77, 80 and 82 dB. For the eccentric breaks at 12.7 and 25.4 mm, the significant peaks were at amplitude values of 100, 107, 113 and 98, 102, 112 and 114 decibels respectively. The NIST sensor detected amplitudes most often at values of 89, 92, 100, 103 and 112 dB. While many of these values are in the neighborhood of the EFPI results for off-axis glass wire breaks, they do not agree for the on axis case where the EFPI is expected to be the most sensitive. Two possible interpretations of this result are that the EFPI is most sensitive to surface breaks or that the glass wire break does not produce any significant out of plane displacement. It is interesting to note that both the EFPI and the NIST consistently had amplitudes values that were close to the published fiber fracture amplitude values from Bohse and Valentin [12, 26, 50].

In the increasing deflection experiment, the EFPI detected amplitude values most often at 96, 97 and 99 dB for the 25.4 mm off axis breaks and at 96, 99 and 105 dB for the 12.7 mm off axis breaks. The PAC R15 sensor detected amplitudes most often at 89, 93 and 95 dB for the 12.7 mm off axis breaks and at 98 and 101 dB for the 25.4 mm off-axis breaks. These results also agree with the range of values from the signals generated by the previous buried off-axis glass wire breaks.

Chapter 6 – Mechanical Loading of MBrace^{tm} Coupons

Sustained Load MBrace^{tm} AE Experiments

The coupons were held in tension by a weighted lever arm to generate AE during different states of strain. Ideally, the coupons are held at a constant level of stress throughout the test. This type of loading is similar to what the material would experience in a field application and will allow the FRP coupons to rapidly respond to strain or displacement in the direction of loading. In a field application, the loads due to matrix or fiber failure are rapidly redistributed throughout the entire section of FRP. This is significantly different from testing a sample on the Instron, in which the rate of deflection is predetermined by the machine controls and the ability of the material to react to displacements is affected by the speed of the machine. The load level was based on the system specifications for a long-term (>5 years) reinforcement/rehabilitation application of the material [67]. Figure 6.01 is a schematic of a typical coupon used for the sustained load test.

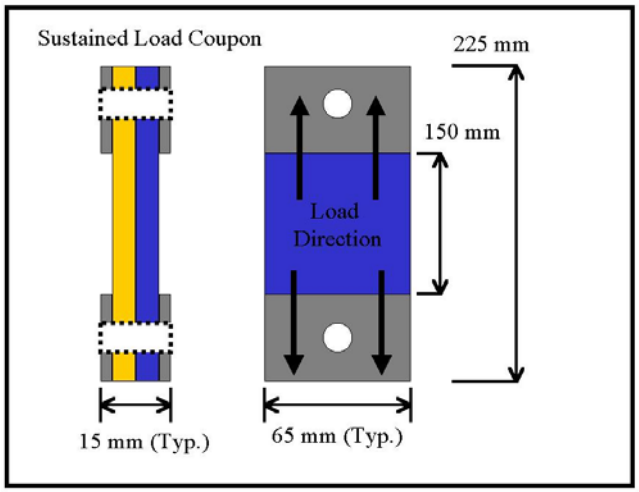

Figure 6.01: Schematic of sustained load coupon in test configuration.

The coupons were loaded in tension using a lever arm with a mechanical advantage of 20:1 with a weight of 75 kg (166 lbs.) on the balance arm. See figure 6.02 for a picture of the machine.

Figure 6.02: Constant Load Lever Arm

The design guidelines for MBrace state that the FRP reinforcing system should be optimized for one of two different conditions, short term or long term. The recommended allowable design strength for long-term applications is obtained using 1/3 of the value of the ultimate tensile stress per unit width of sheet (500 mm), or approximately 1.2 x 10^6 kg/cm^2. All coupons were loaded to 80% of the allowable design stress for a long term application, or 26% of the ultimate tensile strength (80% of 33%) [67]. The grips used to hold the coupons during the test were attached to bearings so that the coupon would sustain no net torque. The area of the FRP coupons placed in the grips were supported by thin strips of plywood and plastic to prevent localized damage and any transmission of AE from the grips to the sensor, Figure 6.01.

Constant Rate of Deflection Instron MBrace^{tm} AE Experiments

Quasi-static loading of selectively damaged FRP coupons was used to generate AE signals from possible fiber fractures and other failure modes. Several kinds of loading conditions were used to capture AE during damage development in the MBrace^{tm} samples. FRP coupons were tested on an Instron testing machine and loaded in tension parallel to the axis of fiber reinforcement until catastrophic failure at a maximum applied stress of 600 MPa. The Instron used in these experiments was rated to 9000 kg and the coupons were loaded at a rate of 0.762 mm/minute (0.03 in/min). Cloth backed 120 Grit sandpaper was used between the coupon and the serrated grips to secure the samples and prevent slipping. Both the EFPI and a PAC R15 transducer were used to monitor samples

during testing using the Instron. FRP sheets were also mounted on an aluminum plate. The plate was then loaded in three-point bending until it yielded. The three-point plate bending experiment was used to place a maximum tensile stress on the fibers in the FRP sheet at the center of the plate, Figure 6.03. The aluminum plate was 101.6 mm by 266.7 mm and 6 mm thick. The matrix surrounding the fibers on a small section in the center of the plate was removed using solvents and an Exacto^{tm} knife and then the reinforcing fibers were slightly scored with a sharp blade so that they were not completely severed across the scored region, Figure 6.04.

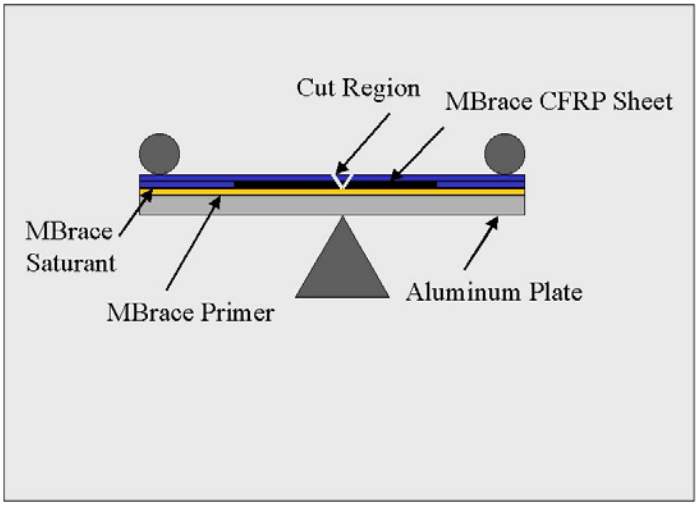

Figure 6.03: Three Point Bending Test Configuration.

Figure 6.04: Aluminum Plate for Three Point Bending Experiment, pen points to scored region.

The combination of tensile stress and selective damaging of the FRP material created a high probability that the first fibers to fracture would be in the damaged area in the center of the plate. The goal of the experiment was to force fiber failure prematurely and record the character of the signal. Both the EFPI and the NIST sensors were used to monitor the resulting AE. As a side note to aid further experimental investigation, care must be taken to insure that the FRP material is bonded solely at the edges of the plate. If

the entire bottom layer of the coupon is attached to the top surface of the plate delamination may make it difficult to obtain accurate test results. In other words, the AE from the failure that occurs may not be from fiber fracture but FRP delaminating from the surface of the plate. Silicon mold release was sprayed onto a masked off area in the center of each plate in order to prevent the FRP from delaminating.

Results of Mechanical Loading of MBrace^{tm} Coupons Experiment

Constant Rate of Deflection Instron Experiments.

AE signals were recorded from several MBrace coupons under increasing tensile strain. The EFPI and a Physical Acoustics R15 sensor were used to monitor the double ply coupons during the tests. The R15 could not be used to monitor the single ply tests since the methods used to attach the sensor to the coupon caused the coupons to crack and split. The strain was applied using an Instron testing machine in two different ways. First, the coupons were loaded in tension at a rate of 0.762 mm/min (0.03 in/min), until failure occurred at approximately 0.1% strain. Second, the coupons were loaded in tension at a rate of 0.508 mm/min (0.02 in/min), until the Instron applied 0.05% strain to the coupon. Two single ply and two double ply coupons were loaded using the first condition and two double ply coupons were loaded using the second condition. The coupons had a width of 63.5 mm (2.5 in) and was 228.6 mm (9 in) long, Figure 6.01. Seventy distinct signals that exceeded the threshold value of 10 mV were recorded during the experiment using the first loading conditions. 650 distinct signals that exceeded the threshold of 1 mV were recorded during the experiment using the second loading conditions. Ten distinct signals were also recorded from the tensile strain three point bending experiment. The threshold was lowered on these tests to attempt to capture more signals in the lower amplitude range.

Figure 6.05 shows the EFPI amplitude distributions for the single ply coupons using the first loading condition. Figure 6.06 shows the EFPI amplitude distribution for the double ply coupons using the first loading condition. Figure 6.07 shows the EFPI amplitude distribution for the double ply coupons using the second loading condition. Figures 6.08 and 6.09 show the PAC R15 amplitude distributions for the double ply coupons under increasing deflection using the first and second loading conditions. The

cumulative energy measured under the rectified signal envelope in the double ply coupon test under increasing strain using the first condition is shown in figure 6.10. Figure 6.11 displays the three point bending unfiltered amplitude distribution from the NIST and EFPI sensors. The reference voltage in all cases is $1x10^{-6}$ volts.

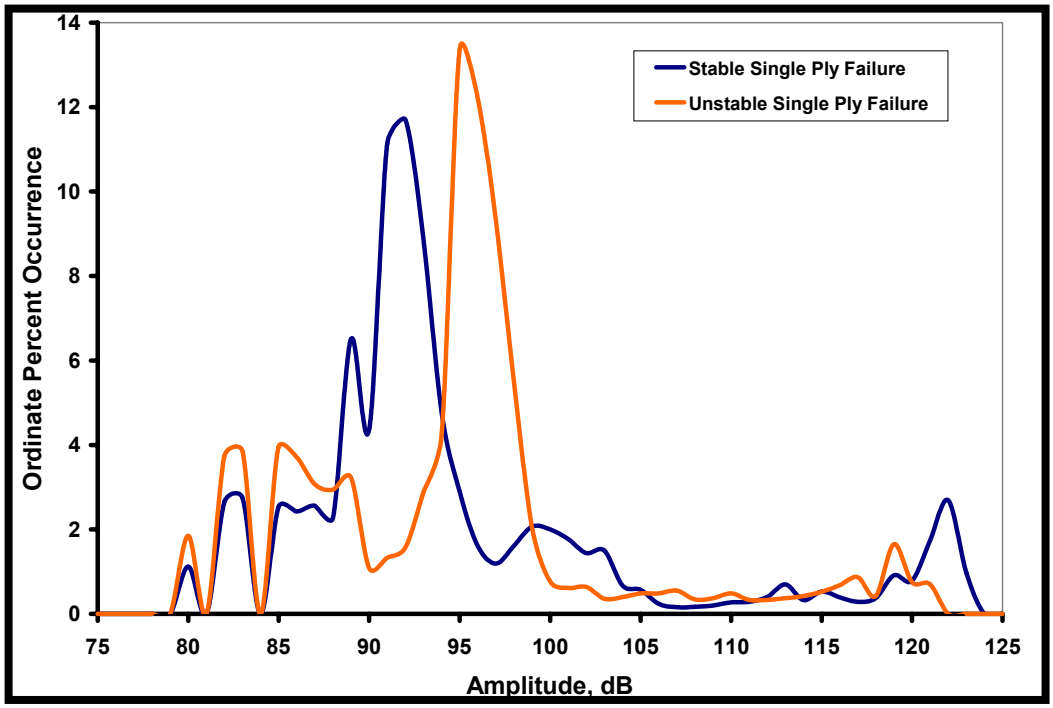

Figure 6.05: Single Ply EFPI Amplitude Distribution, First Loading Condition

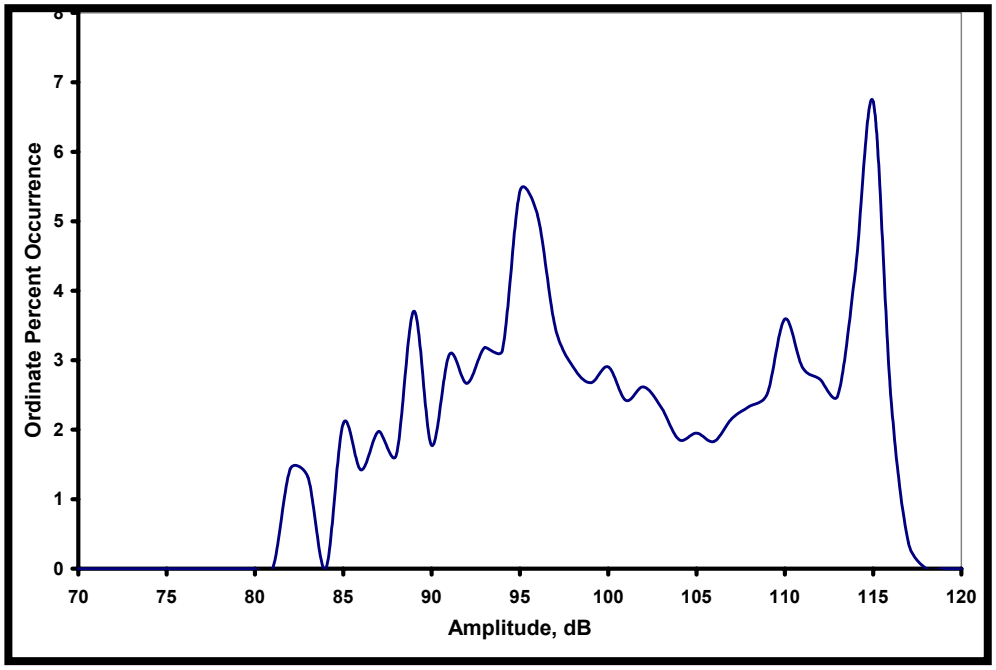

Figure 6.06: Double Ply EFPI Amplitude Distribution, First Loading Condition

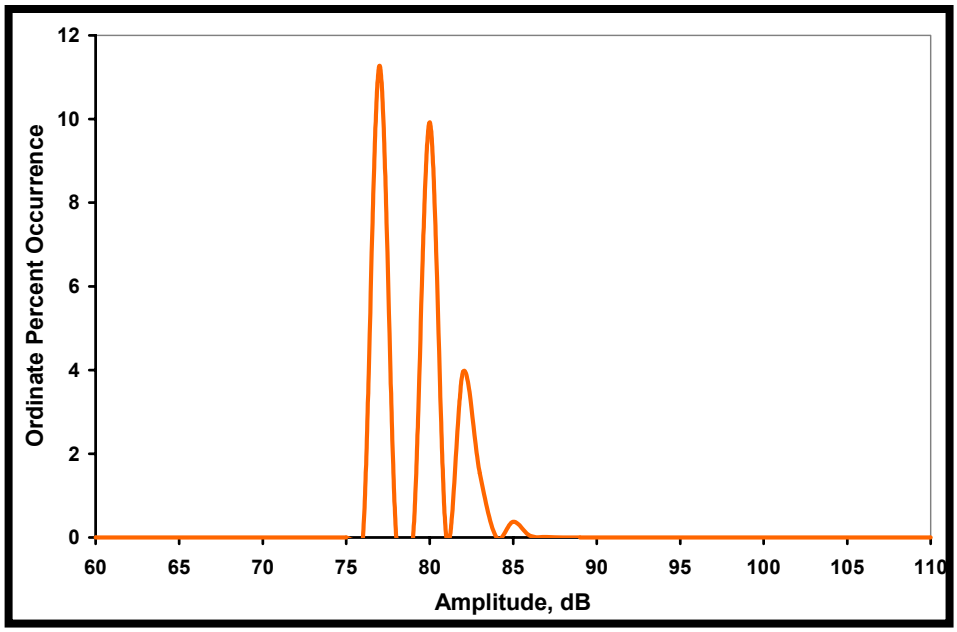

Figure 6.07: Double Ply EFPI Amplitude Distribution, Second Loading Condition

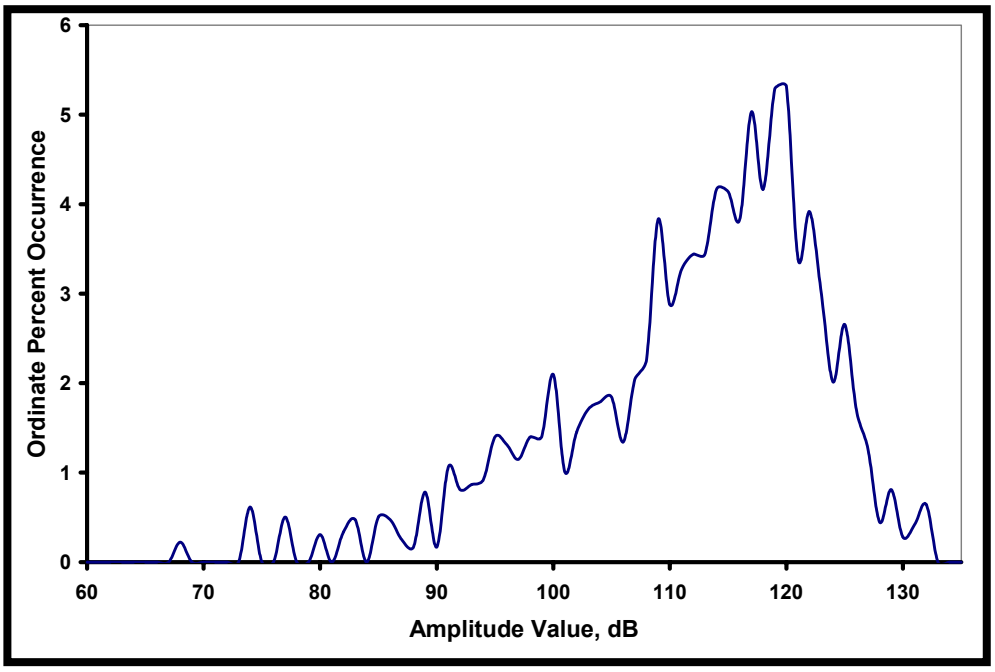

Figure 6.08: Double Ply PAC R15 Amplitude Distribution, First Loading Condition

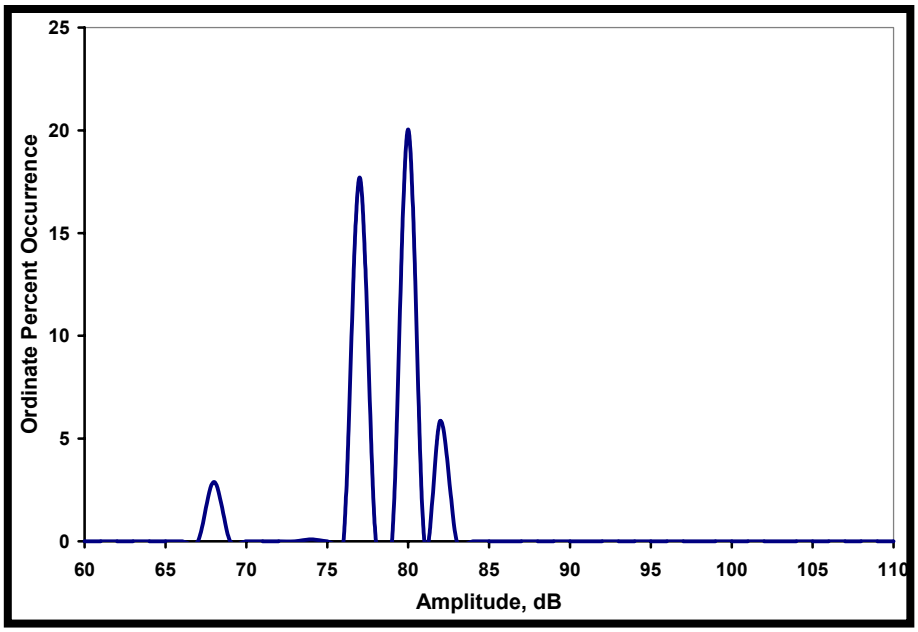

Figure 6.09: Double Ply PAC R15 Amplitude Distribution, Second Loading Condition.

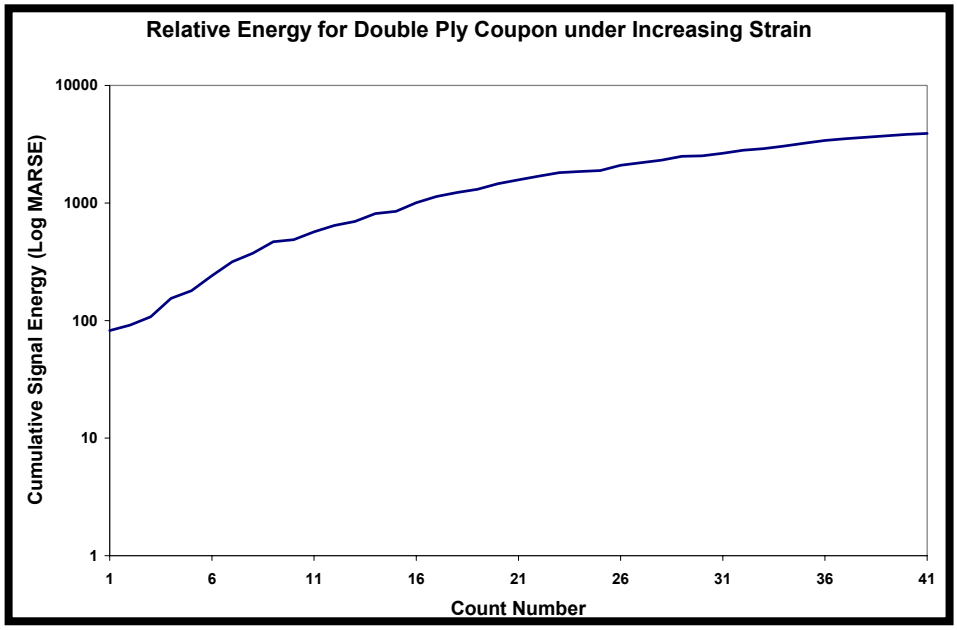

Figure 6.10: Log of MARSE vs. EFPI AE signal counts for a double ply coupon under the first loading condition.

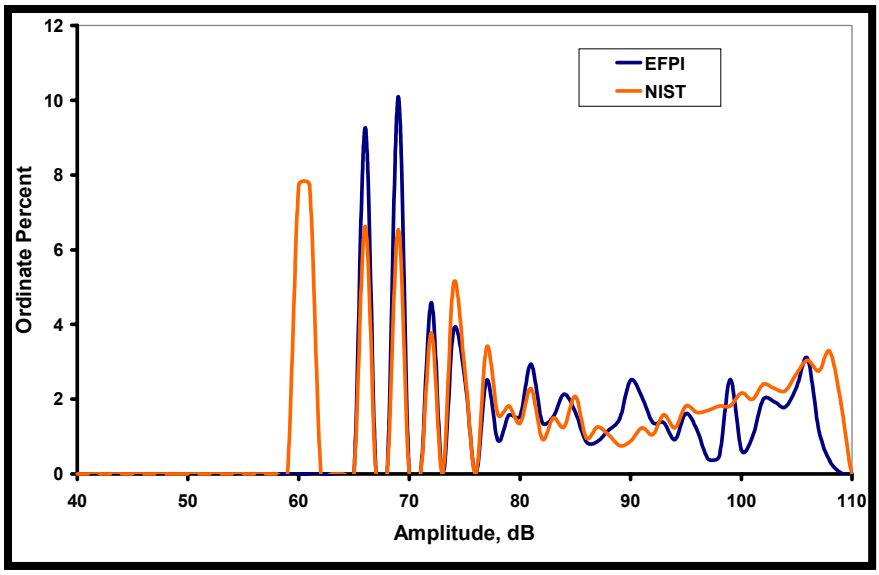

Figure 6.11: NIST and EFPI three point bending amplitude distribution.

Sustained Load Experiment

AE signals were recorded from 12 different undamaged MBrace coupons under a constant, sustained load. Four single ply unidirectional coupons were loaded parallel to the axis of reinforcement. Four double ply unidirectional coupons were also loaded parallel to the axis of reinforcement. Four more single ply coupons were loaded transverse to the axis of reinforcement. AE signals were recorded using the EFPI sensor and recorded using a Gage digital acquisition board, at a sample rate of 25 MHz, with zero gain. Figure 6.12 shows the amplitude distribution for the single ply coupon unfiltered results. Figure 6.13 shows the averaged frequency spectrum of the unfiltered signals, based on a set of 20 recorded signals, for the single ply coupon tests. The signals were processed using a Bessel IIR high pass filter, with a cut-off frequency of 45 kHz, implemented by LabView.

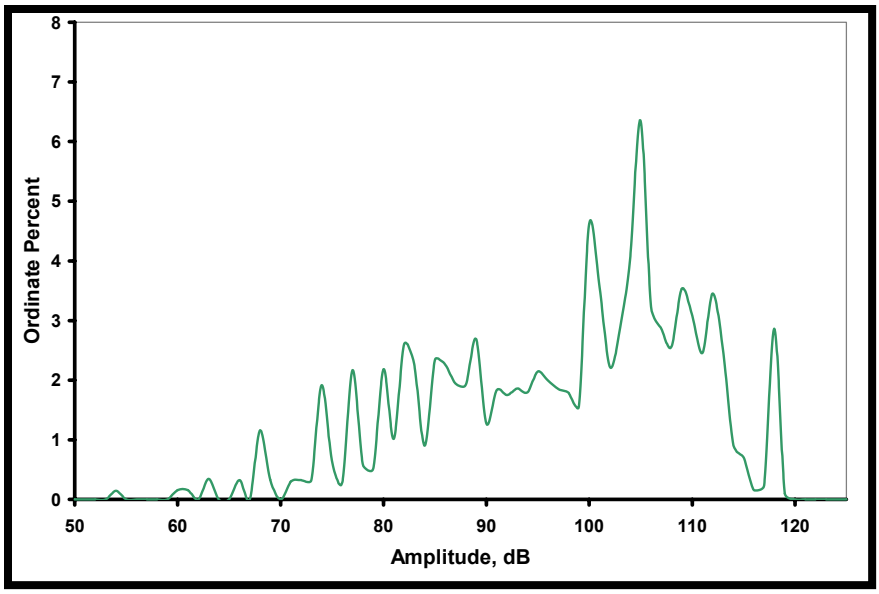

Figure 6.12: Unfiltered Single Ply Amplitude Distribution

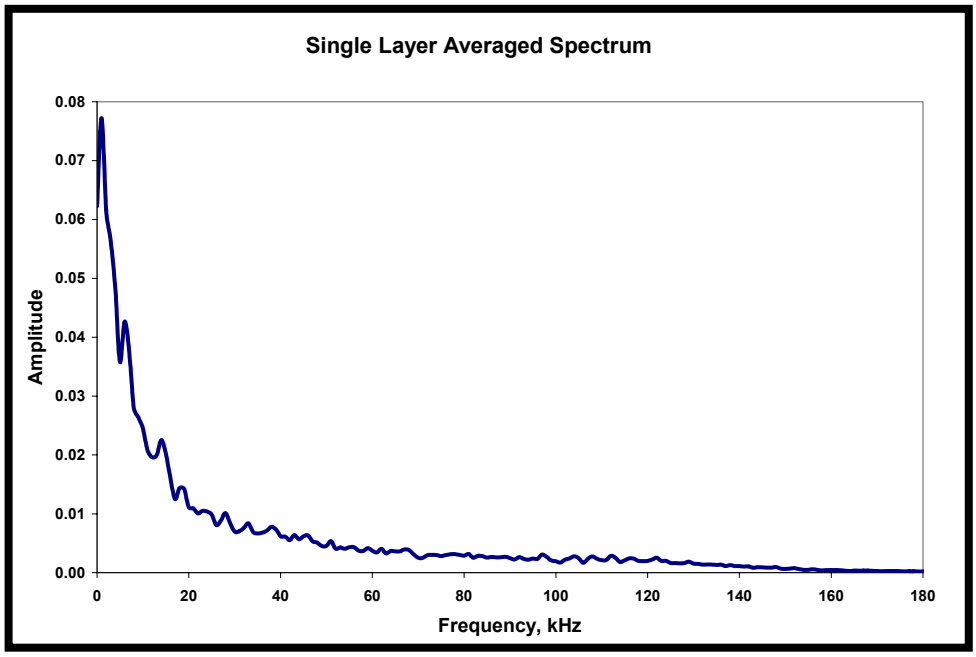

Figure 6.13: Unfiltered Single Ply Averaged Frequency Spectrum

The single ply coupons were 88.9 mm (3.5 in) wide and loaded so as to produce a 143 MPa (20.7 ksi) tensile stress. The loading produced localized damage (i.e. tear out) in some of the coupons, around the machine fixtures. See figure 6.14 for an example of the tearing around the grip area. 20 distinct signals were recorded that exceeded the trigger threshold of 10 mV.

Figure 6.14: Single Ply Tearing

Figure 6.15 shows the amplitude distribution for the double ply coupon unfiltered results. Figure 6.16 shows the averaged frequency spectrum of the unfiltered signals, based on a set of 20 recorded signals, for the double ply coupon tests. Figure 6.17 compares the unfiltered single ply coupon data with the double ply data.

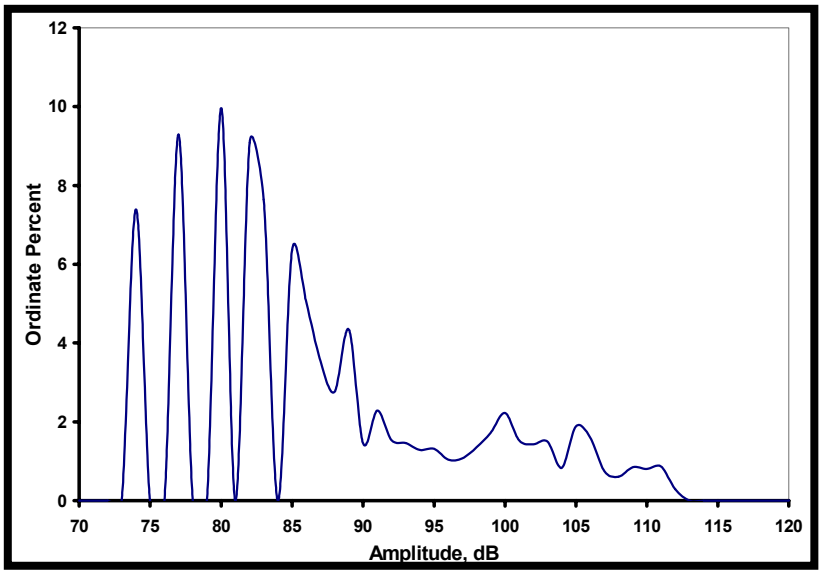

Figure 6.15: Double Ply Unfiltered Amplitude Distribution

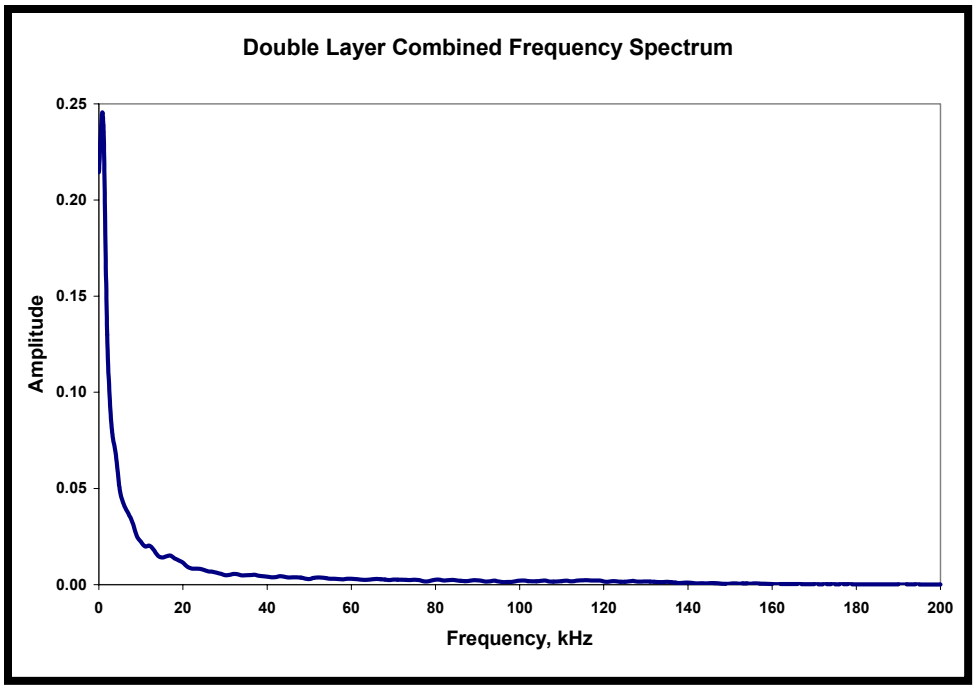

Figure 6.16: Double Ply Average Frequency Spectrum

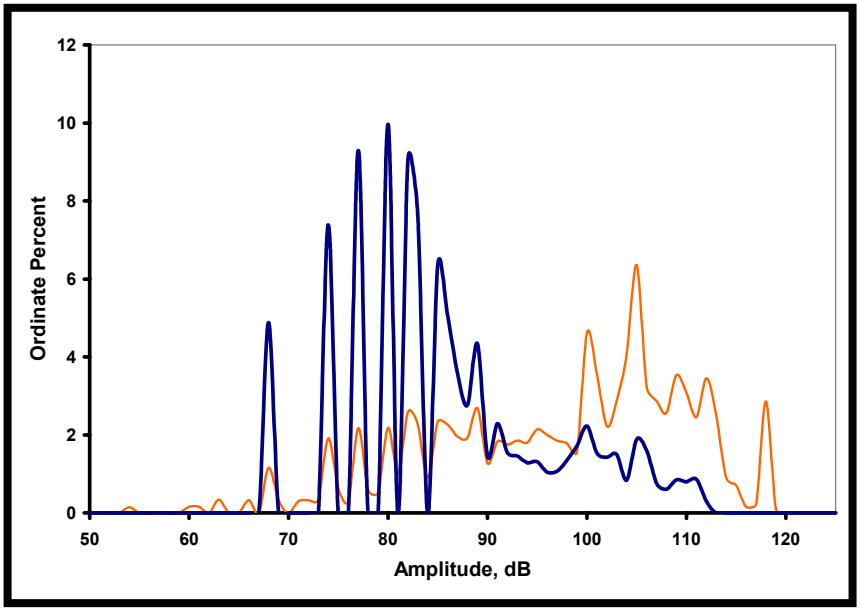

Figure 6.17: Comparison of Single and Double Ply Unfiltered Amplitude Distributions

The double ply coupons were 74.0 mm (2.5 in) wide and loaded to produce a 199 MPa (28.9 ksi) tensile stress. Twenty distinct signals were recorded that exceeded the trigger threshold of 10 mV. No localized damage in the coupon was observed in the area of the machine grips either during or after the testing. However, the loading produced a "cupping" effect on the coupon causing the material to bow out in the middle and remain straight at the edges and along the sides. This cupping caused longitudinal cracking, or

axial splitting, to grow in a stable fashion parallel to the reinforcing fibers and running through the polymer later and the CFRP/Epoxy matrix. See figure 6.18 for typical picture of a longitudinal crack.

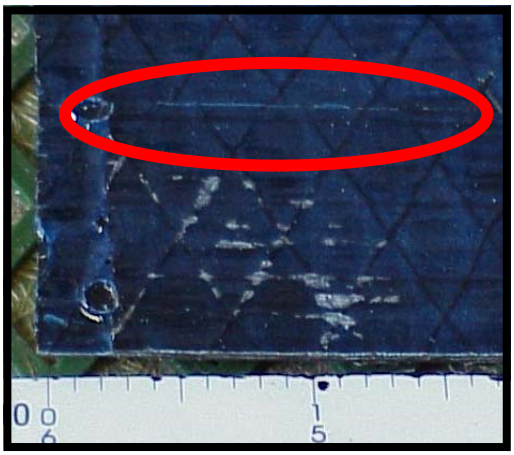

Figure 6.18: Example of Longitudinal Cracking

Figure 6.19 shows the unfiltered and filtered amplitude distributions from the transversely loaded coupon test. Figure 6.20 is the averaged frequency spectrum from the transverse tests. Due to the relatively large and rapidly applied load, all transversely loaded coupons were torn approximately in half and failed completely during each test. 4 distinct signals were recorded that exceeded the trigger threshold value of 10 mV before each coupon failed completely. Figure 6.21 compares the unfiltered amplitude distributions from the single, double and transversely loaded tests. It should be noted that due to the differential nature of the EFPI, the rapidly applied and constant state of strain experienced by the transversely loaded coupons resulted in signals that had a positive slope. As a result, no negative amplitude values were observed during the transverse tests. See figure 6.22 for an example of a typical transverse signal compared with a filtered signal. Also, none of the reinforcing fibers were directly loaded during the test. There was also no evidence of the reinforcing fibers bridging the ruptured coupons. See Figure 6.23 for a picture of a typical transverse failed coupon. Figures 6.24 and 6.25 are typical examples of AE signals observed by the EFPI from single and double ply coupons during the sustained load tests.

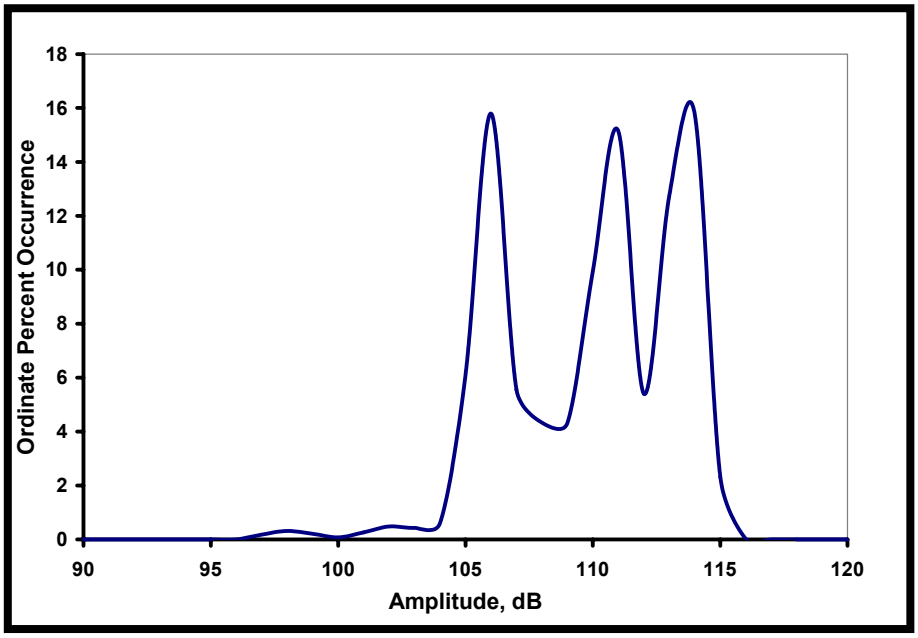

Figure 6.19: Transverse Loaded Amplitude Comparison

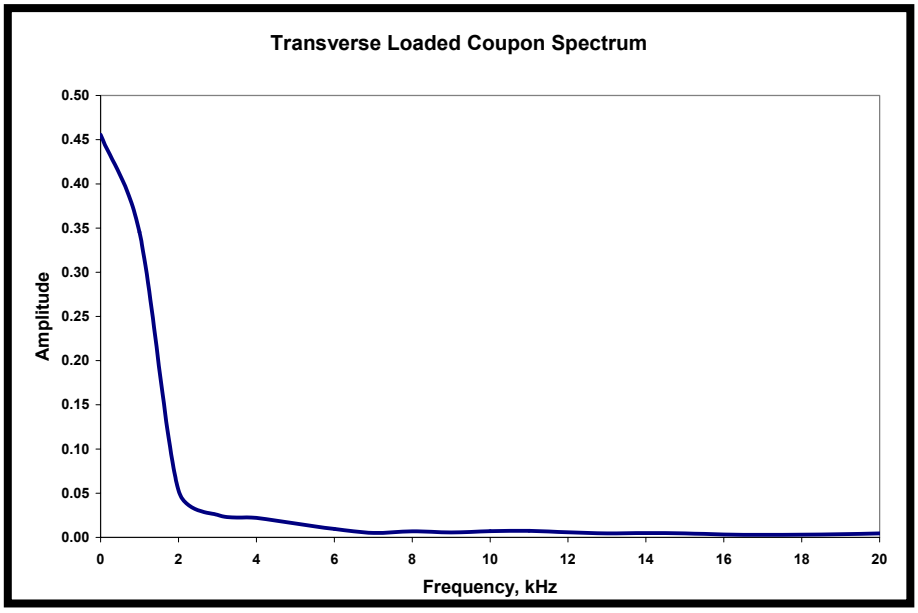

Figure 6.20: Averaged Spectrum of Transversely Loaded Coupons

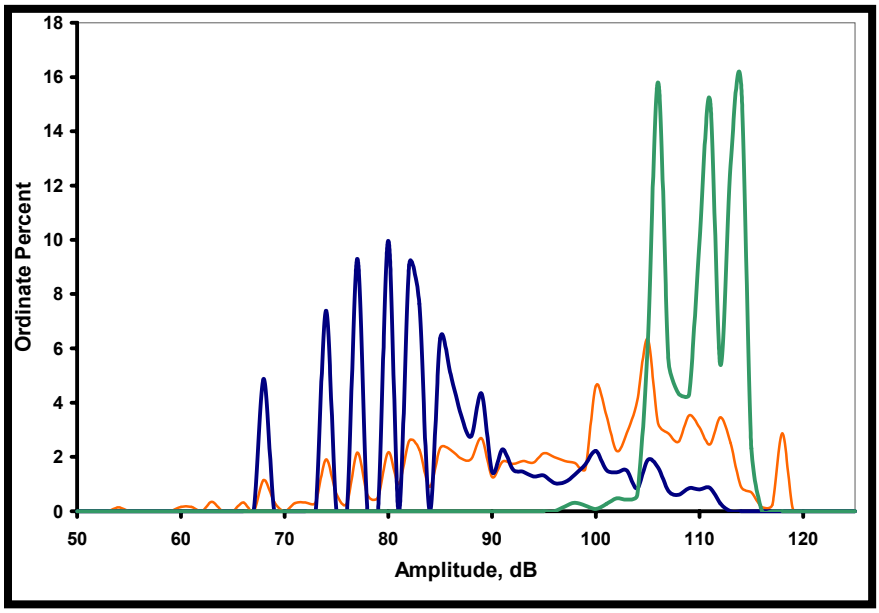

Figure 6.21: Comparison of EFPI Sustained Load Amplitude Distributions.

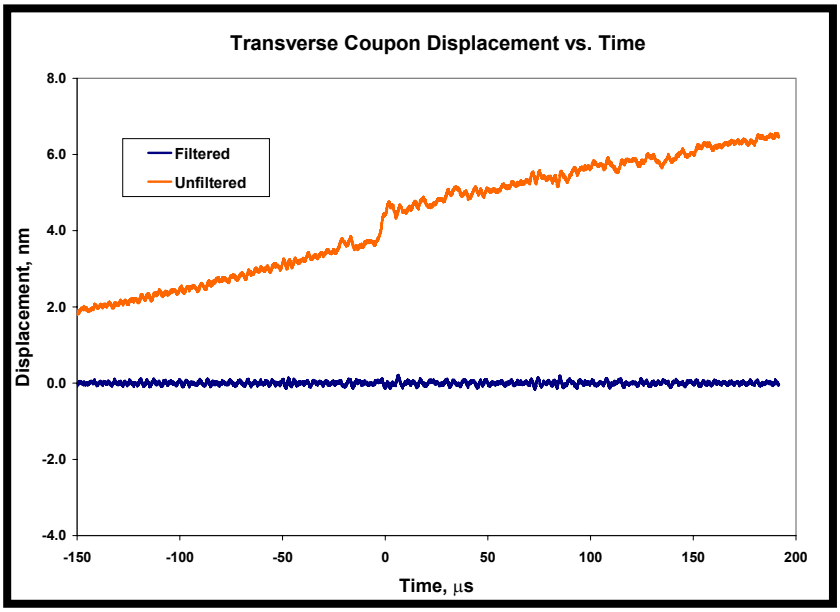

Figure 6.22: Typical Filtered and Unfiltered Transverse Coupon EFPI AE Signals

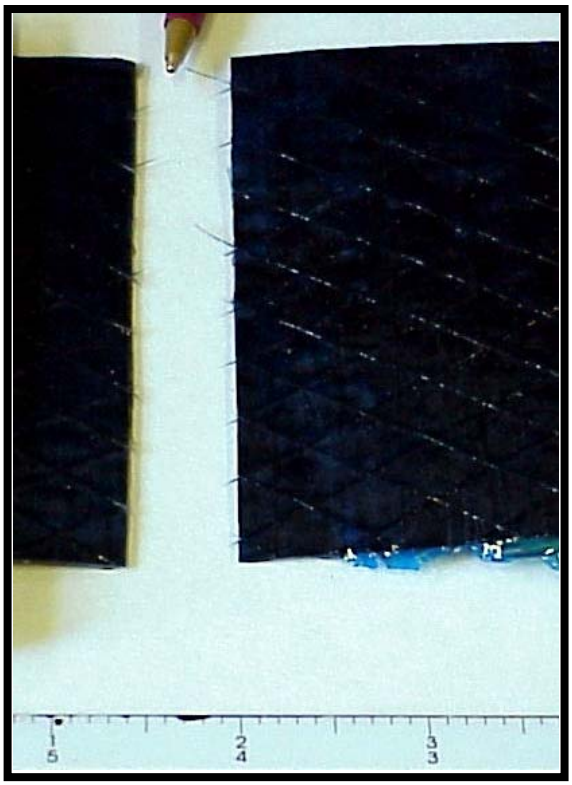

Figure 6.23: Typical Transverse Coupon Tear

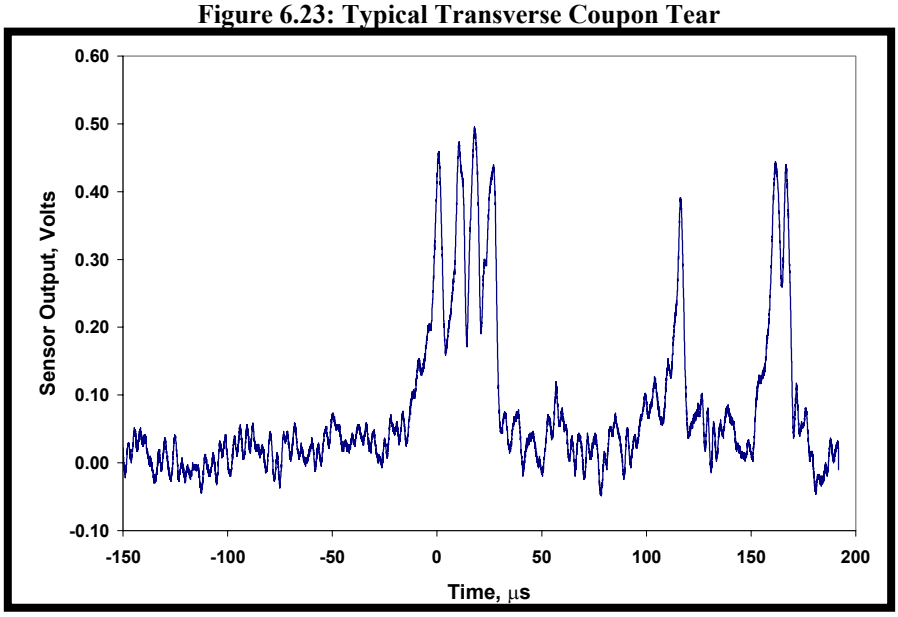

Figure 6.24: Typical Filtered and Unfiltered Single Ply Coupon EFPI AE Signals

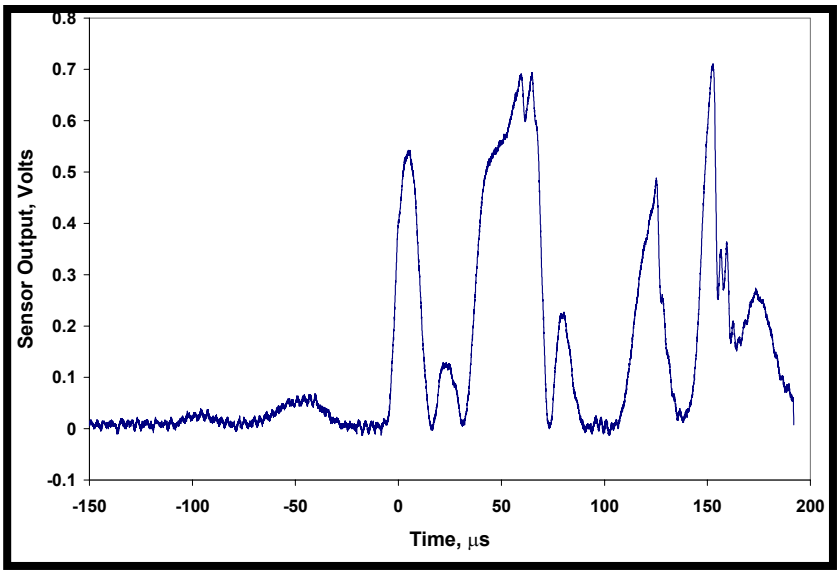

Figure 6.25: Typical Unfiltered Double Ply Coupon EFPI AE Signals

Discussion of Mechanical Loading Results

Constant Rate of Deflection Coupon Experiments

The increasing deflection of the coupons produced different results than the sustained load tests. However, similarities become apparent when the results from the two experiments are compared. It can be seen that several peaks from the PAC R15 occur in the same region and with a similar percent occurrence as the EFPI sensor. This result agree with the previous results indicating that the G(t)-Go and W displacements agree closely in some situations. This may indicate that the damage mechanisms occurring at these amplitudes have in-plane and out-of-plane components.

There were also similar peaks in the amplitude distributions of the PAC R15 and EFPI sensors at amplitude values of 82 and 109 dB for the first loading condition. For the second loading condition, it is very interesting that the PAC R15 and the EFPI observed amplitude values of 77, 80 and 82 dB with similar frequency. The PAC R15 also had a peak at 68 dB that agrees with earlier comparisons of signal amplitude values for fiber fractures. The energy associated with the signals that PAC R15 sensor detected was less than the energy associated with the EFPI signals in the first loading condition, Table 6.1. On average the signals detected by the EFPI have more rectified area, even though the R15 sensor typically had higher signal amplitudes under the same test configurations. This suggests that the EFPI is capable of detecting signal characteristics that cannot be

detected by out-of-plane sensors even if there is an out-of-plane component associated with the deformation that originated the AE signal. However, figure 6.05 shows that fiber fractures have an out-of-plane and in-plane displacement component.

Table 6.1: Average MARSE comparison from double ply coupon tests. CL is Constant Load, IL is Instron test or Increasing Load

Double Ply Mbrace Coupon			
	CL-EFPI	IL-EFPI	IL-PACR15
Avg. MARSE	70.04	95.03	50.33

In the case of a fiber fracture, it is logical to assume that the sudden release of mechanical energy would travel in along the axis of the fiber and the recoil of the fibers would generate a flexural plate mode in the coupon. Therefore, it is reasonable that an out-of-plane component of displacement would accompany a fiber fracture. However, given the previously defined amplitudes for fiber fracture (69 dB), it seems likely that an in-plane displacement sensor is more likely to detect larger amplitudes resulting from fiber fracture than sensors that are primarily sensitive to out-of-plane displacements. This may be especially true in materials that are anisotropic and highly dispersive or with wave guides along a particular direction. Another observation from the amplitude distributions shown in figure 6.05 is that there were two modes of failure in the Instron tests using the first loading condition. The coupons failed in either a controlled and much slower manner as a crack propagated across the width of the sample, or the coupon suddenly ruptured. A peak at 95 dB was observed each time a coupon failed suddenly.

The three point bending plate experiment produced amplitude values that were actually similar to the literature, but it also created a large number of high amplitude peaks. These are most likely the result of matrix macro-cracking and the saturant debonding from the aluminum plate. The NIST sensor detected amplitudes most often at values of 60, 66 and 69 dB. These results agree very well with the reported theory and experimental results. According to Bohse [50], the theoretically predicted amplitude for a carbon fiber surface break detected by an out of plane transducer is 65 dB and the experimental results obtained in the study ranged from 50 to 75 dB with an average of 69 dB. The NIST results are consistent with these reported amplitude values. Valentin [12] reported a wide range of amplitude values also, however, the expected amplitude value

for a CFRP fiber fracture was 60 dB. Using the published results as a guide, it is possible that the observed amplitude peaks that the NIST sensor observed at 60, 66, 69, 72 and 75 dB are the result of fiber fracture occurring in the FRP/Aluminum plate sample, while in the EFPI the peaks from 65 to 80 dB may be from fiber fracture. Due to the nature of amplitude analysis and the difference in the mechanical testing and signal processing in this work compared to the literature, a direct comparison is not possible. However, it is still interesting, and encouraging, to note the similarities between the literature and the experimental data for a larger test sample under less controlled conditions.

Sustained Load Coupon Experiments

The results from the constant load tests are useful because they provide insight about AE signals that result from CFRP designed for long-term loads, under service conditions. Furthermore, by rapidly applying the load at 26% of the ultimate tensile strength, a realistically damaged condition was created while catastrophic failure of the coupons was avoided in most of the samples.

Significant details can be learned from a qualitative analysis of the amplitude distributions. Trends and similarities in the different signals can be viewed in aggregate and compared with each other and data from the previous section to determine the amplitude value of similar damage mechanisms in each type of coupon. Comparing AE observed using the EFPI on similarly loaded specimens, it is reasonable to assume that peaks occurring at similar values are the result of similar damage mechanisms. Some of these damage mechanisms can be verified by visual observation. For instance, the observed axial splitting in the double ply coupons. In the single ply coupons, it is reasonable to assume that longitudinal cracking also occurred. This kind of cracking along the longitudinal direction would probably produce similar high amplitude peaks in single or double ply coupons. The observed cracking in the specimens followed Prosser's [68] observation that cracks will often, if not always, initiate at an edge and then propagate across the width of the specimen or stop within it.

Figure 6.21 combines the amplitude distributions for the single, double and transverse coupon tests. The distribution from the single ply coupon tests has a different character than either the transverse or the double ply tests. This most likely reason for this

is the local damage at the grips and the cracking that propagated throughout the single ply coupons much more severely than in either of the other sample coupons. However, one amplitude peak that all three have in common occurs at a value of 105 dB. This peak and the other common amplitude values in this range must be the result of splitting along the fiber axis or damage in the polymer layer given that the only forms of damage that could be present in the transverse coupon samples were these two due to the direction of loading. The range of higher amplitudes for these damage mechanisms means that damage from events such as fiber fracture occur at less than 105 dB in single ply coupon samples. Therefore, the observed results from the previous sections are most likely the result of fiber fracture. Figure 6.26 displays the single and double ply sustained load results and the OFB MBrace distributions on the same graph. It is interesting to see that similarities occur in the distributions in amplitude ranges that have not been recognized as potentially due to background noise.

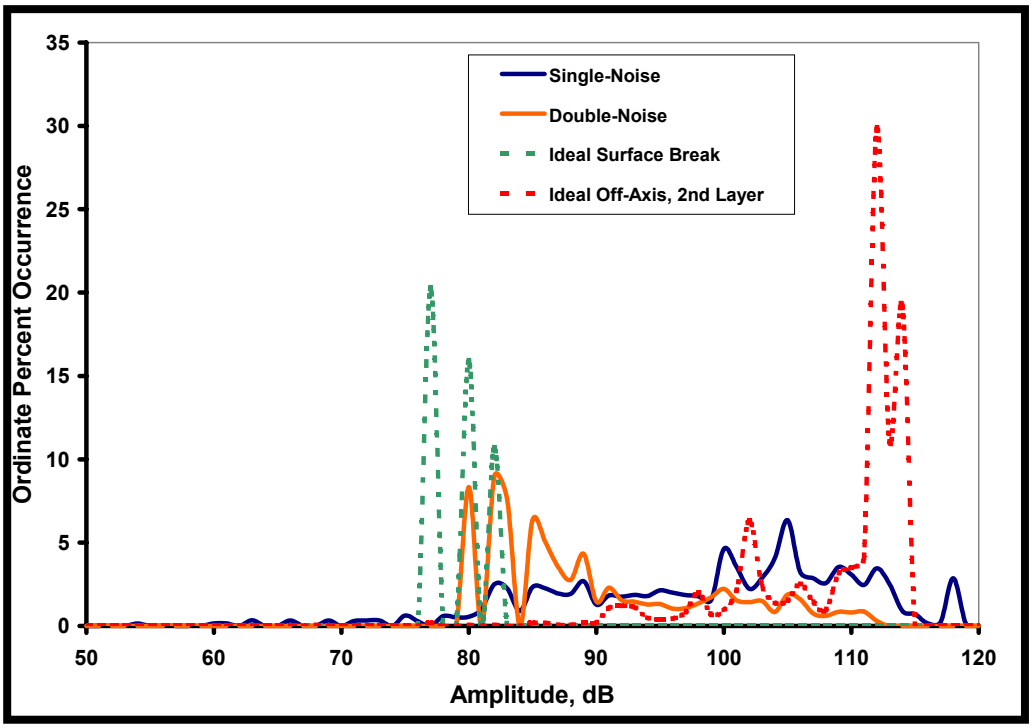

Figure 6.26: Single, Double and Ideal Break Amplitude Comparison.

The single ply distribution does not compare as well to either of the ideal distributions as the double ply distribution does. Examining the common peaks in each distribution, it appears that the single ply coupons cannot be effectively loaded using this experimental set-up without sustaining a large amount of damage so that the amplitude

distribution is the result of many kinds of damage mechanisms. The double ply coupons distributions appear very similar to the surface OFB distribution and could be used in further experiments where the goal is to detect fiber fracture. The peaks located at 80 and 82 dB suggest that the surface OFB may be a good approximation of a top layer fiber fracture along the axis of the EFPI.

Chapter 7 - Conclusions

Summary

A novel fiber optic sensor has been demonstrated to accurately detect in-plane AE in CFRP coupons. The sensitivity of the EFPI to displacements and background noise compares well to other currently available sensors. The EFPI is unique because it is primarily sensitive to displacements along the axis of the optical fibers. It is possible to detect events that are similar to fiber fracture in FRP using the EFPI.

The EFPI was compared against the NIST conical displacement sensor and the PAC R15 sensor. These sensors were chosen because other researchers in fiber fracture experiments that had published their results used them. The signals from the EFPI consistently showed amplitude values at 77, 80 and 82 dB in several experiments where signals from the NIST and PAC R15 sensors observed signals with amplitude values that agreed with previously reported values for fiber fracture. Although, it is not possible to decisively compare the literature results with the test series in this work, the agreement is encouraging and provides a basis for future work. It can be concluded the EFPI responded to displacements caused by fiber fracture and displacements similar to fiber fracture.

The average relative energy from simulated fiber fracture events compared well with the 25^{th} percentile relative energy values from other experiments where fiber fracture occurred. The relative energy detected from signals recorded from the NIST and PAC-R15 did not agree with the simulated events. Overall, the signals detected by the other sensors in these experiments were not as consistent as the EFPI. The average relative energy from the simulated fiber fracture EFPI signals seemed to compare well to the failure of a bundle of carbon reinforcing fibers in a CFRP coupon.

Conclusions

Several conclusions can be drawn from the experimental results. First, with regard to the characteristics of the EFPI as a sensor, it has an equivalent level of sensitivity compared to the PAC R15 and NIST sensors. The EFPI, NIST and PAC R15 also showed a comparable level of background noise for pencil lead breaks and other series of

experiments under similar conditions. Second, the EFPI can indeed detect in-plane displacements and it is more sensitive to these displacements than either the NIST or the PAC R15. The high amplitude content from signals recorded from the EFPI had a low percent error and was fairly consistent. The EFPI can detect fiber fracture and fiber-fracture like displacements. With regards to detecting fiber fracture in CFRP, examining and comparing the results of the experiments from chapter four reveals the common trends and similarities between the AE detected by the EFPI and the other sensors. Figure 7.01 compares the amplitude distributions from the second loading condition used on the Instron test, to the glass wire break on the FRP/steel plate.

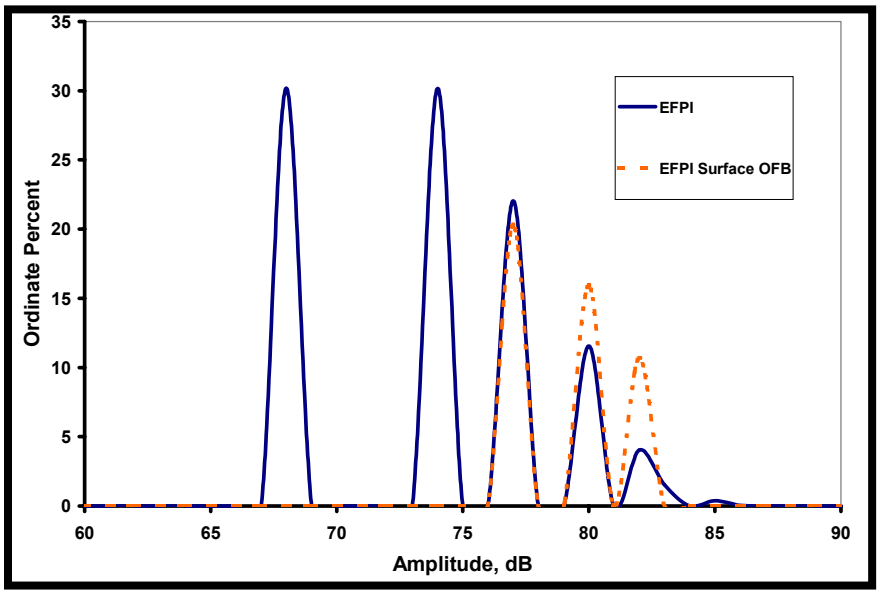

Figure 7.01: Comparison of EFPI AE from Instron Tests and FRP/Steel Glass Wire Break

The amplitude peaks of all distributions in figure 7.01 occur at the same values (77, 80, 82 dB) although at varying frequencies. Which suggests that the glass wire break is a good, repeatable simulation of fiber bundle fracture when it is observed by the EFPI. Figure 7.02 compares the amplitude distributions from the surface break OFB on the unloaded plate detected by the NIST and the EFPI sensors. The close agreement shown in Figure 7.01 is not observed in Figure 7.02. This is the result of the difference between in-plane and out-of-plane displacements, see Figure 4.21. Another factor that could cause disparity between the two is the attenuation of the signal due to the nature of FRP.

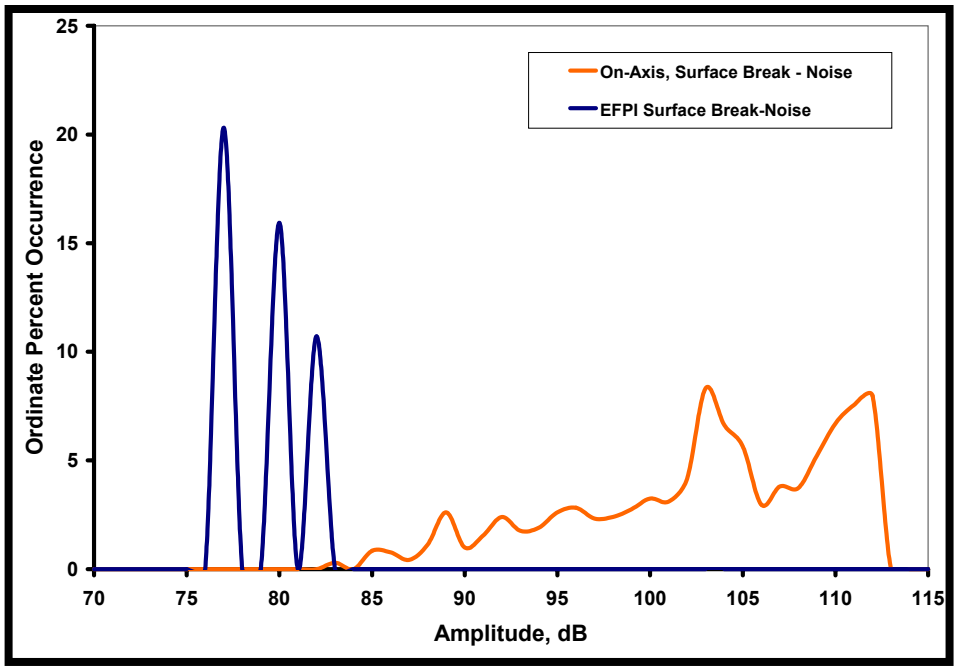

Figure 7.02: NIST/EFPI FRP Steel Plate Surface Break Amplitude Distribution Comparison

Analyzing the EFPI and PAC R15 response to the off-axis and buried glass wire break reveals two similar trends. First, that the EFPI has a less focused distribution (i.e. smaller peaks) in general when the source is off the fiber axis, and second, that the PAC R15 has a more focused distribution, although at higher decibel amplitude values. When the PAC R15 and the NIST sensors detected a significant percent (>5%) of amplitudes at the values determined to be the result of fiber fracture, the EFPI consistently detected amplitude peaks at 77, 80 and 82 dB. Although in all of the experiments, peaks at 80 and 82 dB typically occur more frequently. The amplitude values from signals detected by the EFPI are higher than the reported values for fiber fracture in CFRP using piezoelectric transducers. It is possible that in simulated or real fiber fractures peaks at these amplitude values indicate fiber fracture. When the CFRP coupons were loaded more directly and damage mechanisms other than fiber fracture were possible, the EFPI was still capable of detecting the amplitudes associated with fiber fracture more than 10% percent of the time. It is possible to conclude from these results that not only are the published amplitude values for fiber fracture accurate for larger FRP samples but that the EFPI is capable of consistently detecting displacements due to fiber fracture a greater portion of the time than current out-of-plane sensors.

Table 7.1: Computed MARSE Values from EFPI Signals

Coupon AE Experiment	MARSE
	Average Value
Un-Loaded Plate Glass Wire Surface Break	21.30
Constant Strain Glass Wire Break	21.80
	25th % Value
IL-EFPI Single Ply	20.44
IL-EFPI Double Ply	20.90
CL-EFPI Single Ply	25.23
CL-EFPI Double Ply	25.51
Constant Strain EFPI Double Ply	0.45
EFPI FRP Plate Three Point Bending	159.37

Calculating the MARSE from different experiments can also show the evidence of fiber fracture in the coupons. The relative energy detected by the EFPI was evaluated by taking the 25th percentile value (as in Valentin) from the constant load and Instron experiments and comparing them to the average value from the glass wire breaks, Table 7.1. With the exception of the three point bending experiment and the constant strain experiment, the values are all very close. It can then be concluded that the glass wire break generates a signal that has a rectified signal envelope with an area similar to signals caused by damage mechanisms that occur in FRP. Furthermore, it is possible to conclude that these damage mechanisms are caused by failures of fiber bundles in the composite. The MARSE values from the signals observed by the NIST and PAC R15 sensors do not compare well to each other, the EFPI or the simulated fiber fractures, Table 7.2.

Table 7.2: Computed MARSE values from NIST and PAC R15 signals

Coupon AE Experiment	MARSE
	Average Value
NIST Un-Loaded Plate Glass Wire Surface Break	5.51
PAC-R15 Constant Strain Glass Wire Break	26.89
	25th % Value
IL-PAC R15 Double Ply	20.74
Constant Strain PAC R15 Double Ply	1.76
NIST FRP Plate Three Point Bending	34.81

The most unexpected result of these experiments is that fiber fracture is not necessarily a high amplitude, high frequency event, as seen in Figures 5.07, 5.08, 5.09. Furthermore, the character of the signal and the amplitude of the signal are different if the fiber fracture occurs in a lower ply. These results suggest that the observed amplitudes for ideal FRP samples (i.e. a small number of fibers encased in a block of epoxy), as used

in the literature, are not reasonable for fiber fracture in larger samples in lower layers. Further work needs to be done to fully characterize the behavior of FRP and how a buried source changes both the amplitude and the frequency of the event. However, the results presented here offer a good starting point since all of the work was done without a signal gain in a well-documented and reproducible manner.

Future Work

There a many possible ways of applying the results in this work to the study of CFRP, but all require further testing of the EFPI and calibrating the amplitude response of a sensor with respect to a damage mechanism. A potentially useful application is the long term health monitoring of FRP composites used in the rehabilitation of transportation infrastructure. However, the methods of monitoring and evaluating the observed signals from the EFPI need to be tested on a larger scale. Furthermore, none of the information from a health monitoring system is useful if it cannot be easily explained to engineers so that they can act on it. Using the method of displaying amplitude distributions in this work and assigning a percent value to the acceptable level of damage in FRP would be a simple way to communicate the desired information to engineers who may not be experts in AE or non-destructive evaluation. For example, if an EFPI sensor detected signals that had an amplitude distribution with a 35% peak at 80 dB and the acceptable limit was 25%, then it would be clear that a higher than acceptable number of reinforcing fibers had fractured in that region and that further inspection is necessary. However, pilot studies on repaired piers and concrete columns need to be done before the EFPI can be implemented as a health monitoring tool on a large-scale structure such as a bridge. It will also be necessary to perform further research to quantify the change in sensor response to sources deeper than three layers of FRP reinforcement.

APPENDIX A: Installing the EFPI sensor

Before installing an EFPI sensor, the surface of the substrate should be clean and free of scratches, ridges, or any other items that could catch a fiber. The substrate surface should be prepared by sanding with a fine grade silicon carbide paper or steel wool. After sanding, the surface should be cleaned with acetone and all large dirt particles or lose grit should be cleaned off as well. After the surface is dry and clean, the location of the center of the sensor cavity and the gage length of the fiber should be clearly marked using a soft pencil or a permanent marker.

After opening the case containing the sensor, carefully remove the sensor from its temporary mounting and place it on the substrate. Using masking tape, place a thin strip of tape across the connector end of the fiber optic line attaching it to the substrate. Do not touch the open end of the fiber sensor.

Carefully align the sensor with the location markings. Using a pencil lead, glass wire or the tip of a mechanical pencil, place a small dot of epoxy over the center of the sensor cavity and then a small dot over each end of the gage length. It is preferable to use fast curing epoxy (90 second cure time or faster) to mount the fiber sensor. After the epoxy has cured to a reasonable hardness (a minimum of 30 minutes), heat the sensor to free the interferometric cavity of the phenyl salicylate plugs using a heat gun set to at least 300 ºC for five minutes. If embedding the sensor, encase the sensor in epoxy before melting the phenyl salicylate plugs.

To determine the peak-to-peak output voltage of the sensor, connect it to the equipment used to monitor it and lightly strike the area adjacent to the sensor with a rubber mallet. If the sample is a plate, flexing the plate in the direction parallel to the axis of the EFPI will also produce the desired result. Record the highest and lowest amplitude of the displacement wave caused by the strike. The total amplitude range of the signal is the *Vpp* value.

All other installation, cleaning and maintenance concerns of the sensor, FOSS and fiber optic connectors should be referred to Luna Innovations.

APPENDIX B: Data Filtering and Post-Capture Signal Processing

Introduction to Signal Processing

Data filtering and signal processing are commonly applied to data in order to focus on relevant details or for ease of presentation. Whether the data is a received from laboratory experiments, computer generated models or financial journals, data filtering can easily sift noise or unimportant data from a series of numbers so that the relevant data is all that remains.

Simply put, filtering data is the same as wearing sunglasses or using pre-programmed radio channels. In the case of sunglasses, the environment is too bright and it is preferable to sacrifice a variety of colors for a muted, shaded view of the world using only a few colors. Using pre-programmed radio channels achieves a similar affect for a different reason. It is possible to listen to a lot of frequencies or stations at once, but then it is impossible to discern any music, news or pleasant sound. It is also possible to listen to an extremely narrow bandwidth of frequency, but if that band of frequencies is not near the frequency that any radio station uses to broadcast the radio becomes useless. By choosing pre-arranged standards of frequencies and channels, it is possible to sift through a myriad of choices, static, noise and music to hear exactly what you want to hear.

Data filtering is usually accomplished by taking an algorithm and passing a series of data through it. Various kinds of algorithms exist and while it is not difficult to find a filtering algorithm that will remove unnecessary data from a series of numbers choosing a filter that does it well can be difficult. In signal processing, most algorithms attenuate, or reduce, the strength or amplitude of a pre-determined type of data. Some filters take a relatively long time to attenuate the desired data and others magnify the remaining data so that it is much different from the original data set. Still others affect the position, or phase, of the remaining data in the series. The ideal filtering algorithm does not alter the phase or amplitude of the desired data while attenuating the unnecessary data quickly and efficiently.

The exact definition of what is “important” and what is “quick” must be decided ahead of time and should be based on a popularly agreed standard or previous research. If

the method or level of filtering is not standardized or well known, whoever looks at the filtered data may assume something different from the presented data which negates any benefits of filtering (ease of presentation, highlighting relevant data, eliminating noise, etc.).

Issues when Filtering Acoustic Emission Signals

It is important when dealing with recorded acoustic emission (AE) signals to know exactly how filtering affects a signal. If the amplitude of unwanted data is not attenuated quickly enough, it may alter the perception of the important data. If the remaining data is greatly amplified, then it may be difficult to compare filtered signals to unfiltered ones or other signals that have been processed differently. If the time that different parts of the signal arrive is affected the velocity of the stress wave may be misjudged and different types of waves (Lamb, Rayleigh, Transverse, etc.) may be hidden.The best scenario for filtering AE is to know specifically what frequencies are of interest and what level of signal distortion is allowed.

Using the Signal Processing Toolbox to filter data

When using MATlab or any other digital filtering tool, it is important that all of the data in the series that will be filtered is in the same format, (i.e. same number of decimal places, notation, etc.) or else errors will be generated in the filtered data. It is easiest to import the data into MATLab as either a tab-delimited text file or simple ASCII file. Save or copy the file to the "Work" folder in the MATLab directory. This allows the software to instantly access the data since the "Work" folder is the first location in the directory that the software looks for files. It is also possible to import the data from another location, but this is the easiest way. To import the data into the MATLab workspace, use the "load" command and give the data a variable name. A sample of the syntax follows:

X1 = load ('datastuff.txt');

This command imports the file datastuff.txt into the workspace and assigns a variable name of X1 to it. MATLab will treat the variable X1 as a vector for all further operations.

Alternatively, a Virtual Instrument can be designed using the LABView visual development suite, see figures AB 1 and 2.

LABView Bessel Filter Application

Below are screen captures of the Lab View virtual instrument (VI) used to process the AE signals obtained from the experiments in this work. The VI program was initially designed by Mike Horne and then later modified by Chris Cassino. The modified version is displayed below. The VI reads an ASCII file, and filters the file and outputs two processed files. The first output file is the filtered voltage-time signal. The second output file is the frequency spectra of the filtered file. Figure AC1 shows the front panel display for the VI in operation. Figure AC2 shows the block diagram of the VI from the visual programming design sheet of the Lab View software.

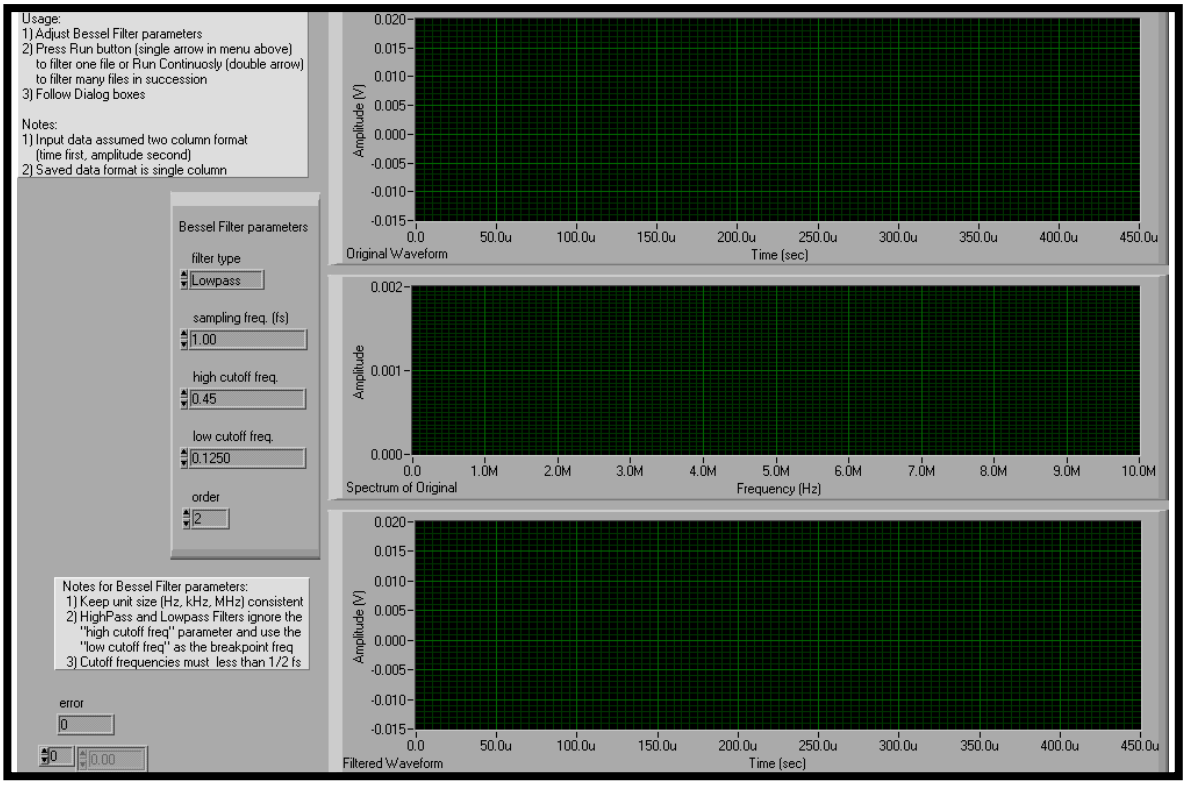

Figure AB1: Bessel Filter VI Front Panel

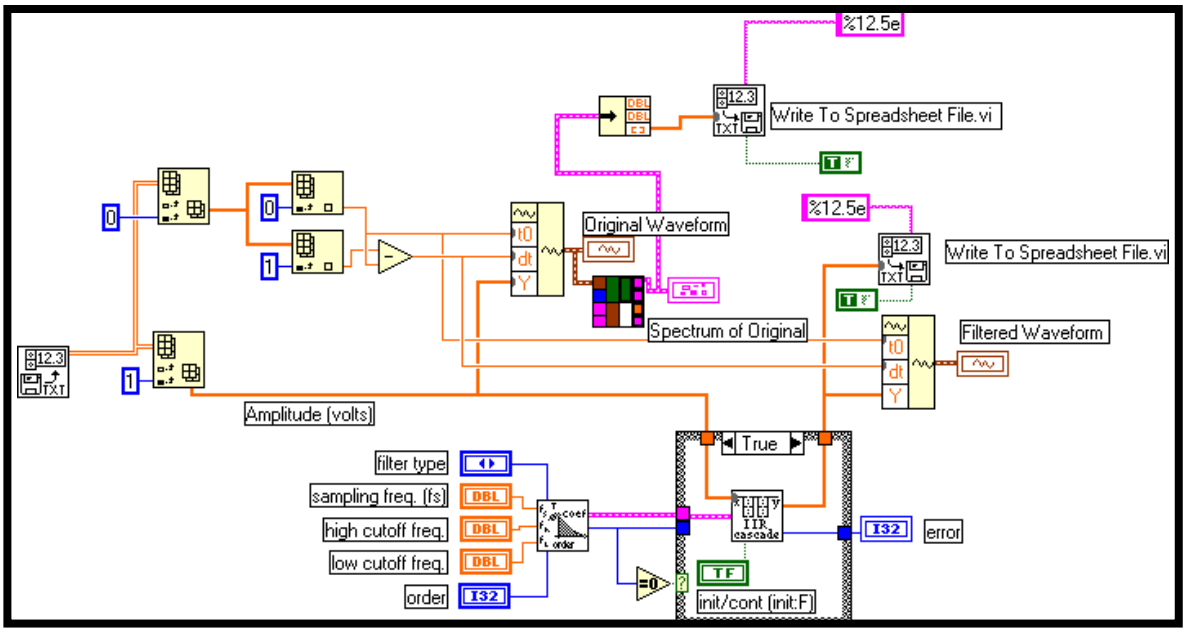

Figure AB2: Bessel Filter VI Block Diagram

Bibliography

1. American Society of Civil Engineering, *ASCE's 2001 Report Card on America's Infrastructure*, . 2001, ASCE.
2. Grigg, N., *Infrastructure Systems*, in *Infrastructure Engineering and Management*. 1988, John Wiley & Sons: New York, New York. p. 25-53.
3. Furh PL, H.D., Nelson M, *Fiber Optic Sensing of a Bridge in Waterbury, Vermont.* Journal of Intelligent Material Systems and Structures, 1999. **10**(April): p. 293-303.
4. Duke, J.C., *Transportation Infrastructure - an Introduction.* Materials Evaluation, 1994. **52**(4): p. 494-495.
5. deVries M, A.V., Meller S, Masri SF, Claus RO, *Implementation of EFPI-based optical-fiber sensor instrumentation for the NDE of concrete structures.* Cement & Concrete Composites, 1997. **19**(February): p. 69-79.
6. Beck, J. and D. Bernal, *Structural testing series: Part 12 - A benchmark problem for structural health monitoring.* Experimental Techniques, 2001. **25**(3): p. 49-52.
7. Kersey AD, D.M., Bellemore D, *Development of Fiber Sensors for Structural Monitoring.* SPIE, 1995. **2456**: p. 262-268.
8. Liu T, W.M., Rao Y, Jackson DA, Fernando GF, *A multiplexed optical fibre-based extrinsic Fabry-Perot sensor system for in-situ strain monitoring in composites.* Smart Materials & Structures, 1998. **7**(August): p. 550-556.
9. Tang, B.P., *Fiber Reinforced Polymer Composites Applications in USA*, . 1997, DOT-Federal Highway Administration.
10. Mayo, R., *Strengthening of Bridge G270 with Externally-Bonded CFRP Reinforcement.* American Concrete Institute Proceedings, 1999. **SP-188**: p. 429-440.
11. Mirmiran, A., *Acoustic Emission Monitoring of Hybrid FRP-Concrete Columns.* Journal of Engineering Mechanics, 1999. **125**(8): p. 899-905.
12. Valentin D, B.A., *A Critical Analysis of Amplitude Histograms obtained during Acoustic Emission Tests on Unidirectional Composites with an Epoxy and PSP matrix.* Composites, 1985. **6**(3): p. 225-230.

13. Weil, G.J., *Introduction to Nondestructive Measurements*, in *CRC Handbook of NDT on Concrete*. 2000, CRC Press. p. 305.
14. Physical Acoustics Corporation, *Introduction to Lamb Wave in Plates*, . 2001, PAC: Princeton Junction, New Jersey. p. 1-9.
15. Pollock, A.A., *Classical Wave Theory in Practical Acoustic Emission Testing*, . 1986, The Japanese Society of NDI: Tokyo, Japan.
16. Pollock, A.A., *Acoustic Emission Inspection*, in *Handbook of Nondestructive Engineering*. 1997, John Wiley & Sons: New York, New York. p. 278-294.
17. Proctor, T., Breckenridge, FR, Pao, YH, *Transient Waves in an elastic plate: Theory and experiment compared.* Journal of the Acoustical Society of America, 1983. **74**(6): p. 1905-1906.
18. Prosser, W.H. and Langley Research Center, *The propagation characteristics of the plate modes of acoustic emission waves in thin aluminum plates and thin graphite epoxy composite plates and tubes*, . 1991, National Aeronautics and Space Administration Langley Research Center
19. Prosser, W.H., Hamstad, M.A., Gary J., O'Gallagher, A., *Reflections of AE Waves in Finite Plates: Finite Element Modeling and Experimental Measurements.* Journal of Acoustic Emission, 1999. **vol. 17(1-2)**: p. 37-47.
20. Rabinovitch, O. and Y. Frostig, *On edge stresses control in strengthened RC beams with FRP strips: Adhesive layer profile effect.* Journal of Engineering Mechanics-ASCE, 2001. **127**(4): p. 317-325.
21. Sison, M., *et al.*, *Acoustic emission: A tool for the bridge engineer.* Materials Evaluation, 1996. **54**(8): p. 888-&.
22. Sison, M., *et al.*, *Analysis of acoustic emissions from a steel bridge hanger.* Research in Nondestructive Evaluation, 1998. **10**(3): p. 123-145.
23. Viktorov, I.A., *Rayleigh and Lamb Waves-Physical Theory and Applications*. Ultrasonic Technology - A series of Monographs, ed. L. Balamuth. 1967, New York, New York: Plenum Press.
24. Tewary, V.K., *Elastic Green's Functions for anisotropic solids (review).* NIST Special Publication, 1996. **SP 910**.

25. Tewary, V.K., *Elastostatic and Elastodynamic Green's Functions*, . 1996, National Institute of Standards and Technology.
26. Valentin D, B.A., *A study of damage accumulation in carbon fibre epoxy resin structures during mechanical loading monitoring by acoustic emission.* Journal of Reinforced Plastics and Composites, 1982. **1**(4): p. 314-334.
27. Sun, W. and F. Lin, *Computer modeling and FEA simulation for composite single fiber pull-out.* Journal of Thermoplastic Composite Materials, 2001. **14**(4): p. 327-343.
28. Williams JH Jr., L.S., *Acoustic Emission Monitoring of Fiber Composite Materials and Structures.* Journal of Composite Materials, 1978. **12**(October): p. 348-370.
29. Shehata, E., R. Morphy, and S. Rizkalla, *Fibre reinforced polymer shear reinforcement for concrete members: behaviour and design guidelines.* Canadian Journal of Civil Engineering, 2000. **27**(5): p. 859-872.
30. Nikos, D., *Appendix: Wave Propagation in Anisotropic Media*, . 1997, Stanford Exploration Project, University of Leeds.
31. Al-Dulaijan, S.U., *Effect of environmental pre-conditioning on bond of FRP reinforcement to concrete.* Journal of Reinforced Plastics and Composites, 2001. **20**(10): p. 881-900.
32. Borinksi, J.W., Richard L. Clark, A. Paige Furrow, John C. Duke, Michael R. Horne, *Fiber Optic Acoustic Emission Sensors and Detection*, . 2000, Luna Innovations and Virginia Polytechnic Institute and State University: Blacksburg, Virginia. p. 5.
33. Kiernan, M.T., *A Physical Model for the Ultrasonic Method*, Dissertation in *Engineering Science and Mechanics*. 1989, Virginia Polytechnic Institute and State University: Blacksburg, Virginia.
34. E 1316 - 97b, A., *Standard Terminology for Nondestructive Examinations*, . 1997, ASTM: New York, New York. p. 619-648.
35. E 1106-86, A., *Standard Method for Primary Calibration of Acoustic Emissions Sensors*, . 1997, ASTM: New York, New York. p. 501-509.

36. E 1781-96, A., *Standard Practice for Secondary Calibration of Acoustic Emissions Sensors*, . 1996, ASTM: New York, New York. p. 884-889.
37. E 650-97, A., *Standard Guide for Mounting Piezoelectric Acoustic Emissions Sensors*, . 1997, ASTM: New York, New York. p. 265-266.
38. E 750-88, A., *Standard Practice for Characterizing Acoustic Emissions Instrumentation*, . 1993, ASTM: New York, New York. p. 346-354.
39. E 976-94, A., *Standard Guide for Determining the Reproducibility of Acoustic Emission Sensor Response*, . 1994, ASTM: New York, New York. p. 386-391.
40. Murphy, K. and J.C. Duke, *A Rugged Optical Fiber Interferometer For Strain-Measurements Inside a Composite-Material Laminate.* Journal of Composites Technology & Research, 1988. **10**(1): p. 11-15.
41. Henneke, E., *Personal Notes on Wave Propagation in Elastic Solids*, . 2001, None.
42. Kriz, R.D., *Introduction to the Mechanical Behavior of Anisotropic Materials*, . 2002, Virginia Tech.
43. Chew, W.C., *Waves and fields in inhomogeneous media*. IEEE Press series on electromagnetic waves. 1995, New York: IEEE Press. xx, 608.
44. Achenbach, J., *Wave Propagation in Elastic Solids*. 1987: North-Holland.
45. Pavic, G., *Structure-bourne Energy Flow*, in *Handbook of Acoustics*, Crocker, Editor. 1998, John Wiley & Sons, Inc. p. 713-723.
46. Plonus, M.A., *Applied Electromagnetics*. 1st Edition ed. 1978: McGraw-Hill Book Company.
47. Shiloh, K., *Aging characterization of adhesives and bonded joints by non-destructive damping measurements.* Journal of Intelligent Material Systems and Structures, 1999. **10**(5): p. 353-362.
48. Meirovitch, L., *Fundamentals of Vibrations*. 2nd ed, ed. K. Druffner. 2001, New York, New York: McGraw-Hill.
49. Chen HL, W.K., *Study of Acoustic Waveguides on Concrete Slabs.* Journal of Non-Destructive Engineering, 2001. **19**(4): p. 125-126.

50. Bohse, J., *Acoustic Emission characteristics of Micro-failure Processes in Polymer Blends and Composites.* Composites Science and Technology, 2000. **60**: p. 1213-1226.
51. Aberg, M., *Numerical Modeling of Acoustic Emission in Laminated Test Specimens.* International Journal of Solids and Structures, 2001. **38**: p. 6643-6663.
52. Gudmundson, P.a.A., M, *Micromechanical modeling of transient waves from matrix cracking and fiber fracture in laminated beams.* International Journal of Solids and Structures, 1999: p. in Press.
53. Duke, J.C., Cassino, C.D., Childers, B. , Prosser, W.H., *Characterization of an Extrinsic Fabry Perot Optical Fiber Interferometric AE Sensor*, . 2001, Virginia Polytechnic Institute and State University- NDE Development Laboratory, Luna Innovations, NASA/Langley Research Center: Blacksburg, Virginia. p. 13.
54. Luna Innovations, *FOSS I Operation and Fringe Counting*, . 1997, Luna Innovations: Blacksburg, Virginia. p. 1-10.
55. Luna Innovations, *EFPI Embedment Strain Gage Installation: Special Topics, Revision B.* Proprietary Technical Support Document, 1999. **EFPI Fiber Optic Strain Gage Notes**(8/1999).
56. Luna Innovations, *EFPI Embedment Strain Gage for Laminates, Special Topics, Revision B.* EFPI Technical Notes, 1999(8/1999).
57. Liu T, B.D., Martin A, Braddock R, Ralph B, Fernando GF, *A multi-mode extrinsic Fabry-Perot interferometric strain sensor.* Smart Materials & Structures, 1997. **6**(August): p. 464-469.
58. Auld, B., *Acoustic Fields and Waves in Solids, Vol I & II*. 1973: John Wiley and Sons.
59. MBrace, S.E.f.M.C., *Fiber Volume Fraction in MBrace CFRP System*, . 2001.
60. Dietzhausen, H., *Numerical Simulation of acoustic emission in fiber reinforced polymers.* Computational Materials Science, 1998. **13**: p. 23-30.
61. Mitzutani, Y., *Fracture Mechanism Characterization of Cross-Ply Carbon Fiber Composites using Acoustic Emission Analysis.* NDT&E International, 2000. **33**: p. 101-110.

62. Scott, M., *Automated characterization of bridge deck distress using pattern recognition analysis of ground penetrating radar data.* Materials Evaluation, 2000. **58**(11): p. 1305-1309.
63. Worlton, D., *Experimental Confirmation of Lamb Waves at Megacycle Frequencies.* Journal of Applied Physics, 1961. **32**(6): p. 967-971.
64. Auld, B.A., *Micro and Macrostructural dispersion of guided waves in solids.* Wave Motion, 1995. **21**: p. 101-114.
65. Breckenridge, P., Hsu, Fick, Eitzen. *Progress in Acoustic Emission V*. in *Progress in Acoustic Emission V*. 1990. Tokyo: JSNDI.
66. Hamstad, M., Gary, J, Journal of Acoustic Emission, 1994. **12**(3-4): p. 157-170.
67. Mbrace, *MBrace Fiber Reinforcement Systems (Product Specifications and Brochure)*, , M.B. Technologies, Editor. 1998, MBT Holding A.G. p. 2.
68. Prosser, W., *Advanced Waveform-based acoustic emission detection of matrix cracking in composites.* Materials Evaluation, 1995: p. 1052-1058.

Vita

Christopher Daniel Cassino was born in Charlottesville, Virginia in 1977. He spent time in many different parts of America while growing up but he considers his childhood home to be Arizona where he first learned the joy of taking apart expensive things and putting them back together with spare parts left over. Despite the warnings of high school guidance counselors (they wanted Chris to become a history teacher), he went to Rowan University in Glassboro, New Jersey. He earned a Bachelor of Science in Infrastructure Engineering while on the PRIDE 2000 engineering scholarship. After graduating from Rowan, Chris decided to pursue an advanced degree in the Engineering Science and Mechanics department at Virginia Tech. Chris now lives in Blacksburg, Virginia with his beautiful wife Theresa, who also attends Virginia Tech.

Chris has presented his research on composites and polymeric materials at the 1998 American Institute of Chemical Engineers mid-Atlantic conference, the 9th Annual UNI-TECH conference at the New Jersey Institute of Technology, the 17th Annual American Society for Composites Conference and the 2001 American Society of Mechanical Engineers World Congress. He has won awards for best presentation, best poster presentation, and best paper on the testing of materials. Chris is currently working on ways to use novel materials in the design and rehabilitation of structures.